Fundamental Behavior of Nanoporous Networks in the Out-of-Autoclave Manufacturing of Carbon Fiber Reinforced Polymer Composites

by

Alisa Nicole Webb

B.S., Mechanical Engineering, William Marsh Rice University (2022)

Submitted to the Department of Aeronautics and Astronautics
in partial fulfillment of the requirements for the degree of

MASTER OF SCIENCE IN AERONAUTICS AND ASTRONAUTICS

at the

MASSACHUSETTS INSTITUTE OF TECHNOLOGY

September 2024

© 2024 Massachusetts Institute of Technology. All rights reserved.

The author hereby grants to MIT a nonexclusive, worldwide, irrevocable, royalty-free license to exercise any and all rights under copyright, including to reproduce, preserve, distribute and publicly display copies of the thesis, or release the thesis under an open-access license.

Authored by: Alisa Nicole Webb
Department of Aeronautics and Astronautics
August 09, 2024

Certified by: Brian L. Wardle
Professor of Aeronautics and Astronautics & Mechanical Engineering
Thesis Supervisor

Accepted by: Jonathan How
Professor of Aeronautics and Astronautics,
Chair, Graduate Program Committee

Fundamental Behavior of Nanoporous Networks in the Out-of-Autoclave Manufacturing of Carbon Fiber Reinforced Polymer Composites

by

Alisa Nicole Webb

Submitted to the Department of Aeronautics and Astronautics
on August 09, 2024 in partial fulfillment of the requirements for the degree of

MASTER OF SCIENCE IN AERONAUTICS AND ASTRONAUTICS

ABSTRACT

Throughout the aerospace industry, carbon fiber reinforced polymer (CFRP) laminated composites are used extensively in spacecraft and aircraft vehicles due to their high specific strength and stiffness and other properties. Processing these advanced structural CFRP composites, especially in prepreg form, is often completed via autoclaves where elevated temperatures and pressures of typically 180 °C (350 °F) and 0.7 MPa (7 bars), respectively, are applied to cure the polymer matrix and compress the constituent laminae together. However, autoclaves are energy intensive, expensive, and impose geometrical constraints on components due to thermal gradients within the chamber. Thus, there exists a need to find alternative manufacturing techniques. Throughout this thesis, an alternative method to autoclave processing is presented using vacuum-bag only (VBO) techniques with nanoporous networks (NPNs) in the interlaminar regions in autoclave-required epoxy prepreg CFRP composites. Nanoporous materials are defined as materials containing pores in the mid nanometer to low micrometer range. Once placed in the interlaminar region of the laminate, voids are reduced by the induced capillary pressures of the NPNs, and trapped gas evacuates through the NPN. By utilizing capillary flow porometry, capillary pressure and through-thickness permeability are quantified for various NPNs, along with other porous materials. Capillary pressure and permeability exhibit an inversely proportional relationship for all tested materials with CNT-based and polymer aerogel NPNs providing capillary pressures higher than an autoclave pressure of 0.7 MPa. Accordingly, an Ashby-type plot is presented as an aid for NPN selection for composites manufacturing. Previous studies of unidirectional glass fiber reinforced polymer (GFRP) composites and unidirectional CFRP composites show success with NPN-enabled VBO-manufacturing using aligned carbon nanotubes (A-CNTs) and electrospun polymer nanofiber (EPN) mats. However, success with

woven prepreg has not been consistently achieved before this thesis. Autoclave woven epoxy CFRP laminates of IM7/8552 are manufactured using EPN and polymer aerogel NPNs with a VBO procedure. Once manufactured, these laminates were characterized for quality through void content analysis. 0.11 void vol% was achieved which is well within the 1 vol% of void requirement for aerospace-grade composite components. To aid the in the understanding of NPNs, in situ experiments utilizing microcomputed tomography are developed to investigate the (presumed Newtonian) flow of resin throughout the NPN as a function of temperature, which varies throughout a typical manufacturer recommended cure cycle (MRCC), along with the void evolution throughout the cure cycle. Based on this new in situ understanding, a manufacturing process modification is devised to produce void-free woven laminates at the 152.4 mm laminate scale. Through manufacturing, material characterization, and designed in situ experiments, this thesis demonstrates the use of NPNs for VBO-manufacturing of low-void content aerospace-grade CFRP composites to replace autoclaves for energy and cost savings.

Thesis supervisor: Brian L. Wardle
Title: Professor of Aeronautics and Astronautics & Mechanical Engineering

Acknowledgments

To my mentors, friends, and family, thank you for your strong support throughout my experience here at MIT. First and foremost, I want to give a special thanks to Professor Brian L. Wardle. He has provided mentorship, both professionally and academically, which has led to invaluable guidance that I will continue to employ throughout my academic and professional journey. I'd also like to thank Jingyao, Carina, Luiz, and Palak who have been mentor figures to me throughout my past two years in necstlab. They were always available to support and encourage my success. Furthermore, the author and thesis supervisor would like to thank Dr. Seth Kessler and Dr. Estelle Kalfon-Cohen from Metis Design Corporation for their expertise throughout this project.

I would like to thank my lab, necstlab, for all their support and guidance for the past two years. To Shaan, Steven, Yuying, and Chris, I'm grateful we started this experience together and appreciate the friendship that blossomed from shared classes and laughs. To Heidi, Briana, Seryna, Gene, Seema, Redshirts, and many others, thank you for making me feel at home, whether in Cambridge or Louisiana. Finally, I would like to thank my family who have supported my every decision and always provide a listening ear for my troubles. To my father, Brian Webb, and my mother, Stacey Webb, thank you for always encouraging me to push the limits and do more than what is expected. To my younger sister, Bre Webb, thank you for all your encouragement, the spontaneous Roblox breaks, and the constant laughs.

Funding Acknowledgements

This work in this paper is supported by the U.S Office of Naval Research (ONR) under grant/contract number N00014-20-1-2300 and by the Naval Air Warfare Center under Contract no. N68335-20-C-0213 awarded to Metis Design Corporation (Boston MA), and partially supported by Airbus, ANSYS, Boeing, Embraer, Lockheed Martin, Saab AB, and Teijin Carbon America through MIT's Nano-Engineered Composite aerospace STructures (NECST) Consortium. This material is based upon work supported by the National Science Foundation under Grant No. DGE-2141064. This material is based upon work supported in part by the U. S. Army Research Office through the Institute for Soldier Nanotechnologies at MIT, under Cooperative Agreement Number W911NF-18-2-0048. Micro-computed tomography instrumentation supported by the Office of Naval Research (ONR) under grant number ONR.N000141712068 through the Defense University Research Instrumentation Program (DURIP) is gratefully acknowledged. The author gratefully acknowledge the members of necstlab at MIT for technical support and advice, Professor Gregory Rutledge (MIT) and their group for use of their porometry equipment, and POROMETER for the capillary flow porometry results for the Celgard materials.

To conclude the acknowledgments, provided is a quote that I discovered as a teen and has resonated with me ever since:

"I think science and technology are the most powerful things in society. They are something that is molded with humanity. Humanity molds technology and science. They are interdependent and intertwined." -Mae C. Jemison

Contents

Abstract **3**

Acknowledgments **5**

List of Figures **11**

List of Tables **21**

List of Abbreviations and Symbols **23**

1 Introduction **27**

1.1 Motivation 27

1.2 Thesis Outline 30

2 Background **33**

2.1 Traditional Production of Fiber Reinforced Polymer Composites 33

2.2 Manufacturing Processes with Carbon Fiber Reinforced Polymer Composites 35

2.2.1 Autoclave Manufacturing 35

2.2.2 Out-of-Autoclave (OoA) Manufacturing 38

2.2.3 Nanoporous Network (NPN) enabled OoA Manufacturing 40

2.3 Nanoporous Networks (NPNs) 42

2.4 Capillary Flow Porometry (CFP) 43

2.5 X-Ray Computed Tomography 45

2.6 Summary and Conclusions 48

3 Objectives and Approach **49**

3.1 Objectives 49

3.2 Approach 50

3.3 Limitations of Current Work 51

4 Fundamentals of Nanoporous Networks **53**

4.1 Selection of NPN Materials 54

4.1.1 Creation of Carbon Nanotube Thin Films 54

4.1.2 Bespoke Commercial Aerogel Film Types 56

4.1.3 Other Commercially Available Materials 57

4.2 Behavior of NPN within Interlaminar Regions 59

4.2.1 Capillary Pressure for Interlaminar Void Removal 59

4.2.2 Permeability for Void Evacuation 63

4.2.3 Secondary Characteristics of NPN for Resin Cannibalization and Interlaminar Region Thickness 67

4.3 Experimental Values of NPNs 68

4.4 Ashby Guideline for Nanoporous Materials 68

4.5 Summary 69

5 In Situ Visualization of CFRP Laminate Curing with and without Nanoporous Networks **73**

5.1 Development of In Situ Resin Flow Monitoring and 3D Void Observation Devices 74

5.2 Initial μCT In Situ 2D Newtonian Resin Flow Monitoring Results of AS4/8552 Composites 79

5.3 3D Multi-Step μCT In Situ Void Observation Results of Woven IM7/8552 Composites 82

5.4 Summary 87

6 Manufacturing and Void Analysis of IM7/8552 Woven Autoclave Prepreg with Nanoporous Networks **93**

6.1 Manufacturing Process for Transferring NPN into the Interlaminar Region of Autoclave Aerospace-grade CFRP Composites 94

6.2 IM7/8552 Autoclave Woven Composites 94

6.2.1 Cure Profile and Layup Process of IM7/8552 VBO-Manufactured Composites 95

6.2.2 Quality of Manufactured Laminates 100

6.3 Summary 110

7 Conclusions and Recommendations **111**

7.1 Summary of Thesis Contributions 112

7.2 Recommendations for Future Work 114

References **117**

List of Figures

1.1 Specific modulus against specific strength Ashby plot for metal alloys, composites, and CNTs. From Wardle et al. 28

1.2 S-curve plot demonstrating advanced carbon materials within aircraft structures as a function of composite wt%. The upper curve represents advanced carbon fiber composites, while the lower curve represents CNT-based materials. From Gorbatikh et al. 29

2.1 Common vacuum bag system procedure for autoclaves for curing of composites. Edge bleeder is only utilized for select aerospace CFRP composite systems. Adapted from Drakonakis et al. [38]. 36

2.2 Manufacturer Recommended Cure Cycle (MRCC) for 8552 based composites. The bold line represents the temperature profile of the cure cycle, the dash-dotted line at the bottom of the graph represents the vacuum applied to the component, and the two upper dashed lines demonstrate the supplied autoclave pressure dependent on part type. From [46]. 37

2.3 Two types of prepreg are presented: (Top) IM7/8552 autoclave prepreg and (Bottom) IM7/M56 out-of-autoclave prepreg. Optical micrographs captured by Dr. Jeonyoon Lee (former student of necstlab, a research group at MIT). 39

2.4 Nanoporous network (NPN) manufacturing with carbon nanotubes in the interlaminar region of a composite. Figure from Lee et al. [25]. 41

2.5 Illustration of the removal of wetting fluid within the pores of a porous membrane via applied inert gas. The numbers at the bottom of the figure represent the order in which the wetting liquid is removed from the pores; 1 represents the first pore emptied of the wetting liquid. Adapted from [78]. 45

2.6 Diagram of three curves— dry curve (green), half-dry curve (maroon), and wet curve (red)— obtained during CFP, along with classification of pore categorization and saturation status (s). The half-dry curve is obtained analytically, while the dry and wet curve are measured directly from the experiment. The saturation of the membrane during the wet curve portion of CFP is shown by the green line labelled wet curve in the same hue as the saturation axis. The pressure is in units of barg (pressure in bars above atmospheric pressure) for this figure. From Bromberger et al. [80]. 46

2.7 Schematic of cone beam systems common in laboratory-based microcomputed tomography (μCT) tools. Provided by Withers et al. [87]. 47

4.1 Illustration of CNT knockdown process using PTFE circular cutouts. The black rectangles represent CNTs, the flexible, blue circle represents the Omnipore® PTFE membrane, the gray rectangle represents the rounded blade, the green rectangle represents the silicon substrate where the VA-CNT array is grown on, and the red arrow demonstrates the direction of the blade's force. This figure was created by Grant Oh, an undergraduate researcher of necstlab, a research lab at MIT. 56

4.2 SEM depicting the HA-CNT thickness measurements. The red bracket indicates the CNT forest, while the light blue bracket indicates the PTFE film support. 57

4.3 Capillary pressure versus through-thickness permeability for a variety of PI aerogels. Red circles indicate AD PI aerogel films, while blue triangles represent SCD PI aerogel films. Regardless of drying type, capillary pressure, thus pore size, is typically consistent between the film types. 58
4.4 Top-View SEM image of a AD PI aerogel film manufactured by Aerogel Technologies, LLC. The nominal thickness of this film has been measured at 61 μm with μCT. 58
4.5 Top-view SEM images of other commercial porous materials: (a) Trilayer Polymer Membrane - Celgard 2325; (b) Anodic Aluminum Oxide; (c) Hydrophilic Polyvinylidene Fluoride Membrane; (d) 21 μm polymer NPN. . . . 60
4.6 Vapor curves of acetone, ethanol, and water - the main volatiles found within HexPly 8552 prepreg. Figure provided by Agius et al. [107]. 61
4.7 A schematic demonstrating the pressure balance within a laminate without NPNs and with inserted NPNs to demonstrate the removal of voids within the interlaminar region. This illustration is depicted with the use of aligned CNTs, but this is applicable for all NPNs. Figure provided by Lee et al. [25]. 62
4.8 Provided form factors for longitudinal and transverse flow of fiber beds used to model flow for VA-CNTs and HA-CNTs. The equations for the equivalent diameter of pores within the fiber network (D_e) is expressed. Provided by Ahn et al. [110]. 64
4.9 Flow versus pressure plots for 8 measured NPNs - 2 Celgard membranes, 2 PI aerogel films, buckypaper, 12 μm polymer NPN, hydrophilic PVDF membrane, and an AAO membrane. Steep slopes of the non-zero flow portion of the wet curve indicate small disparities of the pore size in the membrane. The wet curve aligning with the dry curve signifies full drying of the tested membrane. Different color lines in each plot signify different (repeat) samples. 65

4.10 Capillary pressure versus through-thickness permeability for nanoporous materials using wetting liquid, Porefil™, as the fluid source. All data points were tested at least three times with the plotted point being the average of the results within this Ashby plot. The general trend of an inverse relationship between capillary pressure and permeability is shown clearly here. 70

4.11 Capillary pressure versus through-thickness permeability for the three NPN material families used in FRP composites using HexPly ® 8552 resin as the fluid source. All data points were tested at least three times with the plotted point being the average of the results within this Ashby plot. The bold green line represents the 7 bar pressure typically supplied by an autoclave for epoxy-based CFRP aerospace-grade composite laminates. 71

5.1 Viscosity and degree of cure calculated for a 1°C/min of HexPly 8552 resin. Figure provided by Van Ee et al. [118]. 75

5.2 Physical set-up of the 2D Newtonian resin flow monitoring thermal-mechanical system. The system is directly attached to the rotating scanning stage of the μCT (Zeiss Xradia 620 X-ray microscope) chamber through a connector printed via stereolithography. Note this set-up was abandoned after initial testing. 76

5.3 Physical set-up of the updated 2D Newtonian resin flow monitoring thermal-mechanical system. The previously-used CPU cooler and compression system (see Figure 5.2) has been discarded. The system is directly attached to the rotating scanning stage of the μCT (Zeiss Xradia 620 X-ray microscope) chamber via a Zeiss supplied sample holder. The extended wires shown in the right figure are connected to the Peltier module with two attached thermocouples for redundancy. 77

5.4 3D Observational Void Experiment: Left: Physical set-up of the 3D laminate void evolution monitoring thermal-mechanical system. The system is directly attached to the rotating scanning stage of the μCT (Zeiss Xradia 620 X-ray microscope) chamber through a connector printed via stereolithography. Inset shows the laminate mounting assembly without the vacuum-bag-only configuration. Right: A screenshot of a captured projection displaying the laminate components showing their position during the scan set-up. 79

5.5 Projection of 2D Newtonian Resin Flow Front Experiment with the Associated Configuration Schematic: Left: Captured projection demonstrating the configuration of the NPNs and surrounding laminae. The circle on the far right corner and the horizontal line shown towards the top of the laminate are the thermocouple head and its attached wire. Right: Schematic of the laminate with integrated NPN, the supporting thermocouples (labelled A, B, and C), and two attached thermal module assemblies. The gray rectangles in the schematic represent laminae and the yellow squares represent aerogel thin films. 80

5.6 Temperature plot showing the laminate thermocouple (labelled B in Figure 5.5) temperature during the initial captured projections. The reduced temperature ramp rate before the 10 minute mark is a result of altered DC power supply input to reduce the heating ramp rate. The temperature ramp rate was adjusted to decelerate the flow front speed due to the pre-determined projection sampling rate of 4 seconds. 81

5.7 Initial results of the 2D Newtonian flow monitoring experiment with a 8-ply ($[0]_8$) AS4/8552 unidirectional-ply CFRP laminate. The temperature is that of the thermocouple placed in the middle of the laminate. The short and red horizontal line near the temperature label is the interface between the NPN and CFRP lamina where the thermocouple is placed. 83

5.8 Temperature plot showing the applied temperature to the laminate versus time for the 3D multi-step μCT experiment (for Step 0 and Step 1 only). The laminate for this plot is the $[0]_5$ IM7/8552 woven laminate with PI aerogel NPN (no laminae desolventing). The long scan times are illustrated within this figure. 84

5.9 CFRP woven laminate cross-section and surrounding components during the 3D μCT in situ multi-step experiment. The main components are the laminate, GNPT-wrapped caul plate, attached peel ply, and aluminum T-bar. This reconstructed image is provided from Step 0 of the second multi-step μCT experiment for the laminate with applied aerogel NPN (without desolventing). There exists voids within the intralaminar regions in this image. 85

5.10 $[0]_5$ woven IM7/8552 laminate with no applied NPN and no desolventing for the first multi-step μCT experiment. 89

5.11 $[0]_5$ woven IM7/8552 laminate with aerogel NPN (named Aerogel PI 50 μm) and no desolventing processing for the second multi-step μCT experiment. . 90

5.12 $[0]_5$ woven IM7/8552 laminate with aerogel SCD NPN (named Aerogel PI 50 μm) and desolventing processing for the third multi-step μCT experiment. . 91

6.1 A reconstructed μCT scan of a baseline, autoclave-manufactured IM7/8552 woven $[0]_{12}$ laminate with no applied NPN. No voids are present throughout the laminate at the utilized pixel size. For this scan, the pixel size was 1.77 μm with an exposure time of 2.5s. The voltage of the scan was 100 kV with an applied filter of LE2 to increase overall transmittance. 96

6.2 VBO assembly used for all CFRP laminates manufactured within this thesis. This system is placed within an oven to complete the cure cycle's temperature requirements. 98

6.3 A reconstructed μCT scan of an IM7/8552 woven $[0]_8$ laminate with AD PI Aerogel NPN. The dark gray regions represent an absence of material indicating large void content, in both the intralaminar and interlaminar regions, of this manufactured CFRP composite. For this scan, the pixel size was 1.17 μm with an exposure time of 3s. The voltage of the scan was 120 kV with an applied filter of LE1 to increase overall transmittance. No special processing was performed on this laminate. 99

6.4 Representative cross-sectional view of the IM7/8552 woven laminate without applied NPN manufactured via VBO and oven at the 25.4 mm (1-inch) scale. Large voids are present throughout the laminate with the calculated void content being 3.176 vol%. This scan was produced 1.91 μm pixel size, 3 second exposure, voltage of 80 kV, and with a LE2 filter. 102

6.5 Representative cross-sectional view of the two IM7/8552 woven laminates with SCD PI aerogel NPN produced with VBO and oven at the 25.4 mm (1-inch) scale. The top laminate corresponds to Laminate IM7/8552 SCD Aerogel II 1" and the bottom laminate corresponds Laminate IM7/8552 SCD Aerogel I 1". The void content of the top laminate is 0.170 vol%, while the bottom laminate has a void content of 0.162 vol%. This scan was produced using 1.55 μm pixel size, 3 second exposure, voltage of 100 kV, and with a LE2 filter. . 102

6.6 Representative cross-sectional view of the IM7/8552 woven laminates with AD PI aerogel NPN manufactured via VBO and oven at the 25.4 mm (1-inch) scale. The void content of this laminate is 0.035 vol%. This scan was produced using 1.59 μm pixel size, 3 second exposure, voltage of 80 kV, and with a LE1 filter. 103

6.7 Representative cross-sectional view of the IM7/8552 woven laminate with EPN 12 μm NPN produced with VBO and oven at the 25.4 mm (1-inch) scale. The void content of this laminate is 0.003 vol%. This laminate has the lowest void content of the manufactured 25.4 mm (1-inch) laminates. This scan was produced using 1.24 μm pixel size, 4 second exposure, voltage of 80 kV, and with a LE2 filter. 103

6.8 Representative cross-sectional view of the IM7/8552 woven laminate with EPN 12 μm NPN produced with VBO and oven at the 76.2 mm (3-inch) scale. The two scanned specimens are of the same laminate, but from different locations. This laminate has the highest void content of the manufactured 76.2 mm (3-inch) laminates. Noticeable voids are present throughout the laminate at the utilized pixel size with the laminate void content being 1.843 vol%. This scan was produced using 1.87 μm pixel size, 4 second exposure, voltage of 80 kV, and with a LE3 filter. 104

6.9 Representative cross-sectional view of the IM7/8552 woven laminate with AD PI aerogel NPN produced with VBO and oven at the 76.2 mm (3-inch) scale. The two scanned specimens are of the same laminate, but from different locations. The void content of this laminate is 0.16 vol%. This laminate has the lowest void content of the manufactured 76.2 mm (3-inch) laminates. This scan was produced using 2.01 μm pixel size, 4 second exposure, voltage of 80 kV, and with a LE3 filter. 105

6.10 Representative cross-sectional view of the IM7/8552 woven laminate with AD PI aerogel NPN produced with VBO and oven at the 152.4 mm (6-inch) scale. The two scanned specimens are of the same laminate, but from different locations. The void content of this laminate is 0.112 vol%. This laminate is beneath the void content limit of 1 vol% often required for aerospace composite structures. This scan was produced using 1.68 μm pixel size, 4 second exposure, voltage of 80 kV, and with a LE1 filter. 106

6.11 A visual demonstrating the calculation process for void vol% for all CFRP manufactured laminates. 10 TIFFs are completed for each analyzed laminate to obtain a void vol%. Voids are represented by red regions, while non-voids (resin, fiber, NPN) are represented by green regions. In the figure, 2.25 void vol% represents the calculated void area (colored red) of the example TIFF. 108

6.12 Void vol% of all VBO-manufactured IM7/8552 woven composites, including a standard error bar. The face colors of the bar chart, red, blue, green, and purple, indicate the applied NPN of no NPN, SCD PI aerogel, AD PI aerogel, and EPN 12 μm, respectively. 109

List of Tables

4.1 Reduction in height from the vertical alignment to horizontal alignment of CNTs. Each listed grown-height sample thickness is an average of four measured values per sample, while each SEM measured thickness is an average of three measured values per sample. 55

4.2 Microstructural characterization summary of the investigated NPN material families used for CFRP composites and other NPN sized materials, along with reference to the manufacturer. MFP Pore Size includes a factor of 0.715 to account for asymmetric pore geometry. 69

6.1 Material characteristics for IM7/8552 prepreg composite system [46]. 95

6.2 All VBO-manufactured woven IM7/8552 square, flat-panel composite laminates studied. In brackets is a reference to the representative μCT scan of that laminate. Each laminate name contains the side length of the manufactured laminate in inches. All laminates are produced with the desolventing procedure at 60°C and ∼10 millibar for 60 min, including the laminate without NPN. 101

6.3 Void content percentages of the IM7/8552 VBO-manufactured laminates. The desovlenting process of ∼10 millibar and 60 °C was applied to all laminates for 60 minutes. To calculate these results, 10 evenly spaced TIFFs were selected from the reconstructed 2D slices using ImageJ. The standard error listed for each laminate is the standard deviation of the void vol% for the 10 TIFFs divided by the square root of the TIFF set population (10). 109

6.4 Average laminate thicknesses of baseline autoclave manufactured and oven and VBO-manufactured IM7/8552 $[0]_{12}$ woven composites, along with calculated standard error. Standard error is defined as the standard deviation of the 5 thickness measurements per laminate set divided by the square root of the sample size (5). 110

Abbreviations and Symbols

μCT	Microcomputed Tomography
A-CNTs	Aligned Carbon Nanotubes
AD	Ambiently Dried
ANL	Argonne National Lab
CFP	Capillary Flow Porometry
CFRP	Carbon Fiber Reinforced Polymer (Composite)
CNT	Carbon Nanotube
CPU	Central Processing Unit
CTE	Coefficients of Thermal Expansion
CT	Computed Tomography
CVD	Chemical Vapor Deposition
EPN	Electrospun Polymer Nanofiber
ESRF	European Synchrotron Radiation Facility
FRP	Fiber Reinforced Polymer (Composite)
GFRP	Glass Fiber Reinforced Polymer (Composite)
GNPT	Guaranteed Non-Porous Teflon

HA-CNTs	Horizontally Aligned Carbon Nanotubes
IUPAC	International Union of Pure and Applied Chemistry
LCM	Liquid Composite Molding
MFP	Mean Flow Pore
MRCC	Manufacturer Recommended Cure Cycle
NPN	Nanoporous Networks
OoA-VBO	Out-of-Autoclave Vacuum-Bag-Only
OoA	Out-of-Autoclave
OoO	Out-of-Oven
PAN	Polyacrylonitrile
PID	Proportional – Integral – Derivative
PI	Polyimide
Prepreg	Pre-impregnated Fibers
PTFE	Polytetrafluoroethylene
RFI	Resin Film Infusion
RF	Radio Frequency
RTM	Resin Transfer Molding
SCD	Supercritically-Dried
SCRT	Sychrontron Radiation Computed Tomography
SEM	Scanning Electron Microscopy
SPring-8	Super Photon ring-8 GeV
VA-CNTs	Vertically Aligned Carbon Nanotubes

VARTM	Vacuum-Assisted Resin Transfer Molding
VBO	Vacuum-Bag-Only
$\frac{dP}{dx}$	1D Pressure Gradient
κ	Permeability
μ	Dynamic Viscosity
∇P	Pressure Gradient
∇p	Gas Pressure at Flow Front
σ	Surface Tension
θ	Contact Angle
ε	Porosity
A	Cross-Sectional Area
D_f	Average Fiber Diameter
F	Form Factor
h_f	Flow Front Position
k	Through-Thickness Permeability
K_o	Kozeny Constant
k_{fiber}	Fiber Bed Permeability
n	Geometric Shape Factor
P_c	Capillary Pressure
P_{atm}	Atmospheric Pressure
$P_{c,fiber}$	Fiber Bed Capillary Pressure
P_i	Through-Thickness Permeability of Individual Membrane

P_{total}	Total, Average Through-Thickness Permeability
Q	Volumetric Flow
q	Darcy Velocity
Q_{perm}	Quantity of Permeant
r_m	Pore Radius
T	Temperature
t	Time
V_f	Volume Fraction
X_i	Thickness of Individual Membrane
X_{total}	Total Thickness

Chapter 1

Introduction

The motivation for aerospace-grade advanced composites manufacturing is provided in this chapter, followed by an outline of the thesis.

1.1 Motivation

Advanced composite materials have been developed and known for their structural properties and lightweight composition, leading to an extensive implementation into aircraft and spacecraft. Fiber reinforced polymer composites were evolved during World War II with an industry being generated near the end of the 1940s [1, 2]. By the 1960s, these composites were integrated more routinely throughout the aerospace sector in military and government funded vehicles, with a predominant focus on carbon fiber reinforced polymer (CFRP) composites within the transportation and aerospace industries [3–5].

CFRP composites are ideal for their high specific strength and stiffness, corrosion resistance, outstanding fatigue properties, and lightweight nature [6–10]. The advantages of CFRP for specific strength and specific stiffness are apparent in the Ashby chart [11] provided in Figure 1.1. Weight reductions enable less fuel consumption and greater payload weight allowances— critical areas of design for airplanes and spacecraft. The Boeing 787 Dreamliner 80 percent of structure being composite by volume and 50 percent composite

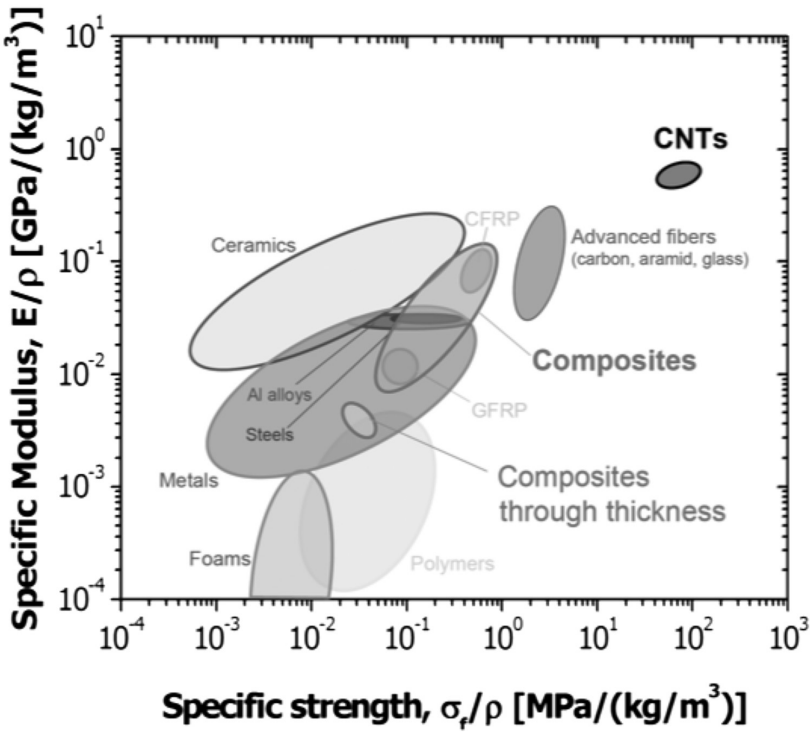


Figure 1.1: Specific modulus against specific strength Ashby plot for metal alloys, composites, and CNTs. From Wardle et al. [16].

by weight [12–14]. Alpha, a small-lift launch vehicle from the company Firefly, has the entire airframe and cryogenic propellant tanks produced from carbon fiber composites [15]. A S-curve visual depicting the usage of advanced carbon materials for a variety of aerospace vehicles is provided in Figure 1.2.

The large-scale utilization of CFRP composites in aviation and space vehicles demonstrates the increasing manufacturing demand needed to satisfy current aerospace technology development. Although these fiber reinforced polymer composites are more expensive to manufacture than traditional metals, the cost-savings from the reduced weight present a strong argument for their use throughout the aerospace industry.

Frequently used microfibers in FRP include glass or carbon, while the polymer matrices can include thermosets or thermoplastics, with the most common being epoxy thermosets in demanding aerospace applications. To process these composites, the use of an autoclave has been considered essential for many years [18]. An autoclave is a vessel that can provide

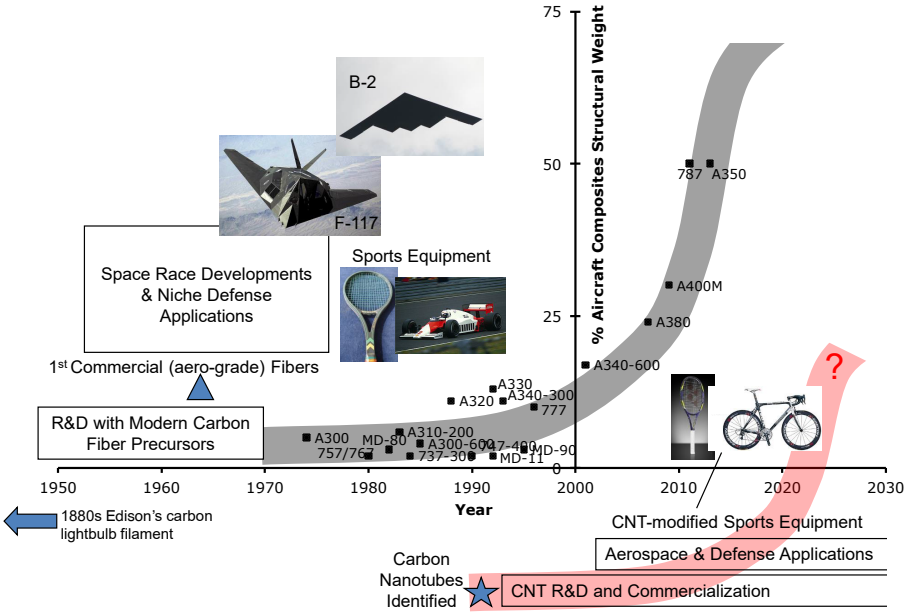


Figure 1.2: S-curve plot demonstrating advanced carbon materials within aircraft structures as a function of composite wt%. The upper curve represents advanced carbon fiber composites, while the lower curve represents CNT-based materials. From Gorbatikh et al. [17].

temperature and pressure requirements needed to consolidate thermoplastic composites or cure thermoset composites into void free laminates. Typically, an applied pressure of ~ 0.7 MPa (7 bars) is supplied by the autoclave to compress these laminates during curing, in a process that compacts the layers and extracts gases [19]. However, autoclaves have significant drawbacks associated with them due to their size and power requirements. One estimate of power consumption for autoclave manufacturing of composites gives 22 MJ/kg of composite [20]. In addition, thermal ramp rates are slow due to the convective heating nature of the tool, while geometric constraints must be considered when designing the desired parts due to the size limitation of the physical chamber. These energy, time, and design costs limit access to the production of CFRPs by smaller companies with relatively less funding and resources.

However, to circumvent these consequences associated with an autoclave, out-of-autoclave (OoA) techniques have been developed over the past couple of decades. One solution includes the creation of OoA prepregs under vacuum-bag-only (VBO) cure to produce low void-

content laminates [21], often with the use of an oven. A major drawback with this system includes long manufacturing times to prevent the dropping of the polymer resin viscosity, which would in turn block air or volatile extraction paths.

While ovens require significantly less energy than autoclaves, a new technique titled out-of-oven (OoO) has been recently developed to further decrease energy costs. Convective heating of an oven can be replaced with OoO conductive heating. A successful OoO method consists of applying the resistive heating of a carbon nanotube film to reduce energy consumption by over two orders of magnitude in comparison to an oven, with success being demonstrated with OoA thermoset and OoA thermoplastic CFRP pre-impregnated fibers (prepreg) [22–24]. Used in parallel with either an oven or OoO techniques, nanoporous networks (NPN) have shown potential to replace the autoclave pressure with capillary pressure within the interlaminar regions of composites [25–30]. The OoO and NPN technologies can be coupled with conventional, aerospace autoclave prepreg to produce aerospace-grade composites with less than 1 vol% void without the use of an autoclave [27, 28].

The research demonstrated throughout this thesis will investigate different NPN that can be used to replace autoclave pressure in the interlaminar regions for an autoclave aerospace-epoxy CFRP prepreg system. By demonstrating the versatility of this technique via expanded sets of NPN materials, an alternative, reliable manufacturing technique is produced to use with conventional aerospace prepreg to create low-void content structural aerospace-grade composites with reduced energy costs and geometrical manufacturing constraints.

1.2 Thesis Outline

Within this thesis, the selection, characterization, and VBO-manufacturing of CFRP composites with interlaminar inserted NPNs are demonstrated through woven IM7/8552 prepreg, a common aerospace CFRP composite system requiring autoclave curing. NPNs are microstructurally characterized to understand the effects of the NPN during the stages of the

cure cycle, including lamina-level resin flow behavior.

Chapter 2 provides background on autoclave and out-of-autoclave manufacturing techniques currently performed throughout the aerospace industry. These techniques will be discussed for their functionality and efficiency. Capillary flow porometry will be reviewed to assist in the explanation of flow behavior throughout the NPNs. A brief overview of X-ray computed tomography will be provided to enable further insights into later experiments designed for in situ resin flow monitoring.

Chapter 3 describes the objectives of the research and the techniques implemented to complete these goals.

Chapter 4 assesses the fundamental behavior of NPNs used in composites manufacturing. The selection of these materials, along with their characterization will be discussed in detail. For selected materials such as aligned carbon nanotubes (A-CNTs), the synthesis will be provided.

Chapter 5 provides an in-depth review of the in situ micro-computed tomography experiments that provide insight into the flow front of resin throughout the laminate, along with the void evacuation and development throughout the manufacturing cure cycle.

Chapter 6 explains the addition of NPNs into the laminate architecture and its effect on the void content quality of the composite. NPN-integrated laminates are oven-cured using VBO-manufacturing.

Chapter 7 summarizes the developments of previous chapters and outlines future work.

Chapter 2

Background

Throughout this literature review, the production and high-level properties of fiber reinforced polymer (FRP) composites are discussed. Their relevance within the aerospace industry is specified, with a focus on primary structures. Manufacturing methods of carbon fiber reinforced polymer (CFRP) composites are explored. Material classifications and microstructural investigation methodology is briefly introduced to provide groundwork for later chapters.

2.1 Traditional Production of Fiber Reinforced Polymer Composites

FRP composites consist of microfibers, usually stiff, and a polymer matrix, typically compliant, that binds together the reinforcing fibers [31]. Within the aerospace industry, continuous fiber reinforced composites are extensively used; these composites consist of long microfibers that can be placed unidirectionally or bidirectionally per lamina. Unidirectional microfiber laminae contain parallel microfibers in a singular direction. These unidirectional microfiber laminae can then be placed in a quasi-isotropic manner to construct homogeneous macroscopic structures. Common bidirectional laminae consist of a fabric structure, with the most common structural geometry being plain weave, twill weave, or satin weave [32]. There also

exists 2D braided fabric structures but this ventures into triaxial fiber orientation, geometry outside the scope of this project. The orientation and alignment of these fibers define the structural properties of the composite, while also affecting the manufacturing procedures.

FRP composites are predominantly categorized by natural or synthetic fibers [31]. Natural fibers are more abundant than synthetic fibers due to their prevalence in nature such as bamboo, flax, and hemp [33]. While highly accessible and environmentally compatible, natural FRP composites struggle to perform in extreme environments due to their high water absorption rates and reduced mechanical properties in comparison to synthetic FRP composites. Synthetic fibers are human-made fibers that are produced by chemical synthesis. Synthetic FRP composites are conventionally used for primary structures throughout the aerospace industry. Glass fiber and carbon fiber are the two most utilized synthetic microfibers. Glass fibers are less expensive than carbon fiber, non-magnetic, electrically and thermally insulating, radio frequency (RF) transparent, and can be optically transparent [34]. Carbon fibers have lower densities than glass fiber, possess high specific modulus and strength compared to other fibers, are electrically conductive, and are X-ray transparent [35]. Carbon fibers are more thermally conductive than glass fibers and possess negative coefficients of thermal expansion (CTEs). For spacecraft and aviation vehicles, CFRP composites are a prevailing material choice for increased weight savings, improved mechanical performance, and desirable thermal performance.

Traditionally, polyacrylonitrile (PAN) is the precursor for carbon fiber manufacturing. After thermally stabilizing the PAN fibers in an oxygen environment for a designated period of time, the PAN fibers are converted into carbon fiber through pyrolysis in an inert atmosphere above 1000 °C [36], usually at 1800 °C [37]. Once these carbon fibers are fabricated, they are arranged into dry fabric cloths or pre-impregnated fibers (prepregs) in unidirectional or bidirectional configurations. Prepregs are advantageous for swift manufacturing processes and controllable resin accumulation within parts [38]. Thermoset prepreg systems are manufactured via solution-dip impregnation or the hot-melt method, with the applied

thermosetting resin being B-staged, or partially cured. The hot-melt method utilizes a thin layer of resin on a conformable substrate. The reinforcing fiber and heated thin layer of resin are applied to each other through rollers [39]. The now impregnated fiber is passed through a cooled plate to terminate any reactions. The solution-dip impregnation process, commonly used for woven fabrics, involves dipping the dry fabric into a mixture of resin and solvents to impregnate the fibers. The solvents are used to to lower the viscosity to improve infiltration. Once infused to a predetermined amount, the prepreg is sent through a drying chamber to remove solvents, but often residual solvent remains in the prepreg [40, 41].

2.2 Manufacturing Processes with Carbon Fiber Reinforced Polymer Composites

2.2.1 Autoclave Manufacturing

Widely used for advanced polymer matrix composites in aerospace, autoclaves provide a consistent and reliable source of convective heating and high pressures to minimize void content (under 1 vol%), ensure fiber wetting, and stimulate polymer cross-linking reactions in the creation of structural thermoset polymer composites [42]. In addition to thermoset composites, autoclaves consolidate thermoplastic composites, generally at temperatures above 300 °C, while thermoset-based composites cure within 200 °C [43]. To prepare typical aerospace-grade CFRP composite flat panels from thermoset autoclave prepreg, the investigated structures within this study, the precut prepreg sheets are laid onto a tool with predetermined ply orientations for a layup [44]. The part is then placed in a vacuum bag assembly to remove trapped air and consolidate the fiber reinforced polymer laminae during the cure.

In Figure 2.1, a vacuum bag system is shown for typical autoclave runs. The vacuum bag assembly is placed into the autoclave where pressurized and high temperature gas, usually air, nitrogen, or carbon dioxide, is applied to the system following a manufacturer recommended

cure cycle (MRCC) — curing the composite. An example of a typical MRCC for epoxy aerospace CFRP is shown in Figure 2.2 for 8552 composite systems; this is the 8552 polymer matrix system studied in this thesis. Conventionally, epoxy resin-based laminates, the most common thermoset resin composites used for demanding aerospace applications, are cured under pressure conditions of 0.7 MPa (7 bar) to suppress void growth, while vacuum is applied to remove air and volatiles trapped within the laminates [45]. The temperature is ramped to a predetermined value to lower polymer resin viscosity, enabling void removal from the laminate and laminate consolidation, and to begin curing the epoxy resin via cross-linking. Dwelling at this temperature after the ramp promotes the gelation of the resin. At this holding stage, resin flow and laminate consolidation continue, but epoxy resin viscosity increases. After the first dwell, the temperature is raised to the final curing temperature and held at this value to complete the cure reaction. The viscosity continues to increase, but is maintained at a value that allows fiber wetting and laminate consolidation until the cure is complete. This process typically is on the order of hours. While some MRCCs have one ramp and one hold, the two ramp and two hold cure cycle shown in Figure 2.2 is more common [30].

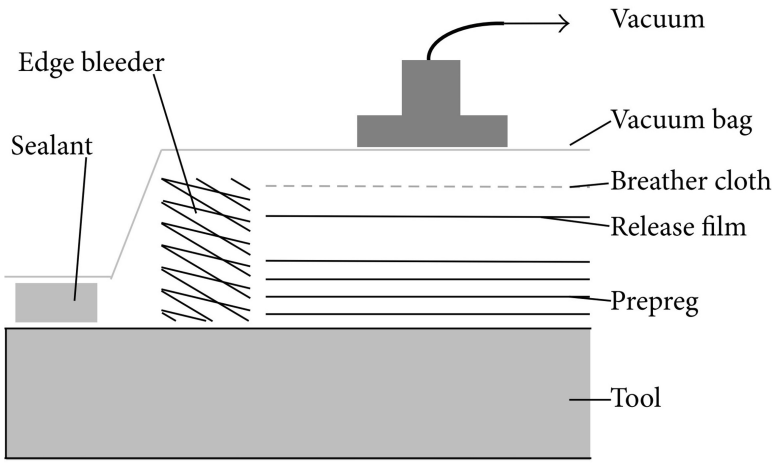


Figure 2.1: Common vacuum bag system procedure for autoclaves for curing of composites. Edge bleeder is only utilized for select aerospace CFRP composite systems. Adapted from Drakonakis et al. [38].

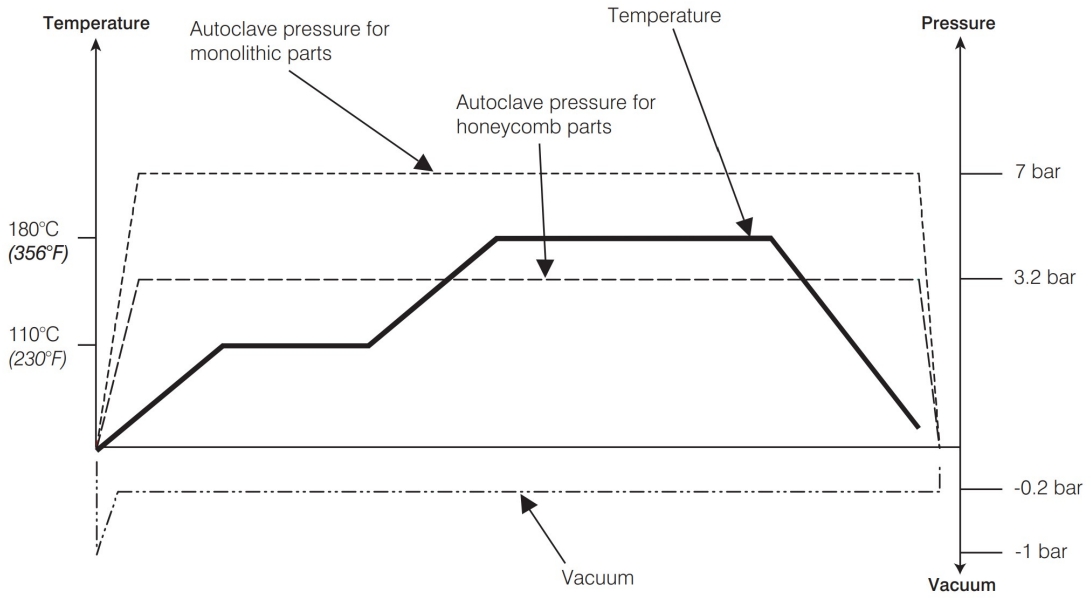


Figure 2.2: Manufacturer Recommended Cure Cycle (MRCC) for 8552 based composites. The bold line represents the temperature profile of the cure cycle, the dash-dotted line at the bottom of the graph represents the vacuum applied to the component, and the two upper dashed lines demonstrate the supplied autoclave pressure dependent on part type. From [46].

While reliable, these autoclaves have disadvantages. Autoclaves have relatively large energy and operating costs [47, 48], that scale in size with the manufactured part size. For context, to manufacture the carbon composite wings of Boeing 777X aircraft, 36.6 m (120 ft) long autoclaves are used to process these structures [49]; this is approximately 1/3 of an American football field. Outside of procedural costs, thermal gradients exist during the cure due to the convective nature and large size of the autoclave, leading to residual stresses within the cured component and non-uniform part cure [50, 51]. Geometrical constraints are often placed on the manufactured laminates due to tooling availability or physical limitations of the autoclave [52]. Moreover, availability of the autoclave can be an issue due to high demand, which consequently can limit production rates [22]. Altogether, autoclaves are well-established and reliable in the manufacturing of aerospace-grade CFRP composites, but have significant disadvantages that provide a compelling need for alternatives.

2.2.2 Out-of-Autoclave (OoA) Manufacturing

To mitigate the disadvantages of autoclave manufacturing, out-of-autoclave (OoA) techniques have been developed to process FRP composites since the late 1990s. One popular technique is creating prepreg that can be processed without an autoclave using vacuum-bag-only (VBO) curing. Out-of-autoclave vacuum-bag-only (OoA-VBO) prepregs use various technologies to allow processing without an autoclave, with most being partially impregnated for the creation of gas migration channels [21]. Entrapped air from layups, volatiles from residual solvents, and vaporized moisture can all be removed via these pathways. Figure 2.3 demonstrates the resin infusion difference between OoA-VBO (partially infused) and autoclave-formulated (fully infused) prepreg examples. The in-plane permeability of the laminate requires long (relative to overall cure time) room-temperature vacuum holds for debulking, sometimes for the entire laminate, and sometimes for groups of plies. As the cure progresses, with increasing temperature, the resin flows into dry channels to fill any non-resin saturated region, barring volumetric constraints.

However, it is essential to note the role of resin viscosity during this process. With low resin viscosity, resin starvation in the laminate or resin bleeding can occur; with high resin viscosity, voids may not have enough pressure to evacuate the surrounding resin region [53]. A maximum pressure of 101 kPa or 1 atm is applied during the OoA-VBO manufacturing process due to the constraints of vacuum bagging [54]. Using this process, theoretically no voids should exist due to gas removal and resin migration; however, this does not always occur. This processing method reduces energy consumption, but manufacturing time concerns and complex geometry constraints remain with the OoA technique [21]. Additionally, OoA-VBO prepreg parts typically have larger void contents compared to their autoclave prepreg counterparts. Provided void vol% estimations are 0 to 1 vol% for autoclave prepreg parts and 0.5 to 3 vol% for OoA prepreg parts after respective curing processes [55].

Other common manufacturing processes that can be performed without an autoclave

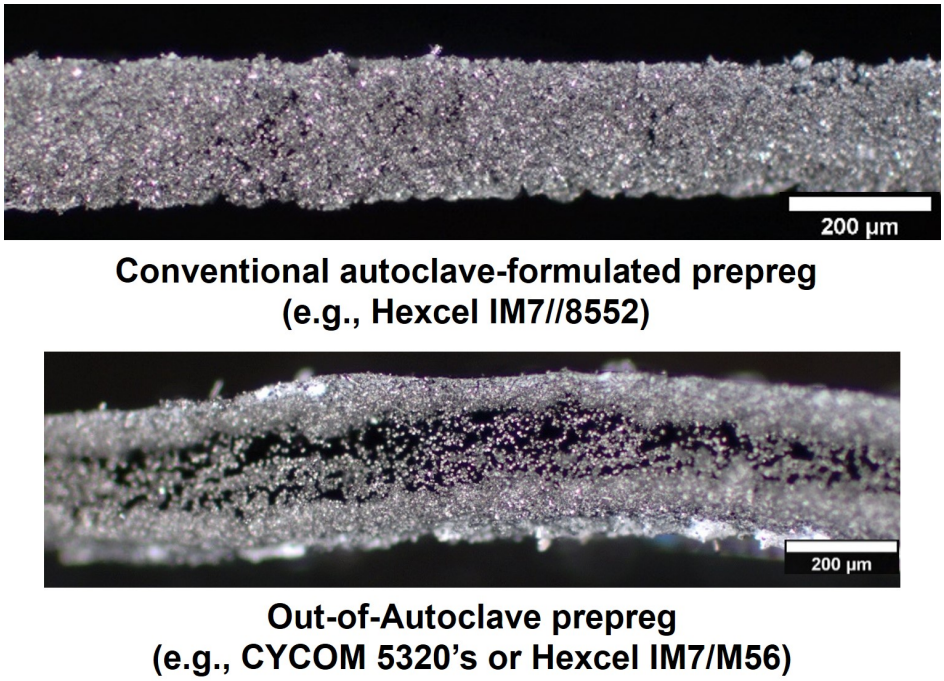


Figure 2.3: Two types of prepreg are presented: (Top) IM7/8552 autoclave prepreg and (Bottom) IM7/M56 out-of-autoclave prepreg. Optical micrographs captured by Dr. Jeonyoon Lee (former student of necstlab, a research group at MIT).

include resin film infusion (RFI), resin transfer molding (RTM), and vacuum-assisted RTM (VARTM) [56], three manufacturing forms of liquid composite molding (LCM). RTM consists of using a dry or semi-dry fiber perform placed inside of a closed mold where resin is injected into the enclosed space at a specific flow rate. This technique lends itself useful to creating complex 3D structures [57], with low tooling costs. While able to control the volume fraction of resin within a part, the local velocity can vary considerably throughout the part's geometry at the micron scale, leading to non-uniformity of the manufactured component [58]. VARTM is a similar process to RTM except with the usage of vacuum to facilitate resin flow throughout the structure. High-quality parts used for the aerospace industry are commonly produced with this method, but surface finish differs per exterior and there exists part thickness variation within larger components [19, 59, 60]. Lastly, RFI places films of B-staged resin between the laminae of the laminate, or on the top and bottom of the laminate, in an open mold where vacuum is applied to typically produce rib or stiffened structures

[61, 62]. Of the three manufacturing LCM techniques, RTM or VATRM provides superior internal and external surface quality, but has limitations in overcoming dry region emergence [63]. LCM, a common replacement of autoclave prepregging, still results in expensive manufacturing and oftentimes lower-performance parts [55].

This inventory of OoA manufacturing techniques is not all-encompassing, as many new developments are being advanced to replace the need for autoclaves. However, the benefits of autoclave aerospace-grade prepreg are introduced throughout this section. In this thesis, a manufacturing technique without the use of an autoclave will be used to process aerospace-grade autoclave prepregs. The process will be described in the following section and with additional detail in later chapters.

2.2.3 Nanoporous Network (NPN) enabled OoA Manufacturing

Another manufacturing approach, and primary focus of this thesis, is the use of nanoporous networks (NPN) to produce aerospace-grade CFRP laminates without the use of an autoclave. Using nanomaterials in the interlaminar regions of the composites, capillary pressure can replace autoclave pressure to produce void free interlaminar interfaces. Through the porous nature of the materials, polymer resin flows through the pores of the NPN. The capillary effects of the air interface and flowing polymer within the pore create a localized pressure that pulls the prepreg resin into the NPN from the surrounding lamina, thereby eliminating any voids that may exist within that region. Interlaminar voids are known to detrimentally affect mechanical properties like interlaminar shear strength, fatigue resistance, and flexural strength [25]. Void-free unidirectional CFRP laminates, including those of L-shaped geometry, have been manufactured with electrospun polymer nanofibers (EPN) or vertically aligned carbon nanotubes (VA-CNT), two types of NPNs [25, 28, 64]. NPN-enabled OoA manufacturing has been exclusively used with autoclave thermoset prepregs to date, but has the potential to be applied in other manufacturing processes. A schematic, Figure 2.4, underlying the use of carbon nanotubes as a NPN is provided [25].

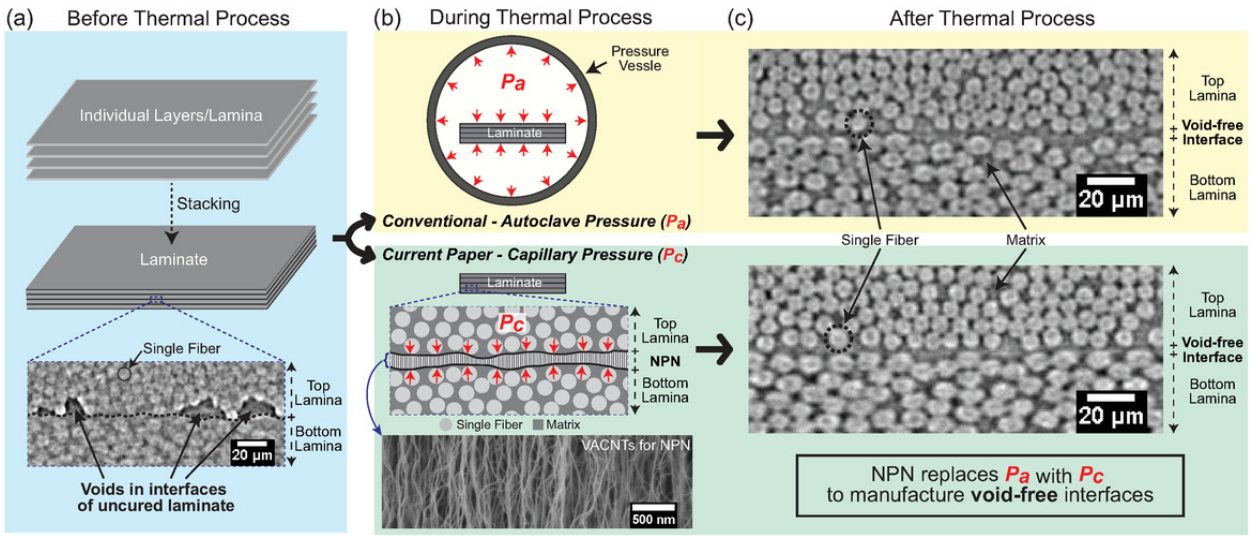


Figure 2.4: Nanoporous network (NPN) manufacturing with carbon nanotubes in the interlaminar region of a composite. Figure from Lee et al. [25].

While NPNs replace the pressure provided by an autoclave, high temperatures are still needed to complete the cure of these CFRP laminates. By using a convective oven, there are significant energy savings compared to the use of an autoclave due to the removed requirement of pressurized gas. Through using a conductive out-of-oven (OoO) heating method enabled by aligned carbon nanotubes (A-CNT), even more energy savings can be realized utilizing the resistive heating of A-CNTs. Former studies have shown a decrease in energy consumption by two orders of magnitudes via conductive A-CNT resistive heaters compared to an convective oven, with no reduction in mechanical properties of the manufactured laminates [22, 23, 65]. Using solely OoO techniques, there has been success with OoA thermoset and OoA thermoplastic CFRP prepreg [22–24]. However, pairing OoO with the use of NPNs has resulted in the low void content manufacturing of unidirectional aerospace-grade autoclave prepreg [28, 30]. For this thesis, manufacturing of the composite laminates will be completed with the assistance of an oven for woven CFRP laminates, with future work indicating the application of OoO to manufacture autoclave woven composites.

2.3 Nanoporous Networks (NPNs)

For differing applications and fields, the term nanoporous can refer to materials with a varying range of pore sizes. In the creation of nanoporous polymer networks for gas storage or environmental separations, porous materials are categorized by the International Union of Pure and Applied Chemistry (IUPAC) into the following groups: macroporous materials having pore diameters larger than 50 nm, mesoporous materials having pore diameters between 2 and 50 nm, and microporous materials having pore diameters less than 2 nm [66, 67]. The NPNs in this thesis encompass the scope of mesoporous and microporous materials by the definitions of IUPAC. Commonly, in medical and biological applications such as drug delivery systems or immunoisolation devices, nanoporous membranes are distinguished with pore sizes that range between 1 to 100 nm [68]. Metallic nanostructures are divided into nanoporous networks and foams, where these networks range similarly to the medical-based nanoporous membranes and the foams range from sub-micrometers to centimeters [69, 70]. With applications in hydrogen storage, filtration, desalination, lightweight structures, and catalysis processes, the necessary pore range differs per function [70, 71].

Alongside the quantitative size of the pore, there are other characteristics that are important in the classification of any porous materials. Pores can be qualitatively classified as closed or open [72]. Open pores indicate surface connectivity throughout the material allowing fluid flow, while closed pores are better described as voids with a maximum of a single, exposed open face. The morphology of the pore is another consideration of nanoporous materials, when determining the intrinsic properties of the material such as thermal conductivity, permeability, and diffusivity [73]. The tortuous, or conversely straight, path that fluid flow occurs along varies widely across material types, regardless if materials share similar pore sizes [74].

In the application of composites manufacturing, NPNs are materials that have pore diameters ranging from tens of nanometers to several micrometers. Generally, these materials

are polymeric for their conformability, compressibility, and possess a temperature tolerance of over 200° C, a common temperature needed for cure cycles of aerospace-grade epoxy-based CFRP composites.

2.4 Capillary Flow Porometry (CFP)

Capillary flow porometry (CFP) characterizes open, or through-pore dimensions, pore distributions, and gas permeabilities of nanoporous and microporous materials [75]. This characterization method is often implemented for EPN membranes, batteries, paper, and zeolites [76, 77]. This experimental technique is based on Darcy's Law (Equation 2.1 or Equation 2.2) and the Young-Laplace equation (Equation 2.3). By using Darcy's Law, the permeability of tested materials can be established. Darcy's Law for isotropic porous mediums is as follows:

$$q = -\frac{\kappa}{\mu}\nabla P \tag{2.1}$$

where q, κ, μ, and ∇P are the Darcy velocity , permeability of the porous medium (in tensor form), dynamic viscosity of the fluid, and the pressure gradient, respectively.

With the conditions of cylindrical ideal pores, one-dimensional flow, incompressible fluid, and laminar flow, results in the Darcy's Law used throughout this experimental technique:

$$Q = \frac{k}{\mu}\frac{dP}{dx}A \tag{2.2}$$

where Q, k, μ, $\frac{dP}{dx}$, and A are the volumetric flow, through-thickness permeability of the porous medium (scalar), dynamic viscosity of the fluid, the 1D pressure gradient, and cross-sectional area, respectively. Although Darcy's Law, Equation 2.1, is for isotropic mediums, this equation remains suitable in this CFP due to the one-dimensional flow assumption. To determine the pore size of the tested materials, Young-Laplace equation (Equation 2.3) is

utilized.

$$P_c = \frac{2\ \sigma\ \cos(\theta)\ n}{r_m} \tag{2.3}$$

where P_c, σ, θ, n, and r_m are the capillary pressure, surface tension of the fluid, contact angle between the liquid and solid surfaces, geometric factor, and radius of the cylindrical pore, respectively.

Pore size of untested materials is generally undetermined before the experiment, so dry curve data collection is executed before collecting data points of the wet curve to prevent pore shrinkage from capillary effects. For the dry curve data collection, an inert gas is introduced to the sample via the pressure tube in increasing amounts of pressure. As the pressure of the flowing gas is increasing, the respective flow rate is measured downstream of the sample as shown in Figure 2.6. Additionally, a half dry curve, a curve with half the slope of the original dry curve, is produced analytically. Using Darcy's Law, the through-thickness permeability of the sample can be calculated with the dry curve data, knowing the sample thickness. Using a wetting liquid with a low vapor pressure, low surface tension, and zero contact angle, the sample is fully saturated and the wet curve follows the same procedure as the dry curve data collection. In the wet segment of the experiment, the wetting liquid is removed from larger pores initially due to inverse, linear relationship of capillary pressure and radius shown in the Young-Laplace equation (Equation 2.3). Figure 2.5 displays the removal of wetting fluid as a function of pore size and can be used with Figure 2.6 to understand the through-pore composition of the tested membranes.

To determine the range of capillary pressures a material possesses, the dry curves and wet curve are analyzed with respect to each other. Shown in Figure 2.6 is a representative diagram of the pore classifications and relationships between the CFP obtained curves. The first bubble point correlates to the moment when the largest pore of the sample has the wetting liquid replaced with the flowing nitrogen gas, signifying the capillary pressure of that orifice and the first non-zero flow rate of the wet run. The smallest pore correlates

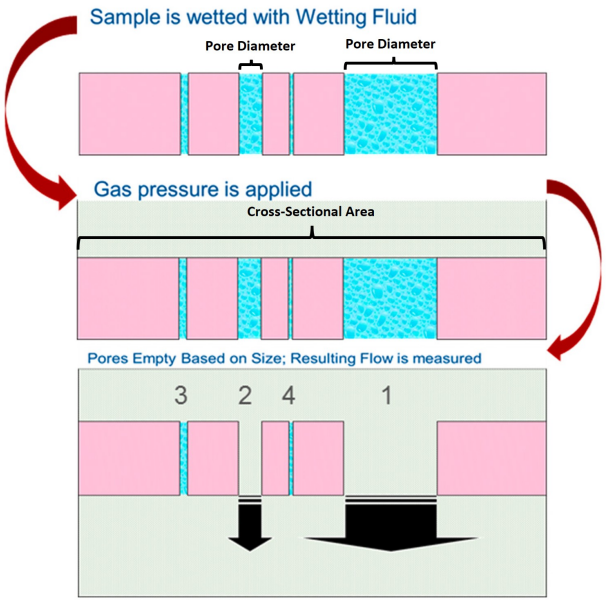


Figure 2.5: Illustration of the removal of wetting fluid within the pores of a porous membrane via applied inert gas. The numbers at the bottom of the figure represent the order in which the wetting liquid is removed from the pores; 1 represents the first pore emptied of the wetting liquid. Adapted from [78].

to the instance when the dry curve and wet curve align back together [79], indicating full material dryness. At this point, the membrane is completely dry and only nitrogen is flowing through the pores. The range of capillary pressures of a material exists from first bubble point pressure to the smallest pore pressure. The mean flow pore pressure represents the pressure at which half of the total gas flow can pass through the tested sample. In this thesis, the mean flow pore pressure is used as the representative capillary pressure of the nanoporous networks, while acknowledging the entire range of pressures that exist within a sample.

2.5 X-Ray Computed Tomography

An established approach of quality monitoring for composites, especially of novel manufacturing techniques, includes the use of X-ray computed tomography (CT) [81–85]. Both synchrotron radiation computed tomography (SCRT) and microcomputed X-ray tomogra-

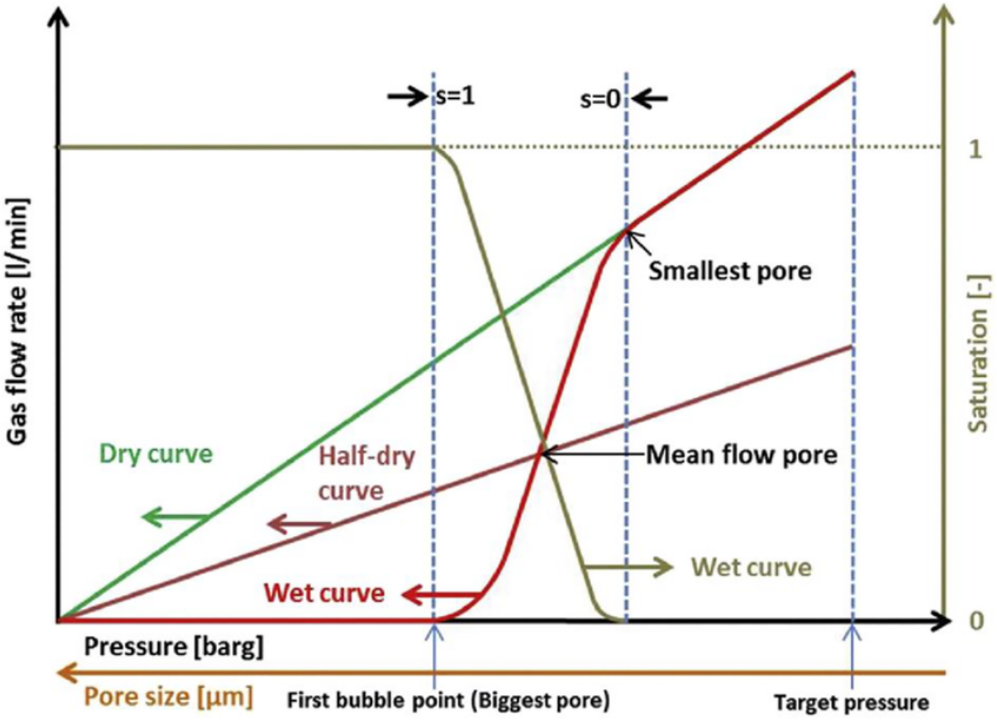


Figure 2.6: Diagram of three curves— dry curve (green), half-dry curve (maroon), and wet curve (red)— obtained during CFP, along with classification of pore categorization and saturation status (s). The half-dry curve is obtained analytically, while the dry and wet curve are measured directly from the experiment. The saturation of the membrane during the wet curve portion of CFP is shown by the green line labelled wet curve in the same hue as the saturation axis. The pressure is in units of barg (pressure in bars above atmospheric pressure) for this figure. From Bromberger et al. [80].

phy (μCT) are in common use for many visualization and characterization experiments. Lab-based μCT is used herein. Other non-destructive characterization instruments such as ultrasonic C-scan and infrared thermography lack the high resolution provided by CTs [86]. The three most fundamental components of any CT scanner are the X-ray source, the X-ray detector, and the sample platform [87]. In the case of centimeter-sized or millimeter-sized samples, the sample rotates while the source produces the high-energy photons and the detector receives the downstream electromagnetic waves [88]. In Figure 2.7, the relationship of the sample position compared to the source and detector is easily evident. As the sample moves closer towards the source and farther from the detector, the projection extends over more pixels of the detector, thus enhancing the resolution of the image. However, enhanced

resolution of images results in longer scanning times. Following the completion of the scan, the projections are reconstructed to create a 3D volume representation of the scanned specimen. In the case of composites quality monitoring, the reconstructed 3D volume assembles a visualization of the void, resin, and fiber volume fraction percentages of the structure. Densities of the captured materials are portrayed by a range of gray scale colors.

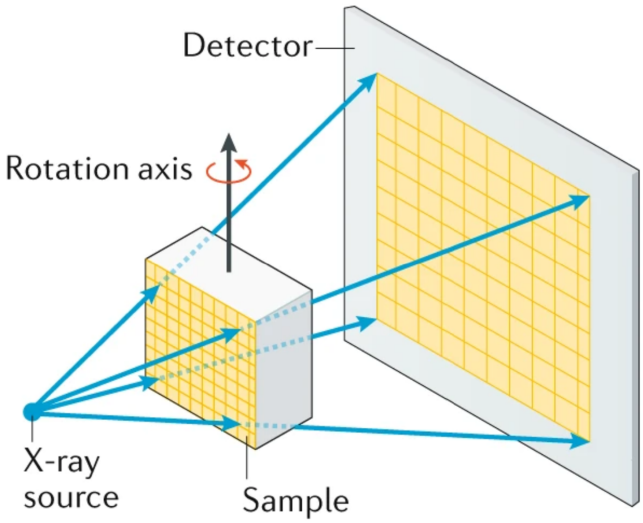


Figure 2.7: Schematic of cone beam systems common in laboratory-based microcomputed tomography (μCT) tools. Provided by Withers et al. [87].

In the interest of significantly reducing scanning times or capturing 4D material processes, synchrotrons are vital tools for bulk sub-second observations with sub-micron voxels [89]. Modern synchrotrons accelerate electrons to high relativistic velocities, near the speed of light (299,792 km/s) [90], in storage rings with magnetic particle accelerators to produce high brilliance, or high brightness, collimated X-rays. High brilliance X-rays penetrate through thicker materials, produce high resolution images, and allow for fast measurements for time-based imaging. Synchrotron radiation CT utilizes parallel beams X-rays, also improving the image quality. There are numerous synchrotron light sources situated throughout the world with widely known facilities such as Super Photon ring-8 GeV (SPring-8), the European Synchrotron Radiation Facility (ESRF), and Argonne National Lab (ANL). This thesis utilizes lab-based μCT.

2.6 Summary and Conclusions

CFRP composites are extensively used throughout the aerospace industry for a variety of vehicles and primary structures. Commonly used to fabricate these structures are autoclave-formulated prepregs that are cured and processed via autoclaves, leading to large energy consumption and part geometrical constraints. Alternative, OoA production procedures are available including OoA prepreg, liquid composite molding, and NPN-enabled OoA manufacturing. This thesis will focused on NPN-enabled OoA manufacturing of aerospace-grade autoclave-formulated prepreg for low void content composites to replace the need for autoclaves. CFP and μCT are used to study the integration of NPNs within these CFRP laminates.

Chapter 3

Objectives and Approach

The objectives of this thesis, along with the approaches to achieve these objectives, are listed below and demonstrated in full throughout Chapters 4, 5, and 6. Chapter 4 will target the fundamentals of nanoporous networks (NPN) and the underlying characteristics that allow for successful integration within woven IM7/8552 carbon fiber reinforced polymer (CFRP) composite laminates. Chapter 5 will discuss the experimental in situ observations of the IM7/8552 CFRP composites during steps of their cure cycle through the use of X-ray microcomputed tomography (μCT). Chapter 6 will demonstrate the oven-curing and vacuum-bag-only (VBO) manufacturing of NPN-integrated woven CFRP laminates, along with their void vol%.

3.1 Objectives

As the focus of this thesis prioritizes the fundamentals of NPNs and their integration within aerospace-grade CFRP composite laminates, the following objectives will be explored throughout this study:

- Expand the inventory of NPN materials that could be applied in a variety of composite systems and implement them in a preliminary Ashby guideline

- Measure the inherent microstructural properties — capillary pressure, permeability, and thickness — of NPNs to understand their behavior in the interlaminar region of CFRP laminates
- Manufacture woven CFRP laminates with a range of NPNs to investigate whether NPNs can effectively remove or reduce voids in the interlaminar region of laminates
- Develop in situ X-ray μCT experiments to observe the time-based resin infusion through the NPNs as a function of temperature and to investigate void evolution throughout a composite's cure cycle

3.2 Approach

To achieve these objectives, a variety of experiments and literature reviews are completed to ensure proper material selection, understand material characteristics, and quantify the effects of these added NPNs. Thus, the usage of NPNs can be validated as an alternative manufacturing technique of aerospace-grade CFRP laminates, in comparison to the autoclave, for significant energy savings. The approaches for the previously mentioned objectives are listed below:

- Utilize X-ray μCT, scanning electron microscopy (SEM), and capillary flow porometry (CFP) to obtain the microstructural characteristics of NPNs
- VBO-manufacture woven, flat-panel CFRP composites with electrospun polymer nanofibers (EPN) and polyimide (PI) aerogel films to determine whether these NPNs can remove or reduce voids in the interlaminar region of laminates using manufacturer recommended cure cycles (MRCC)
- Quantify the quality of the laminates through calculating the void vol% of these laminates using X-ray μCT

- Use X-ray μCT and design a thermal-mechanical system to heat and cool autoclave prepreg at pre-determined temperatures for observations of resin flow and void evolution for CFRP laminates (including with NPNs)

3.3 Limitations of Current Work

There are some limitations of the current work presented within this thesis. Mechanical testing of the VBO-manufactured CFRP laminates with NPNs will not be presented, as it is in progress. All selected NPNs are commercially available for ease of integration into large-scale manufacturing. Thus, the provided Ashby chart in later chapters is not all-encompassing. Other CFRP systems can be and have been investigated with the usage of NPNs; however, this thesis will focus on the IM7/8552 system, an autoclave prepreg commonly used for primary composite aerospace structures.

Chapter 4

Fundamentals of Nanoporous Networks

Nanoporous networks (NPN) herein refer to open porosity materials used in fiber reinforced polymer (FRP) composites manufacturing that have pore diameters ranging from tens of nanometers to several micrometers. Typically, these materials are polymeric, in the form of thin membranes, and have melting temperatures above 200 °C, a common maximum cure temperature for epoxy-based FRP composites. Before this thesis, three material types of nanoporous networks were investigated with unidirectional carbon fiber reinforced polymer (CFRP) and glass fiber reinforced polymer (GRFP) laminates - electrospun polymer nanofiber (EPN) mats, supercritically dried (SCD) polyimide (PI) aerogel films, and (seminally) vertically aligned carbon nanotubes (VA-CNTs) [30, 91–93]. While the initial fundamentals of NPNs were established, no extensive characterization of the materials was completed. Within this chapter, fundamental characteristics of NPNs, as they function within composite interlaminar regions, is discussed. The microstructural characteristics of the NPNs are investigated and compared to other common, engineering porous materials to provide a seminal Ashby plot of their behavior focusing on capillary pressure and permeability.

4.1 Selection of NPN Materials

An expansive list of commercial materials is selected to broaden potential composite manufacturing, while also providing a reference to popular engineering porous materials. Within this section, the synthesis and selection of these nanoporous materials are described in detail.

4.1.1 Creation of Carbon Nanotube Thin Films

Implementing CNTs in the interlaminar regions of composites has been executed through the use of VA-CNTs for the purpose of increasing fracture resistance and reinforcing this resin-rich region. As a multifunctional benefit, VA-CNTs can also reduce voids in the interlaminar regions of unidirectional composites when used as an NPN, introduced by Lee et al. [25, 93]. To manufacture these arrays of VA-CNTs, also called forests, a chemical vapor deposition (CVD) process is performed. Beginning with silicon wafers that are layered with 500 nm of SiO_2, 10 nm of Al_2O_3 and 1 nm of Fe are deposited onto the wafer via electron beam physical vapor deposition. These bulk wafers are cleaved into 30 mm by 40 mm substrates. The cleaved substrates, removed of any debris using the adhesion of scotch tape, are placed within a 44 mm inner diameter quartz furnace where C_2H_4, He, and H_2 gases, along with water, are supplied to the wafer surface to promote multi-walled CNT growth and weaken adhesion to the underlying substrate [94]. To grow the CNT forests utilizing the CVD process, C_2H_4 is used as the carbon source and He as the carrier gas at 680°C in atmospheric pressure. Flowing C_2H_4 for 170 seconds produces VA-CNT forests with an approximate height of 100 microns - the preferred height for the studies in this thesis. After growth, the C_2H_4 flow is terminated and H_2 gas is supplied to promote delamination between the forest and the base substrate [95]. The volume fraction of these synthesized forests are 1 vol% CNT with an average outer CNT diameter of $\sim$ 8 nm and an average inter-CNT spacing (outer wall to outer wall) of $\sim$ 60 nm [96, 97]. Using a Carl Zeiss Axiotech 30 HD optical microscope, four locations on the wafer are selected and measured for their height, with the average of

these results being the representative height of the forest. Once the VA-CNTs are grown to their final height of approximately 100 microns, a porous polytetrafluoroethylene (PTFE) film (Omnipore®), of manufacturer stated pore size 0.2 μm, is placed over the forest of CNTs to create a two-layer film for testing. A backing or support layer, the porous PTFE membrane, is needed to ensure that CNTs are not pushed through the porometer due to the pressure of the nitrogen gas. Additionally, VA-CNTs have not been successfully measured for capillary pressure due to the significant capillary densificiation that occurs as the wetting liquid is applied; thus, creating large voids throughout the structure leading to incorrect characterization. Using a rounded blade, the PTFE film is mechanically flattened against the forest of VA-CNTs to create a final product of horizontally-aligned carbon nanotubes (HA-CNTs) on a PTFE substrate. A schematic showing the process is shown in Figure 4.1. The red arrows indicate the movement of the rounded blade against the PTFE membrane onto the VA-CNT forest. Using scanning electron microscopy (SEM), example shown in Figure 4.2, the thicknesses of the HA-CNTs on top of the PTFE membrane are measured for the grown heights of 103 μm, 108 μm, 111 μm and are listed in Table 4.1 below.

Table 4.1: Reduction in height from the vertical alignment to horizontal alignment of CNTs. Each listed grown-height sample thickness is an average of four measured values per sample, while each SEM measured thickness is an average of three measured values per sample.

Grown VA-CNT Forest Height	SEM Measured HA-CNT Thickness
103 μm	6.4 μm
108 μm	8.4 μm
111 μm	5.5 μm

Along with creating aligned CNT membranes for testing, commerical CNT buckypaper was also selected for characterization. Using CNT buckypaper from Tortech Nano Fibers of 7 gsm and thickness of 21.8 μm, measured by microcomputed tomography (μCT), the microstructural characteristics were measured and compared against HA-CNT membranes in section 4.3.

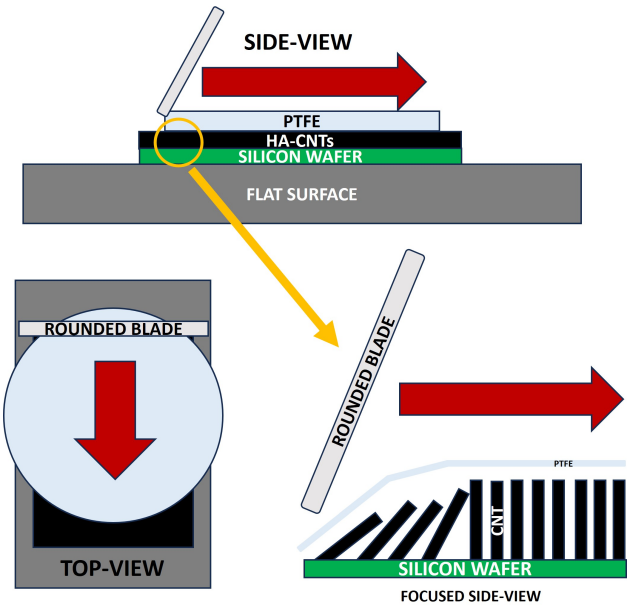


Figure 4.1: Illustration of CNT knockdown process using PTFE circular cutouts. The black rectangles represent CNTs, the flexible, blue circle represents the Omnipore® PTFE membrane, the gray rectangle represents the rounded blade, the green rectangle represents the silicon substrate where the VA-CNT array is grown on, and the red arrow demonstrates the direction of the blade's force. This figure was created by Grant Oh, an undergraduate researcher of necstlab, a research lab at MIT.

4.1.2 Bespoke Commercial Aerogel Film Types

Aerogels are high porosity solids containing nanopores resulting in a low density, low thermal conductivity, and high specific surface area material. While silica aerogels are a very popular type of aerogel in aerospace, they perform mechanically as a brittle and fragile material [98, 99], prompting them to be an unlikely candidate for insertion into the interlaminar region of a composite. However, ideal for their high flexibility and high thermal stability [100, 101], PI aerogels can be used as a durable NPN within aerospace-grade CFRP composites. Partnering with Aerogel Technologies, LLC in Boston, Massachusetts, two types of PI aerogel films are manufactured for this study: (i) supercritically-dried (SCD) and (ii) ambiently dried (AD) PI aerogels. These two different types of films can range in thickness from approximately 20 microns to 200 microns, with the general trend of SCD PI aerogel films having greater through-thickness permeability than AD PI aerogel films. A plot depicting the behavior of

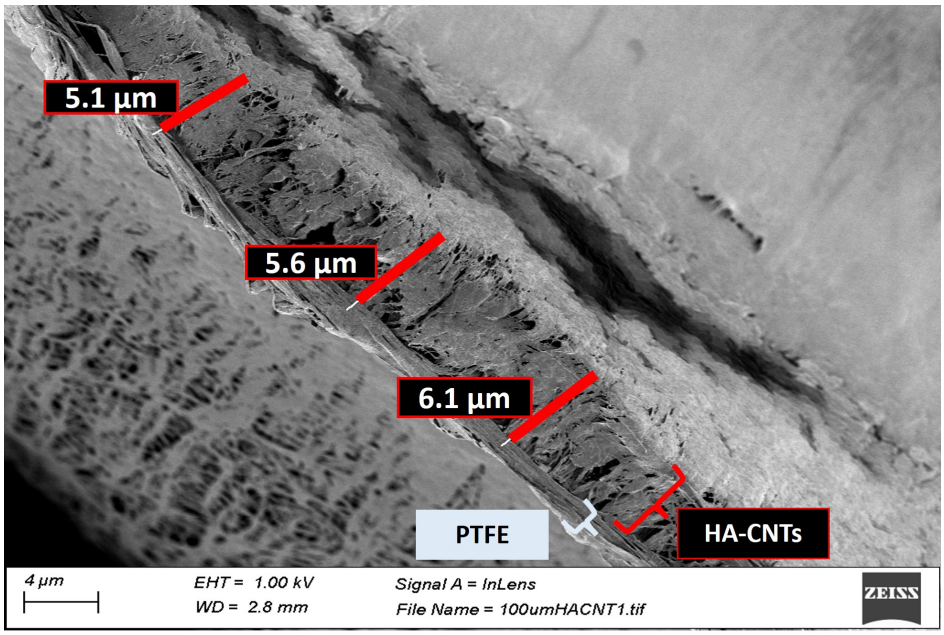


Figure 4.2: SEM depicting the HA-CNT thickness measurements. The red bracket indicates the CNT forest, while the light blue bracket indicates the PTFE film support.

tested PI aerogel films is shown below in Figure 4.3. A SEM image of a SCD PI aerogel film is provided in Figure 4.4.

4.1.3 Other Commercially Available Materials

Along with CNT based materials and PI aerogel films, electrospun polymer nanofiber (EPN) membranes are the remaining NPNs investigated within this thesis for CFRP composite manufacturing. Areal densities of 1.5 gsm and 4.5 gsm of the EPN mats are investigated for their microstructural properties with the material composition consisting of PA 66. The measured thickness for the EPN film of 1.5 gsm is 12 microns and will be referred to as EPN 12 μm. The measured thickness for the EPN film of 4.5 gsm is 21 microns and will be referred to as EPN 21 μm. These membranes, by Revolution Fibers, are manufactured as an interlaminar composite veil to reduce ply delamination, increase flexural strength, increase the composite's fatigue life, and minimize interlaminar fracturing of CFRP [102].

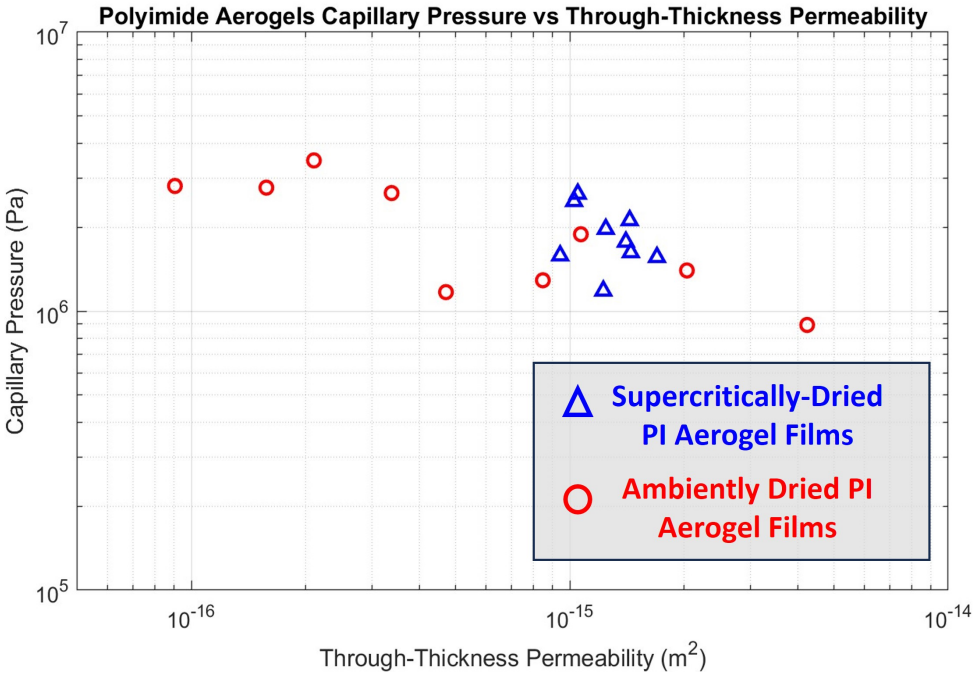


Figure 4.3: Capillary pressure versus through-thickness permeability for a variety of PI aerogels. Red circles indicate AD PI aerogel films, while blue triangles represent SCD PI aerogel films. Regardless of drying type, capillary pressure, thus pore size, is typically consistent between the film types.

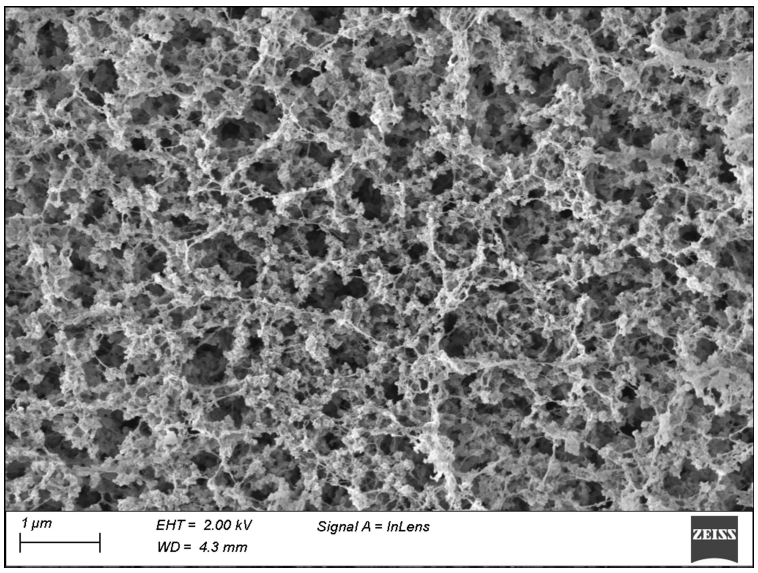


Figure 4.4: Top-View SEM image of a AD PI aerogel film manufactured by Aerogel Technologies, LLC. The nominal thickness of this film has been measured at 61 μm with μCT.

Other investigated materials within this thesis include three other polymer based membranes and one common ceramic nanomaterial. The three main polymers systems are com-

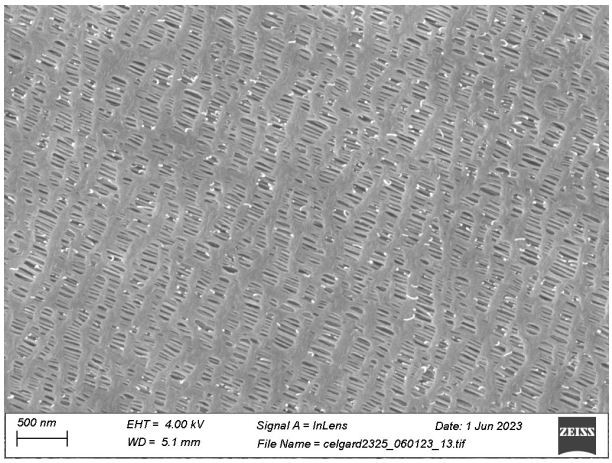
posed of two Celgard membranes and a hydrophilic polyvinylidene fluoride (PVDF) membrane. Celgard 2325 membrane is a trilayer membrane consisting of two outside layers of polypropylene with one inner layer of polyethylene. Developed for its use in high energy lithium battery systems, the selected polymer arrangement provides oxidation resistance, longevity, and high thermal stability [103]. Celgard 2400 membrane is a monolayer membrane of polypropylene used for drug delivery systems [103]. The thicknesses of both Celgard membranes is expected to be approximately 25 μm [103]. A SEM image, top-left of Figure 4.5, of Celgard 2325 is shown below to demonstrate the microstructure and uniformity of the polymer architecture. Hydrophilic PVDF membranes are common in applications of water treatment and recovery through filtration [104]. The manufacturer expected thickness should be within the range of 115 to 223 μm as provided by the material's certificate of analysis. Lastly, the tested ceramic membrane is nanoporous anodic aluminum oxide, known for its highly uniform pore arrangement with a manufacturer expected thickness of 50 μm. These membranes are often used in the synthesis of aligned nanostructures such as nanodots, nanowires, and nanotubes [105, 106].

4.2 Behavior of NPN within Interlaminar Regions

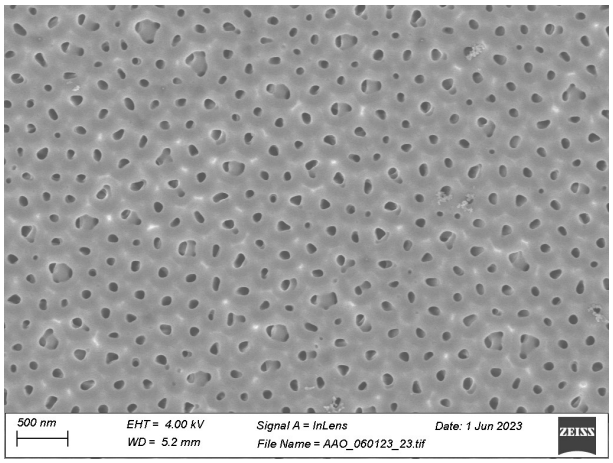
Here, the physical characteristics of NPNs for void removal in VBO-manufactiring of autoclave-grade FRP is reviewed, leading to a focus on NPN capillary pressure and permeability, in section 4.3.

4.2.1 Capillary Pressure for Interlaminar Void Removal

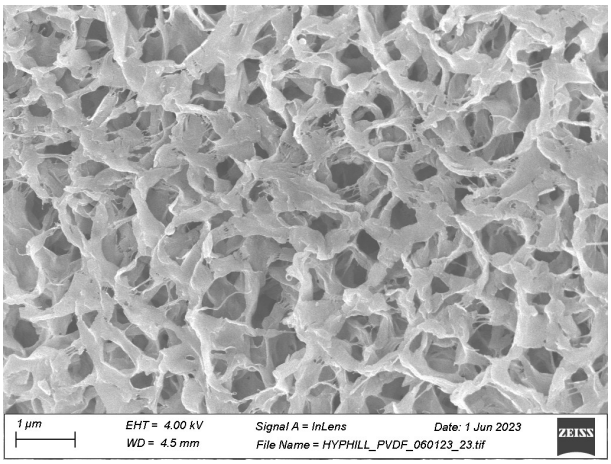
When using autoclaves to manufacture CFRP laminates, external pressure is applied to the entire laminate, reducing existing intralaminar and interlaminar voids within the layered architecture. To replace the pressure requirements supplied by energy-demanding autoclaves, NPNs are placed in the interlaminar region of prepreg FRP composite laminates to remove



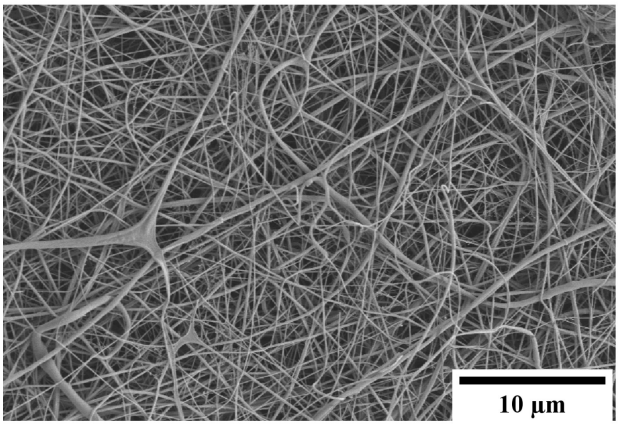
(a) Celgard 2325



(b) AAO



(c) Hydrophilic PVDF



(d) 21 μm polymer NPN

Figure 4.5: Top-view SEM images of other commercial porous materials: (a) Trilayer Polymer Membrane - Celgard 2325; (b) Anodic Aluminum Oxide; (c) Hydrophilic Polyvinylidene Fluoride Membrane; (d) 21 μm polymer NPN.

interlaminar voids. Voids within a laminate are typically produced from entrapped air from incomplete interlaminar surface contact, moisture evaporation from resin, and volatile emission leftover from the prepreg manufacturing process [21, 40, 41]. Within the investigated IM7/8552 composites, three gases are noted within the HexPly 8552 prepreg - acetone, ethanol, and water [107]. The vapor maps of these various volatiles are provided in Figure 4.6.

A large source of interlaminar voids are a product of entrapped air generated during the physical laminate layup process. Once the cure cycle progresses, resin will flow into the pores

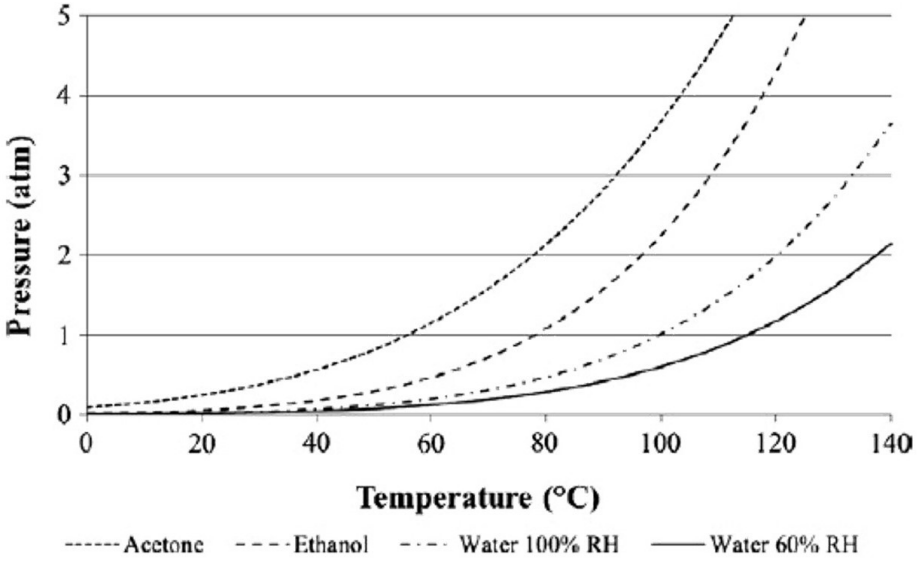


Figure 4.6: Vapor curves of acetone, ethanol, and water - the main volatiles found within HexPly 8552 prepreg. Figure provided by Agius et al. [107].

within the NPNs. At the air and liquid interface within the pores, strong capillary effects are induced due to the pore diameter and non-orthogonal contact angle between the two fluids. This relationship is clearly seen in the Young-Laplace Equation 4.1, written below.

$$P_c = \frac{2\ n\ \sigma}{r_m} \cos(\theta) \tag{4.1}$$

where P_c, n, σ, θ, and r_m are the capillary pressure within the NPN pore, geometric shape factor, surface tension, contact angle between liquid and solid surfaces, and radius of the cylindrical NPN pore, respectively.

Due to the high pore density of the inserted NPN membranes, high localized capillary pressure is supplied throughout the interlaminar region creating contact between the NPN and the surrounding laminae; therefore, reducing the overall interlaminar void content. The resin pressure is assisted by the NPN's capillary pressure to overcome the gas pressure within the NPN, allowing the NPN to be saturated. The resin pressure is a product of the external pressure applied to it, which would include vacuum in vacuum-bag-only (VBO) manufacturing procedures. An illustration of the NPNs intrinsic capillary effects are provided

in Figure 4.7.

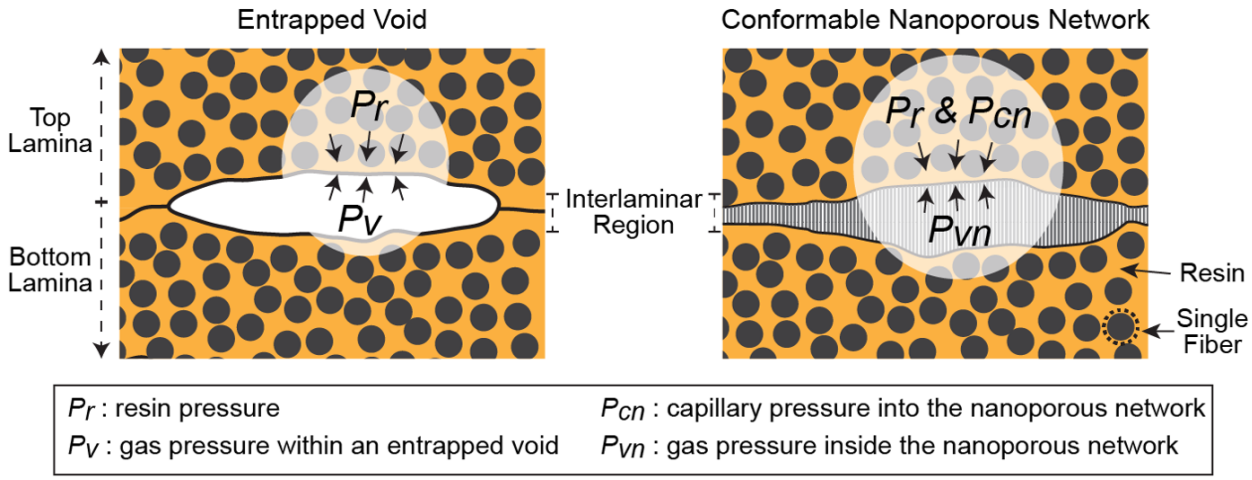


Figure 4.7: A schematic demonstrating the pressure balance within a laminate without NPNs and with inserted NPNs to demonstrate the removal of voids within the interlaminar region. This illustration is depicted with the use of aligned CNTs, but this is applicable for all NPNs. Figure provided by Lee et al. [25].

To provide quantitative values of capillary pressure, capillary flow porometry (CFP) was completed as described in Chapter 2. Utilizing a gas-liquid porometer, the POROLUX™1000 of Professor Gregory Rutledge's (Department of Chemical Engineering) research group of Massachusetts Institute of Technology, the nanoporous networks' microstructures can be investigated [108]. To initiate capillary flow porometry with the POROLUX™1000, samples of 25 mm diameter are extracted from bulk material using a 25mm steel hammer-held hole punch and placed within the POROLUX™1000 circular 25 mm sample holder. A rubber o-ring and screw cap of the sample holder are placed on top of the sample to prevent leakage in connection to the pressure tube. Nitrogen gas, the inert gas used for this test, is supplied to the membrane to achieve the dry curve data collection with an upper pressure limit 2.5 MPa (25 bar). Using perfluoroether, specifically Porefil™, a low viscosity wetting liquid, the wet curve data collection was completed. For materials that are supported with a backing substrate, such as the HA-CNTs, the capillary pressure measured is the membrane with smaller pores, as smaller pore sizes limit flow rate. As a note, the PTFE backing substrates have measured pore sizes of approximately 0.3 μm, which is much larger than the target

material pore size to ensure accurate characterization. The measured data is shown below in Figure 4.9 for a variety of materials. To determine the MFP size, the representative pore size for the tested materials, a factor of 0.715 is applied as the geometric shape factor to account for asymmetric pore geometry [109].

To estimate the capillary pressure measured for VA-CNTs, there are derived fiber bed models that can be used to convert the pressures between VA-CNT and HA-CNT structures. To use this model, CNTs are considered nanofibers. The generalized form, provided by [110], can be described as:

$$P_{c,fiber} = \left(\frac{F}{D_f}\right)\left(\frac{1-\varepsilon}{\varepsilon}\right)\sigma\cos(\theta) \tag{4.2}$$

where $P_{c,fiber}$, F, D_f, ε, and σ, θ are fiber bed capillary pressure, form factor, average fiber diameter, porosity of fiber bed, surface tension of wetting fluid, and contact angle between liquid and solid surfaces, respectively. Form factor is a function of flow direction and fiber alignment. For transverse flow, the form factor is 2, while for longitudinal flow, the form factor is 4; these values are illustrated in Figure 4.8.

4.2.2 Permeability for Void Evacuation

Permeability is defined as the state in which a fluid can pass through a material, with high permeability indicating abundant flow. Defined as a second order tensor and dependent on the directional morphology of the material's pores, permeability is assessed via linear flow [111]. While a material can be porous, this does not guarantee high permeability due to tortuous or potentially closed paths. Additionally, permeability can be anisotropic, similar to stiffness. CNTs are predicted to possess high anisotropy in permeability, with EPNs and PI aerogels having lesser degrees of anisotropy. CFP, the experimental technique used to determine permeability in this thesis, investigates the through-thickness permeability of various nanoporous materials. Permeability is a significant material property to investigate

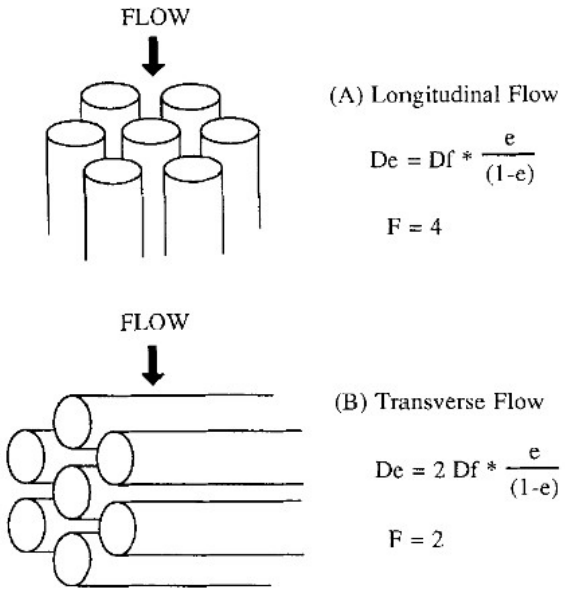


Figure 4.8: Provided form factors for longitudinal and transverse flow of fiber beds used to model flow for VA-CNTs and HA-CNTs. The equations for the equivalent diameter of pores within the fiber network (D_e) is expressed. Provided by Ahn et al. [110].

to further understand the role of NPNs throughout composite cure cycles.

Within the laminae, intralaminar voids have a high likelihood of being connected throughout the fiber axial direction, where there exists higher permeability along the fiber axial direction than the transverse direction [93, 112]. Thus, vacuum, or an added debulking step in the cure cycle, reduces the existence of intralaminar voids that are not explicitly directly targeted through the use of NPNs. However, permeability of the NPNs, along with capillary pressure, plays an important role in the removal of interlaminar voids. As the lamina is compressed under vacuum, with no large temperatures applied to cause significant resin flow, entrapped air from the layup procedure can be evacuated throughout the NPN (mostly in-plane) into the surrounding, breathable layup material. Additionally, moderate permeability of the membrane allows for full saturation, reducing dry regions that can exist within this interlaminar region.

Using the dry curves from the porometer experiments, the through-thickness permeability of the membranes can be extracted from the curves using the fundamentals discussed in

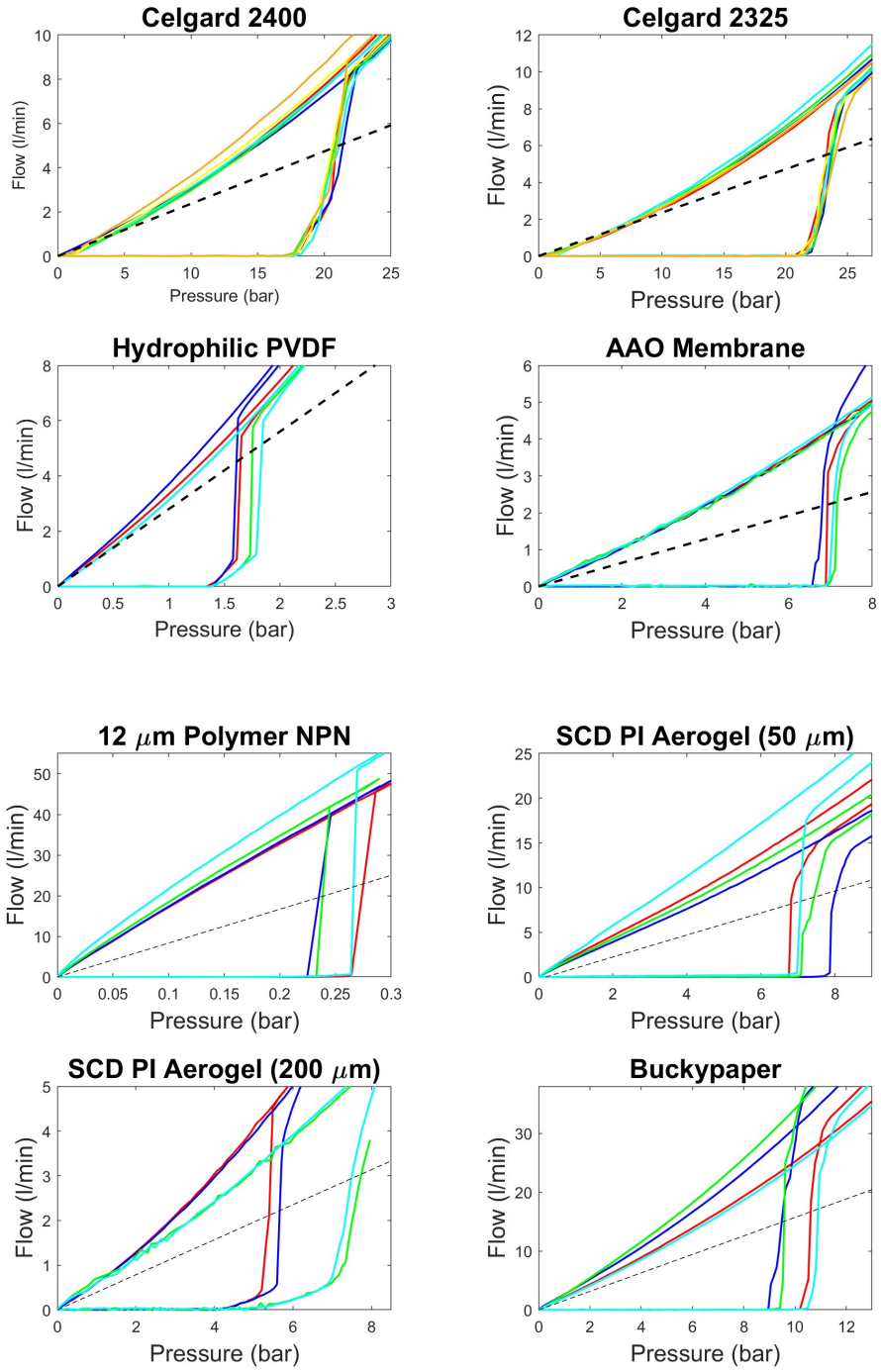


Figure 4.9: Flow versus pressure plots for 8 measured NPNs - 2 Celgard membranes, 2 PI aerogel films, buckypaper, 12 μm polymer NPN, hydrophilic PVDF membrane, and an AAO membrane. Steep slopes of the non-zero flow portion of the wet curve indicate small disparities of the pore size in the membrane. The wet curve aligning with the dry curve signifies full drying of the tested membrane. Different color lines in each plot signify different (repeat) samples.

Section 2.4 (Capillary Flow Porometry) with the note of using measured pressure values near 1 bar for the known dynamic viscosity of nitrogen. For more fragile materials, some PI aerogels and the HA-CNTs, a backing support, respectively hydrophilic PVDF or PTFE film, is used to ensure no material is pushed through the porometer's open valve. The characteristics for these supports is listed in Figure 4.2. For these multi-layered membranes, permeability can be represented by a resistor network, similar to electrical and thermal resistor networks. To model a two-membrane permeability resistor network in series with constant cross-sectional area, the equations 4.3 and 4.4 can be used [113]:

$$\frac{Q_{perm}X_{total}}{tP_{total}A} = \frac{Q_{perm}X_1}{tP_1A} + \frac{Q_{perm}X_2}{tP_2A} \tag{4.3}$$

or simplifying for repeated variables,

$$\frac{X_{total}}{P_{total}} = \frac{X_1}{P_1} + \frac{X_2}{P_2} \tag{4.4}$$

where Q_{perm}, A, t, X_{total}, X_i, P_{total}, P_i are the quantity of permeant, cross-sectional area, time, total thickness, thickness of individual membrane, total, average through-thickness permeability of system, through-thickness permeability of individual membrane, respectively. By testing the assembly of membranes and the support membrane individually, the permeability of the fragile material can be calculated from the series network.

Using the Carman-Kozeny equation, an application of the Hagen-Poiseuille equation and Darcy's Law, the permeability of a porous membrane can be approximated for HA-CNTs or VA-CNTs using the assumption of nanofibers [110, 114, 115]. The equation is as follows:

$$k_{fiber} = \left(\frac{D_f^2}{16K_o}\right)\left(\frac{(1-V_f)^3}{V_f^2}\right) \tag{4.5}$$

where k_{fiber}, D_f, V_f, and K_o are fiber bed permeability, average fiber diameter, fiber volume fraction of fiber bed (V_f = 1 - ϵ), and Kozeny constant, respectively.

This equation can be used for both transverse and axial directions. However, the Kozeny

constant depends on the packing type of the fibers, volume fraction, pore non-uniformity, and tortuosity of fluid flow paths. Due to the difficulty of determining this constant, a deeper literature review would be required after this thesis to convert the permeability results of the HA-CNTs to an equivalent VA-CNT forest permeability.

4.2.3 Secondary Characteristics of NPN for Resin Cannibalization and Interlaminar Region Thickness

Along with the fundamental characteristics of permeability and capillary pressure that allow for void evacuation, void reduction, and resin saturation, there are secondary characteristics that enable lower void content within the cured laminate. One secondary characteristic that is inherent within the property of permeability is thickness. From past manufacturing work, it has been discovered that thinner NPNs have more success with unidirectional FRP laminates and thicker NPNs are more successful with woven FRP laminates. Thicker NPNs provide contact between woven laminae in the interlaminar region where there is more disparity, versus unidirectional laminates that are more consistent in interlaminar spacing. There is also a subjective balance between thin NPN and thick NPN performance within the interlaminar region. NPNs that are too thin become saturated too quickly and do not provide an outlet for entrapped air to escape the laminate during the cure cycle. NPNs that are too thick cannibalize the resin throughout the laminate, leaving the laminate more likely to have intralaminar voids.

Hinted at in the previous paragraph, conformability is another essential secondary characteristic that enables persistent contact between the NPN and the surrounding laminae. In order for the localized capillary pressure to be produced at the interface of the NPN and lamina, the two surfaces need to be in contact or close enough for the surface tension of the lamina's resin to pull the surfaces into contact with each other. This is more difficult for woven FRP composites due to the interweave regions that are prone to voids compared to unidirectional FRP composites. Lastly, compressibility is an important trait within an

NPN to mitigate against a significant interlaminar region thickness increase. If the NPN can be compressed during the cure cycle as vacuum is applied to the laminate, the interlaminar region thickness can be minimized as much as possible, reducing potential negative effects on the fracture performance of these CFRP laminates.

4.3 Experimental Values of NPNs

Described in more detail above, here is a concise, summary table, Table 4.2, providing the characteristics of the relevant nanoporous materials, including thickness, MFP capillary pressure, MFP size, and evaluated through-thickness permeability.

4.4 Ashby Guideline for Nanoporous Materials

Using Table 4.2, and other porometry tests, the MFP capillary pressures and through-thickness permeabilities are plotted for a range of materials. The Ashby plot in Figure 4.10 shows all of the NPN materials, along with the nanoporous materials used as engineering reference materials throughout this thesis. These properties are for the wetting liquid used in the porometry experiments, Porefil™. The Ashby plot in Figure 4.11 shows the characteristics of three NPN material families that are inserted into aerospace-grade CFRP composites. Note, these properties, capillary pressure and permeability, are plotted for NPNs wetted with 8552 resin instead of Porefil™, as this is the investigated epoxy system within this thesis. Shown by both plots, Figure 4.10 and Figure 4.11, most materials tend to fall between two categories: (1) high permeability and low capillary pressure and (2) low permeability and high capillary pressure. Using the Young-Laplace equation (Equation 4.1) and Darcy's Law (Equation 2.2), it is direct to see why this relationship naturally occurs.

Table 4.2: Microstructural characterization summary of the investigated NPN material families used for CFRP composites and other NPN sized materials, along with reference to the manufacturer. MFP Pore Size includes a factor of 0.715 to account for asymmetric pore geometry.

Nanoporous Materials	Thickness (μm)	MFP Capillary Pressure (MPa)	MFP Pore Size (nm)	Through-Thickness Permeability (μm^2)	Material Category in Figure 4.10
Celgard 2325	29.1	2.34	19.5	7.69E-05	Celgard
Celgard 2400	27.8	2.07	22	8.76E-05	Celgard
Aerogel SCD 50 µm	59	0.73	64	1.41E-03	SCD Aerogel
Aerogel SCD 60 µm	69	1.02	45.4	1.03E-03	SCD Aerogel
Aerogel SCD 200 µm	151	0.65	72.6	9.43E-04	SCD Aerogel
AAO 120 nm	52	0.70	67.2	2.77E-04	AAO
Hydrophilic PVDF	128	0.17	277.3	4.21E-03	Hydrophilic PVDF
EPN 12 μm	12	0.025	1823.4	2.31E-02	EPN Films
EPN 21 μm	21	0.049	970.4	2.07E-02	EPN Films
CNT Buckypaper (7 gsm)	21.8	1.01	46.5	5.09E-04	CNT Based Materials
HA-CNT (100 µm Grown)	6.79	1.25	37.4	2.41E-04	CNT Based Materials
Aerogel SCD 10 µm	26	0.64	102.1	1.70E-03	SCD Aerogel
Aerogel AD 70 µm	74.7	1.23	38.1	9.19E-04	AD Aerogel
Aerogel AD 40 µm	41.2	0.78	60.29	1.07E-04	AD Aerogel
PTFE Backing Support	30.7	0.15	319	1.35E-03	N/A

4.5 Summary

Throughout this chapter, the fundamental behavior of NPNs are discussed and characterized via CFP, μCT, SEM, and various equations. Capillary pressure and permeability are shown as two primary qualities that should be investigated to support NPN insertion into the interlaminar region, while secondary characteristics such as conformability, compressibility, and thickness should also be considered. Quantitative results were provided for a variety of nanoporous materials for capillary pressure, through-thickness permeability, MFP pore size, and thickness. Preliminary Ashby charts were provided with materials existing within two

classifications: (1) high permeability and low capillary pressure and (2) low permeability and high capillary pressure. Using the framework provided within this chapter, NPNs can be integrated within structural CFRP laminates to investigate their void removal performance and validate the current fundamental background.

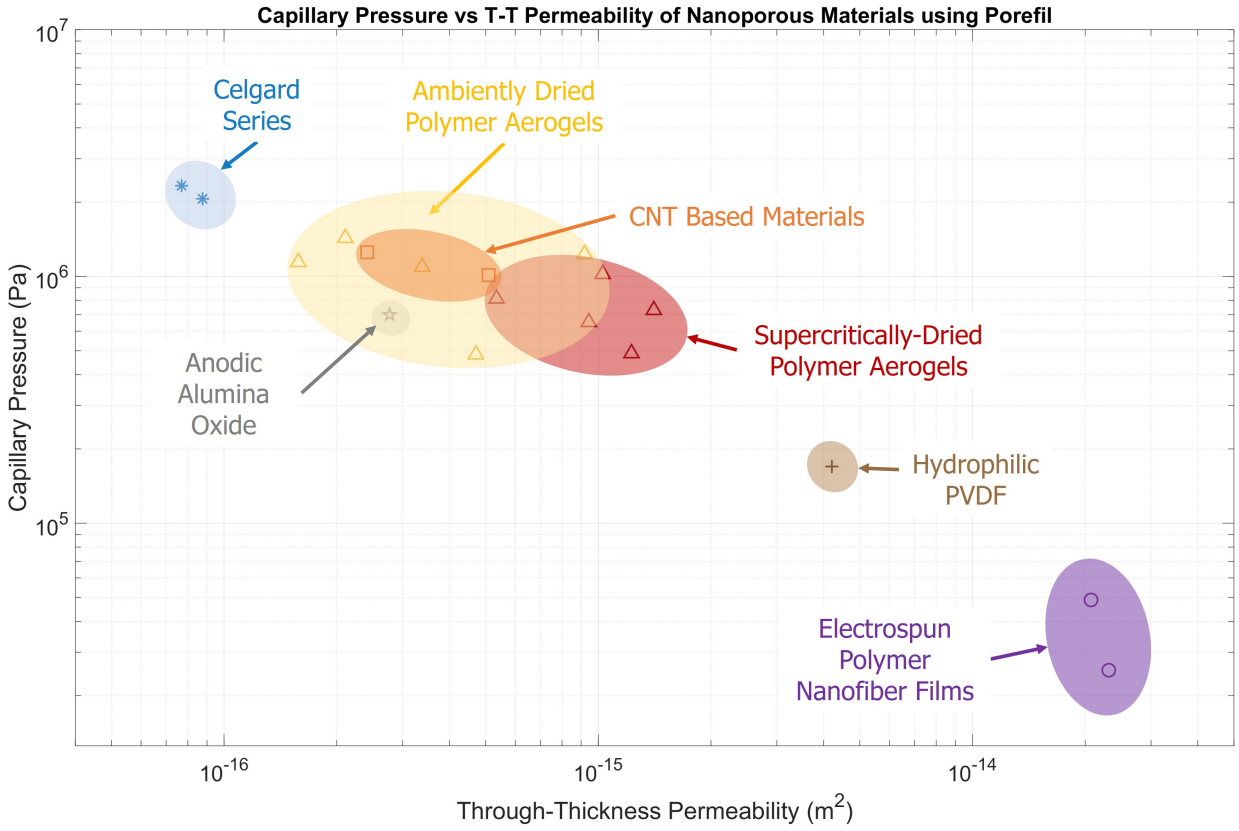


Figure 4.10: Capillary pressure versus through-thickness permeability for nanoporous materials using wetting liquid, Porefil™, as the fluid source. All data points were tested at least three times with the plotted point being the average of the results within this Ashby plot. The general trend of an inverse relationship between capillary pressure and permeability is shown clearly here.

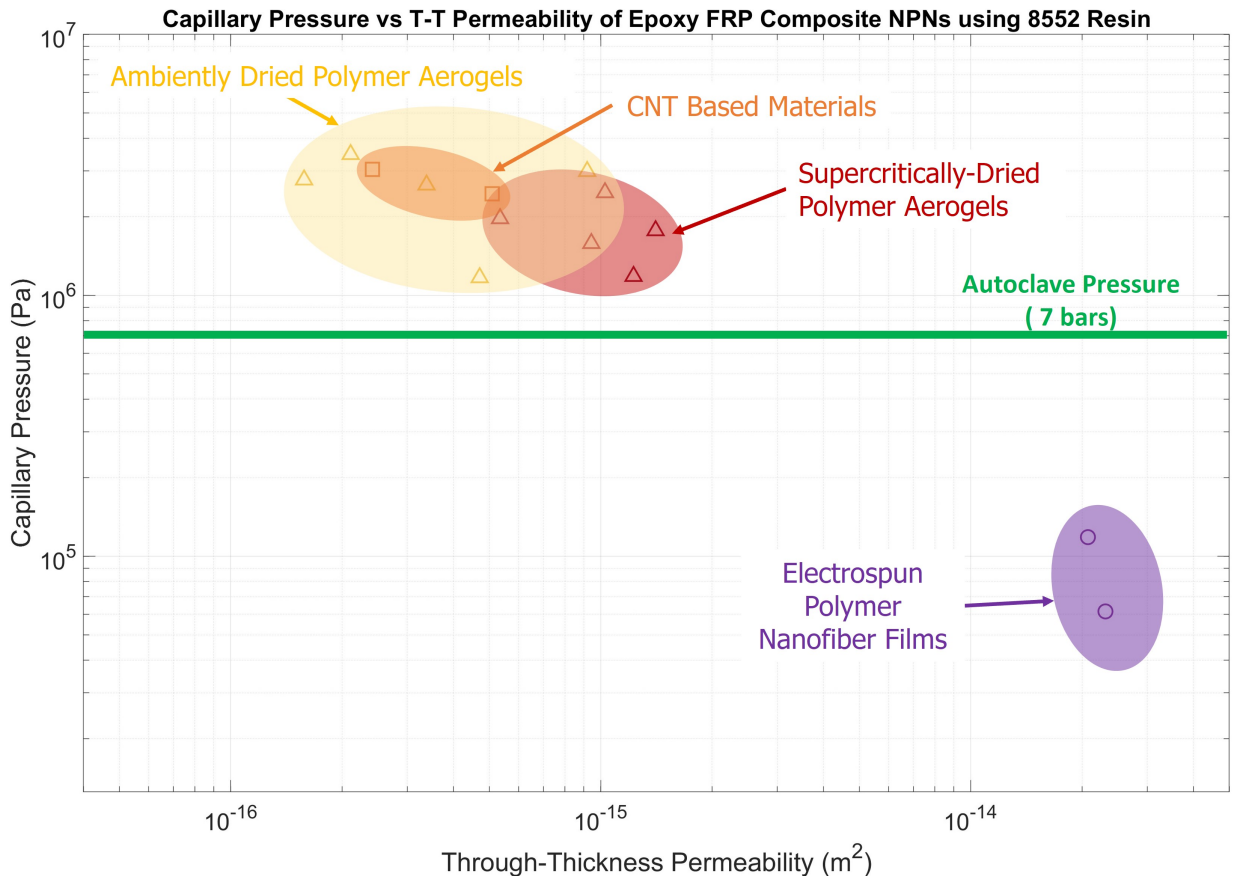


Figure 4.11: Capillary pressure versus through-thickness permeability for the three NPN material families used in FRP composites using HexPly ® 8552 resin as the fluid source. All data points were tested at least three times with the plotted point being the average of the results within this Ashby plot. The bold green line represents the 7 bar pressure typically supplied by an autoclave for epoxy-based CFRP aerospace-grade composite laminates.

Chapter 5

In Situ Visualization of CFRP Laminate Curing with and without Nanoporous Networks

Developing in situ experiments with the assistance of computed tomography, whether microcomputed tomography (μCT) or sychrontron radiation computed tomography (SRCT), has allowed invaluable insight into the evolution of composite features via designed manufacturing processes or sub-second damage progression [82, 85, 116, 117]. Within this thesis chapter, two designed in situ μCT experiments are developed for two discrete functions: (1) to observe the resin flow throughout nanoporous networks (NPN) integrated within a laminate and (2) to investigate the void evolution of IM7/8552 woven composites under temperature and vacuum conditions. The work in this chapter was a collaboration with Dr. Jingyao Dai, Postdoc in necstlab, a research group at MIT.

5.1 Development of In Situ Resin Flow Monitoring and 3D Void Observation Devices

To illustrate the resin flow front, a model was developed [27, 93] to explain the infiltration of resin into the NPNs as a function of time. Through Darcy's Law, a one dimensional wetting model for NPNs was formulated, shown in Equation 5.1, where the reservoir of fluid originates from a prepreg lamina. The Equation 5.1 represents the flow front speed of the resin as it moves throughout the NPN. With this model, an infusion time can be calculated for each NPN based on capillary pressure, permeability, and porosity for generic composite systems and their cure cycles, while including the effects of vacuum pressure. Various flow front gas pressures can be modeled to represent the interlaminar entrapped gases or inadequate vacuum. A plot of HexPly ® 8552 resin's viscosity, Figure 5.1, is provided to demonstrate the change in viscosity as a function of temperature. The flow front model is as follows:

$$\left(\frac{dh_f}{dt}\right) = \left(\frac{k}{\varepsilon\mu(T)}\right)\left(\frac{P_{atm} - \nabla p + P_c}{h_f}\right) \tag{5.1}$$

where h_f, t, k, $\mu(T)$, ε, P_{atm}, ∇p, P_c, and T represents flow front position, time, through-thickness permeability, dynamic viscosity (as a function of temperature), porosity, atmospheric pressure, gas pressure at flow front, capillary pressure, and temperature respectively.

However, experimental results are needed to validate this model due to the assumption of using a 1D model with multi-directional porous materials. Newtonian fluid flow is utilized for these models due to the low shear rate of the resin flow [119, 120]. As a result, two in situ experiments were created to monitor the resin infusion as a function of temperature and time, along with revealing the void evolution behavior that a CFRP laminate experiences throughout a cure cycle.

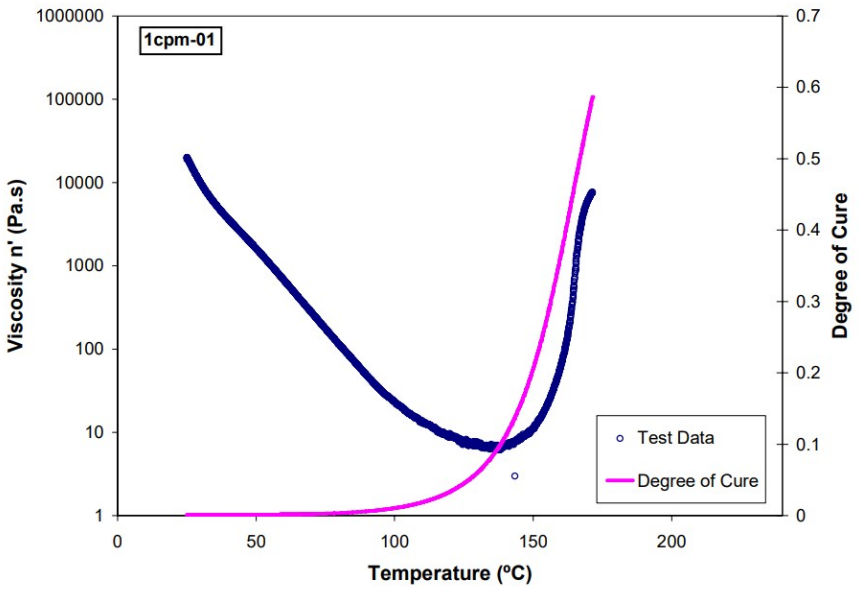


Figure 5.1: Viscosity and degree of cure calculated for a 1°C/min of HexPly 8552 resin. Figure provided by Van Ee et al. [118].

2D μCT Newtonian Resin Flow Front Monitoring Experiment

The first experiment focused on monitoring the resin flow front through NPNs using close-to real-time ($\sim$ 4 seconds sampling) 2D projections. Throughout the scan, the saturation, compliance, and compressibility of the selected NPN, a SCD PI aerogel film, is observed as a function of temperature. In this experiment, a laminate can have temperature applied to the top and/or bottom surface of the laminate to visualize the resin flow front moving through the NPN from surrounding laminae. In the initial tests, only the bottom surface of a laminate was heated via one Peltier module to investigate the experiment's feasibility. A visualization of the experimental set-up is shown in Figure 5.2. The thermal-mechanical assembly consists of two Peltier modules, a central processing unit (CPU) cooler, an uncured carbon fiber reinforced polymer (CFRP) AS4/8552 unidirectional laminate with aerogel NPN, and a compression system. Overall, this experiment is completed in approximately 30 minutes with a projection sampling rate of approximately 4 seconds.

By placing a Peltier module, rated for 8.6 volts and 8.5 amps, on both surfaces of the

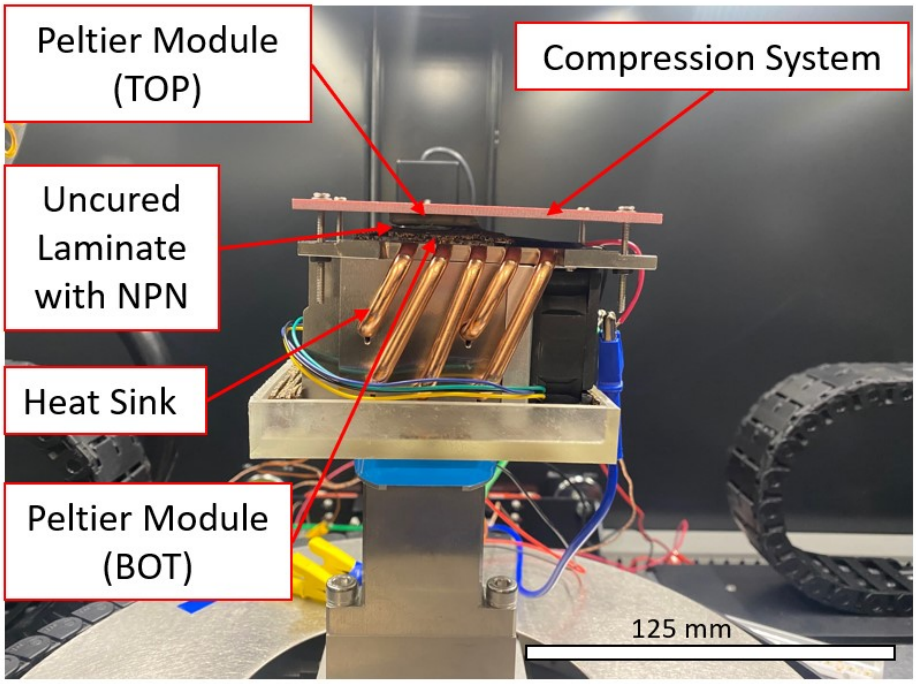


Figure 5.2: Physical set-up of the 2D Newtonian resin flow monitoring thermal-mechanical system. The system is directly attached to the rotating scanning stage of the μCT (Zeiss Xradia 620 X-ray microscope) chamber through a connector printed via stereolithography. Note this set-up was abandoned after initial testing.

laminate, a thermal gradient can be established throughout the laminate with one Peltier module, attached to a CPU cooler (Dynatron T17), capable of supplying low temperatures if desired. The CPU cooler is an aluminum heat sink with embedded copper heat pipes that is supplied 11.5 V from a DC power supply. By establishing a thermal gradient, flow front speeds can be investigated for different layers of NPN throughout the laminate. The compression system ensures that the all system components stay in full contact with each other as the stage moves during the μCT scan, as movement is required to capture the necessary reference images. Compression is completed through the use of hand tightened nuts and bolts between a red glass fiber reinforced polymer (GFRP) composite panel and heat sink. To power one Peltier module, a Proportional – Integral – Derivative (PID) controller, Omega CN32PT-440-DC, is used in conjunction with a solid state relay, Crydom Solid State Relay D1D12, to effectively control the supplied temperature provided by the module to

the CFRP laminate. The other Peltier module was supplied power directly by a DC power supply.

However, after completing an initial trial, the CPU cooler was determined to be too large in width, causing large distances from the X-ray source. Thus, reducing the intensity and resulting in a pixel size of over 1 μm, approximately 1.3 μm. To reduce the positional effects of the heat sink, a new, reduced width set-up was developed for reduced pixel size to achieve better projection quality. This experimental set-up is provided in Figure 5.3. Similar to the previous set-up, a compression system is used to hold the laminate and surrounding materials to avoid movement during the scan and ensure full laminate contact with the Peltier module. The insulation is used to prevent strong thermal differences across the sample holder into the μCT stage, while the vacuum bag is used to catch any resin bleeding due to the applied temperature.

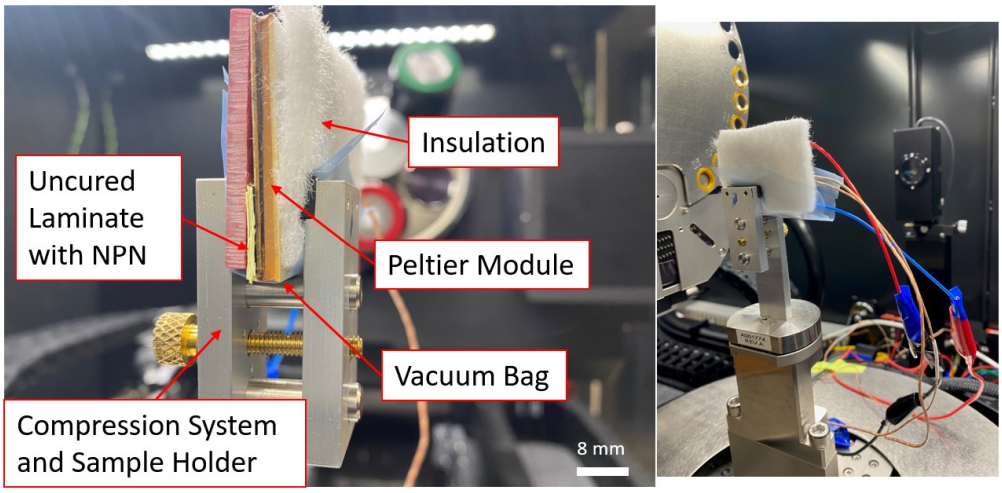


Figure 5.3: Physical set-up of the updated 2D Newtonian resin flow monitoring thermal-mechanical system. The previously-used CPU cooler and compression system (see Figure 5.2) has been discarded. The system is directly attached to the rotating scanning stage of the μCT (Zeiss Xradia 620 X-ray microscope) chamber via a Zeiss supplied sample holder. The extended wires shown in the right figure are connected to the Peltier module with two attached thermocouples for redundancy.

3D μCT Observational Void Evolution Multi-Step Experiment

When initially manufacturing the woven IM7/8552 composites and performing μCT to check for void quantity, voids would consistently appear throughout the laminate, regardless of the integrated NPN or its application into the laminate. This was a vastly different experience from the manufacturing of 8552-based unidirectional composite systems. To understand why these voids were present, a 3D volumetric X-ray μCT experiment was designed to understand the evolution of voids throughout a cure cycle, along with the the role of NPNs in void reduction in the interlaminar region. In this experiment, a laminate was chilled at low temperatures to prevent resin movement and then heated quickly to a given temperature for a given period of time. Once the heating hold was completed, the laminate was quickly re-chilled to low temperatures to prevent any additional heating and prevent further resin movement. The laminate remained frozen throughout the scan and until the next heating stage. This process was repeated multiple times in the designed experiment resulting in a multi-step μCT experiment. Figure 5.4 shows the physical configuration of the experiment.

Resembling the 2D projection experimental set-up, one Peltier module, rated for 8.6 volts and 8.5 amps, is located on top of a CPU cooler to control the applied temperature to the CFRP laminate. This singular Peltier module can chill (or heat by reversing the polarity of the Peltier module) the laminate directly. The Peltier module of this assembly is powered similarly to the 2D in situ experiment using a PID controller and solid state relay, while the active heat sink was powered directly through the use of a DC power supply. In contrast to the 2D in situ experiment, a vacuum-bag-only (VBO) manufacturing methodology is utilized through the use of a vacuum port, vacuum bag, tool plate (the aluminum T-bar), caul plate, breather, and resin cork dams. The VBO-manufacturing approach of this experiment allows an understanding of the NPN's role in a more representative environment. One K-type surface thermocouple is placed on the back side of the aluminum T-bar within the breather to record the temperature being applied to one surface of the laminate. Additionally, the aluminum T-bar was milled to allow for higher X-ray transmission during the scan, allowing

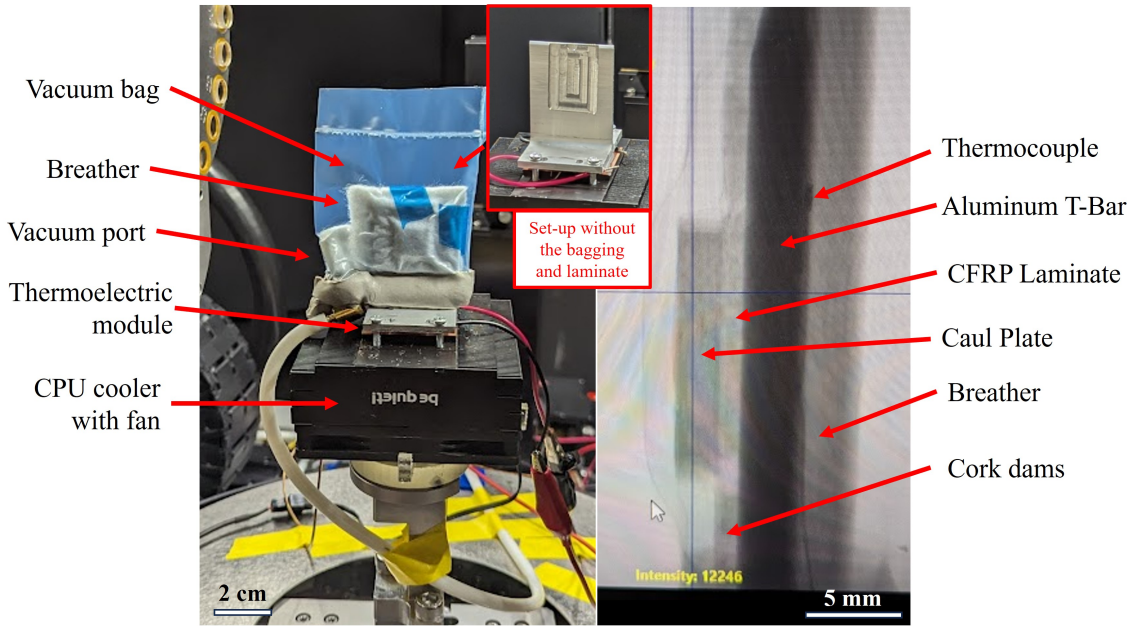


Figure 5.4: 3D Observational Void Experiment: Left: Physical set-up of the 3D laminate void evolution monitoring thermal-mechanical system. The system is directly attached to the rotating scanning stage of the μCT (Zeiss Xradia 620 X-ray microscope) chamber through a connector printed via stereolithography. Inset shows the laminate mounting assembly without the vacuum-bag-only configuration. Right: A screenshot of a captured projection displaying the laminate components showing their position during the scan set-up.

better projection quality of the sample. These scans typically take between 18 through 22 hours to complete due to the high exposure time needed for image quality, thus necessitating the use of a Peltier module to freeze the laminate after temperature excursions.

5.2 Initial *μCT* In Situ 2D Newtonian Resin Flow Monitoring Results of AS4/8552 Composites

For the 2D μCT in situ experiment, an 8-ply AS4/8552 unidirectional CFRP laminate with SCD PI aerogel NPN was utilized. The SCD aerogel is measured to be 151 microns in thickness and labelled as Aerogel PI 200 µm. Material properties of this aerogel film can be found in Table 4.2. Three K-type thermocouples were placed throughout this laminate, one on each side of the laminate to monitor the applied temperature and one in the center

between the fourth NPN and fifth ply in the laminate. A schematic demonstrating this layout is provided for clarity in Figure 5.5.

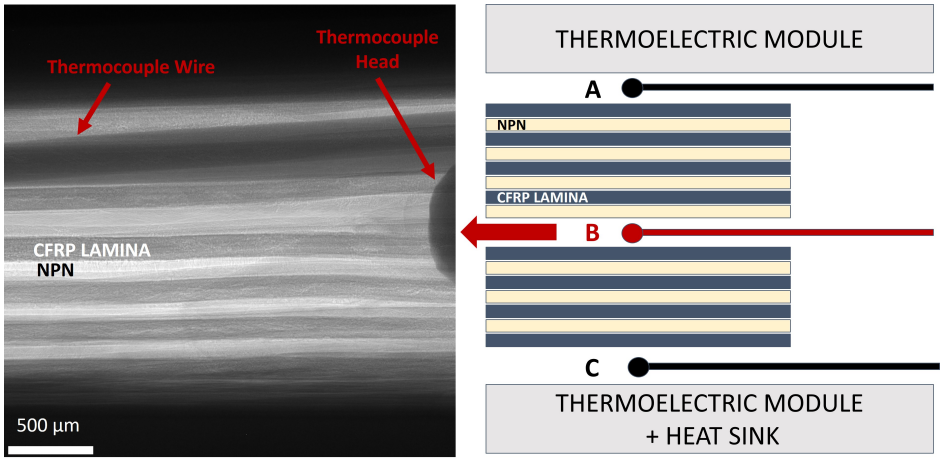


Figure 5.5: Projection of 2D Newtonian Resin Flow Front Experiment with the Associated Configuration Schematic: Left: Captured projection demonstrating the configuration of the NPNs and surrounding laminae. The circle on the far right corner and the horizontal line shown towards the top of the laminate are the thermocouple head and its attached wire. Right: Schematic of the laminate with integrated NPN, the supporting thermocouples (labelled A, B, and C), and two attached thermal module assemblies. The gray rectangles in the schematic represent laminae and the yellow squares represent aerogel thin films.

This scan was completed in the longitudinal direction of the AS4 fibers and heat was only applied to one side of the laminate for this preliminary test. The pixel size for this scan was 1.32 microns with a voltage of 160 kV used. No filter was applied to this scan. The number of projections chosen was 351 with an exposure of 2 seconds to ensure quick imaging and sufficient projection quality. The projection sampling rate was approximately 4 seconds, while the temperature sampling rate was approximately a second. The scan mode was selected such that the sample holder did not rotate during the scan and only gathered projections at 0 degrees. However, the sample stage moved vertically to capture reference images frequently.

The laminate was heated by directly supplying voltage and current from the DC power supply to the bottom Peltier module. As a note, there is an attached PID controller to the top Peltier module and an additional bottom Peltier module, but for this trial the PID

controller connection was interrupted; thus, power was directly supplied by the DC power supply to the bottom Peltier module for heating. Initially, the Peltier module was supplied 3 V, but was then reduced to 2 V to decrease the heating ramp rate. The resulting temperature profile, recorded by the middle thermocouple (B) demonstrated by Figure 5.5, is provided in Figure 5.6. While this heating is occurring, projections are captured approximately every 4 seconds.

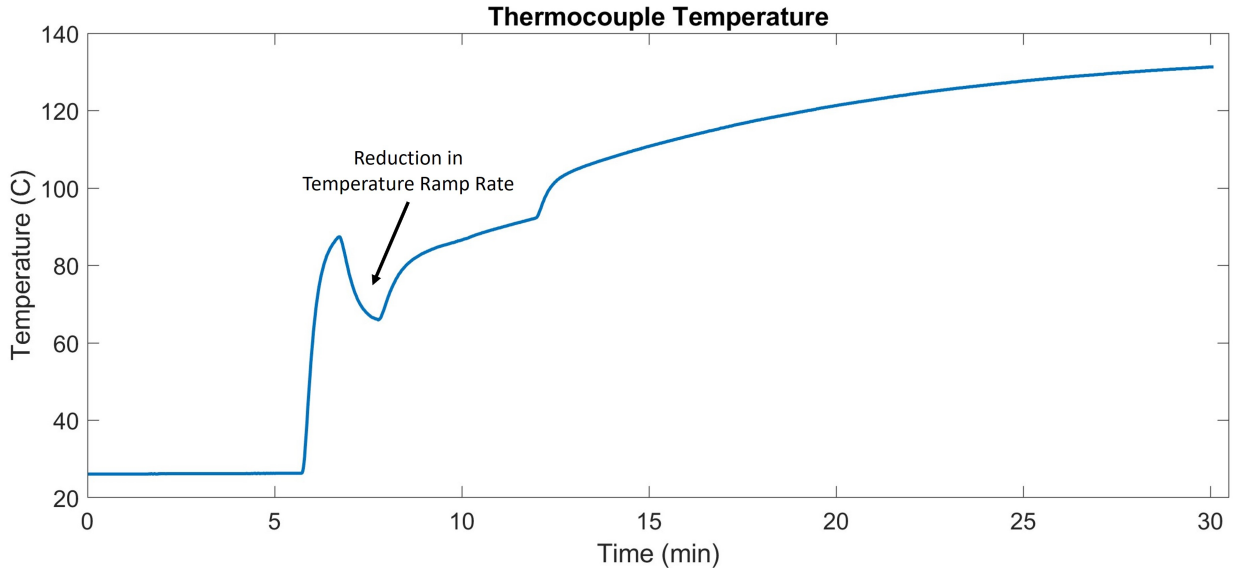


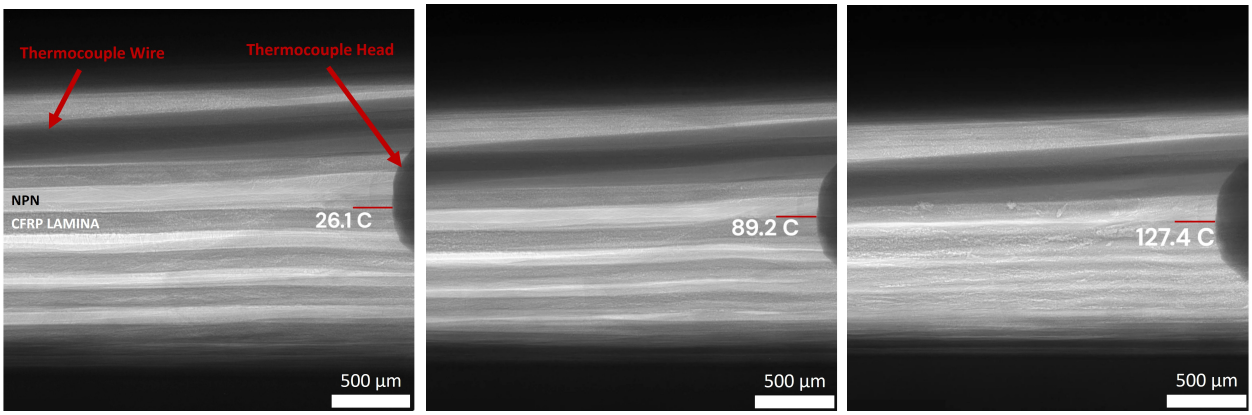
Figure 5.6: Temperature plot showing the laminate thermocouple (labelled B in Figure 5.5) temperature during the initial captured projections. The reduced temperature ramp rate before the 10 minute mark is a result of altered DC power supply input to reduce the heating ramp rate. The temperature ramp rate was adjusted to decelerate the flow front speed due to the pre-determined projection sampling rate of 4 seconds.

Throughout the scan, the experiment demonstrated the wetting of aerogel as the temperature increased, dry regions in the intralaminar regions forming, and the compressibility of the aerogel film. At approximately 89 °C, using the middle thermocouple recorded temperature, noticeable compressibility of the aerogel films occurred. The closest aerogel layer underneath the laminate inserted thermocouple reduced to 30 % of its original thickness. Additionally, dry regions formed in the laminae of the composite due to resin cannibalization, as a result of thick NPNs. Selected projections, along with their temperatures are shown in Figure 5.7.

While initial insights into resin cannibalization and aerogel compressibility were confirmed by the captured projections, the resin flow front advance was unable to be determined through the NPN at the current scan pixel size. The updated set-up, shown in Figure 5.3, was used to determine the minimum pixel size to capture the resin flow front. When moving the updated 2D in situ setup to the closest position to the source, to avoid collision, the pixel size ranged from 0.3 to 0.4 microns, resulting in a resolution near 1 micron. However, the significantly low intensity of these projections caused poor image quality due to the necessary position of the detector to achieve the desired pixel size. To mitigate this consequence of a finer resolution, exposure time is increased; thus, increasing the sampling time rate for captured projections. This increase in exposure time would cause time-distant data collection, not suitable for viewing the flow front of membranes of 200 microns or less. As a consequence, this experiment would need different imaging equipment, such as a nano-computed tomography X-ray microscope or would strongly benefit from synchrotron imaging.

5.3 3D Multi-Step μCT In Situ Void Observation Results of Woven IM7/8552 Composites

For the multi-step μCT experiments, a 5-ply ($[0]_5$) woven IM7/8552 composite is fabricated to fit within the vacuum assembly that is placed upon the PID-controlled Peltier Module for regulated heating and cooling. The dimensions of the flat-panel IM7/8552 laminate are 12.7 mm (0.5 inch) by 12.7 mm (0.5 inch) to fit on the aluminum T-bar that is approximately 25.4 mm (1 inch) in width. The pixel size for these scans range between 1.6 to 1.7 microns. 24 W power and 160 kV voltage were used with a HE2 filter for improved X-ray transmittance. An exposure time of 15-22 seconds was applied for these scans to get acceptable intensities for better image quality. Dissimilar to the 2D experiment, a scanning fan of -110 to 110 degrees was used for the scan to reconstruct 2D cross-sectional images. Within this investigation, both heating and cooling are required to determine the void evolution. To switch between



(a) Projection showing the initial configuration of the PI aerogel NPN and AS4/8552 unidirectional prepreg near room temperature. Aerogel and laminae layers are different shades due to the different densities. All layers, both CFRP laminae and aerogel NPN, are initially comparable in size.

(b) Projection showing the PI aerogel NPN and AS4/8552 unidirectional prepreg around 89 °C. Some aerogel NPNs were wetted via 8552 resin flow with films decreasing in thickness. The wetting of the aerogels is most apparent at films towards the bottom of the laminate, near the heat source.

(c) Projection showing the PI aerogel NPN and AS4/8552 unidirectional prepreg around 127 °C. Most aerogel NPNs were wetted via 8552 resin flow with films decreasing in thickness. Shown by the speckled regions throughout the laminae, dry regions exist in the intralaminar regions.

Figure 5.7: Initial results of the 2D Newtonian flow monitoring experiment with a 8-ply ($[0]_8$) AS4/8552 unidirectional-ply CFRP laminate. The temperature is that of the thermocouple placed in the middle of the laminate. The short and red horizontal line near the temperature label is the interface between the NPN and CFRP lamina where the thermocouple is placed.

the thermal modes, the polarity of the thermoelectric module is reversed.

Four time steps were investigated for three laminates within this section. The three laminates are: (1) $[0]_5$ IM7/8552 woven laminate with no applied NPN, (2) $[0]_5$ IM7/8552 woven laminate with PI aerogel NPN, and (3) Laminae-only heat treated $[0]_5$ IM7/8552 woven laminate with PI aerogel NPN. The following list describes the steps and an example thermal profile for the first two scans (of Step 0 and Step 1) are shown in Figure 5.8:

Step 0 : After vacuum bagging. The laminate has been cooled to around approximately 0 °C with no supplied heat applied to the laminate. The laminate is under vacuum.

Step 1 : After a 5 minute ramp to 60 °C, there is a 15 minute hold at 60 °C. The laminate is under vacuum. Once heated to the desired conditions, the laminate's temperature is reduced to approximately 0 °C and held until the next step.

Step 2 : After another 5 minute ramp to 60 °C, there is a 15 minute hold at 60 °C. The cumulative time at 60 °C is 30 minutes. The laminate is under vacuum. Once heated to the desired conditions, the laminate's temperature is reduced to approximately 0 °C and held until the next step.

Step 3 : After another 5 minute ramp to 60 °C, there is a 15 minute hold at 60 °C. The cumulative time at 60 °C is 45 minutes. The laminate is under vacuum. Once heated to the desired conditions, the laminate's temperature is reduced to approximately 0 °C.

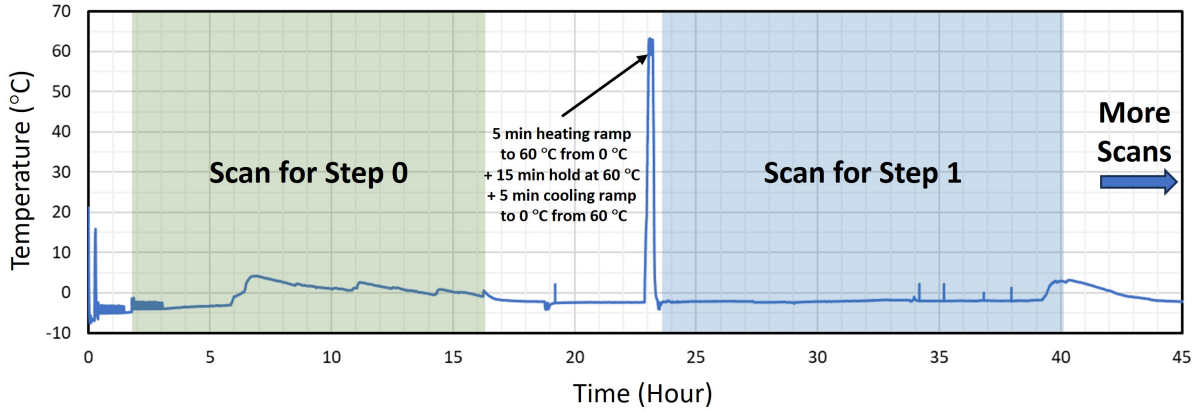


Figure 5.8: Temperature plot showing the applied temperature to the laminate versus time for the 3D multi-step μCT experiment (for Step 0 and Step 1 only). The laminate for this plot is the $[0]_5$ IM7/8552 woven laminate with PI aerogel NPN (no laminae desolventing). The long scan times are illustrated within this figure.

An image, Figure 5.9, of a reconstruction slice from the second experiment is provided to demonstrate the arrangement of components imaged within these scans. At the top of the reconstructed image is the glass fiber reinforced polymer caul plate wrapped in guaranteed non-porous Teflon (GNPT) film. Underneath the wrapped caul plate is the manufactured laminate with the dark horizontal strips indicating the unsaturated PI aerogel NPN. The spotted layer beneath the laminate is the applied peel ply and the light gray region at the bottom is the aluminum T-bar.

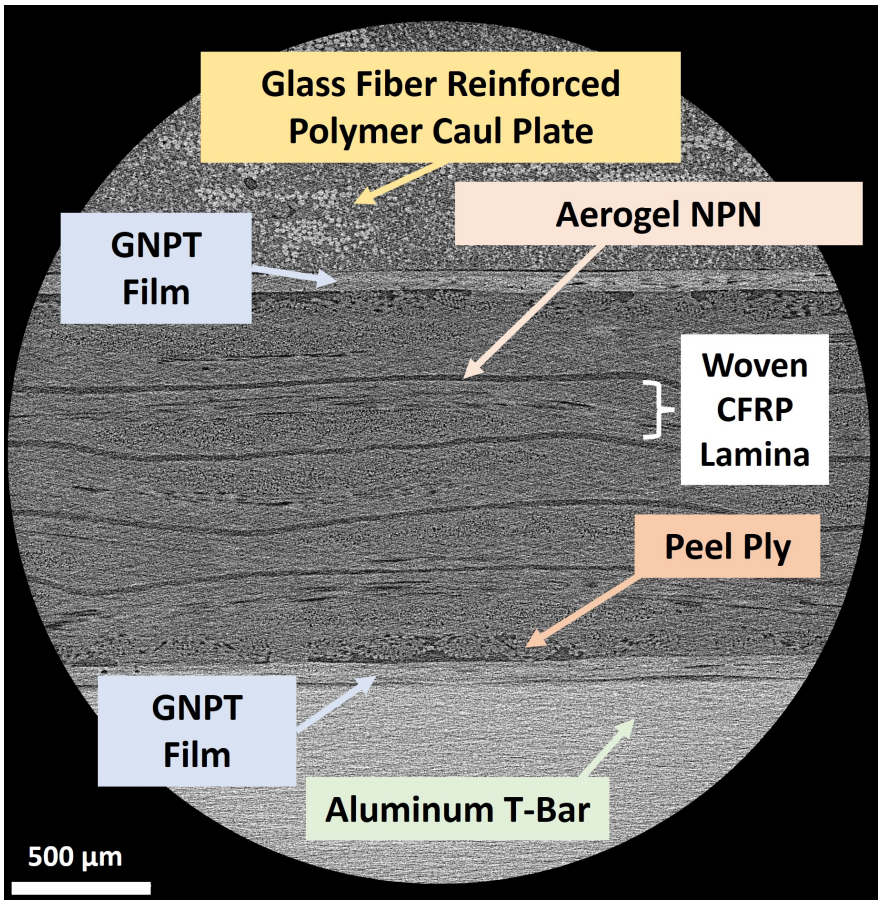


Figure 5.9: CFRP woven laminate cross-section and surrounding components during the 3D μCT in situ multi-step experiment. The main components are the laminate, GNPT-wrapped caul plate, attached peel ply, and aluminum T-bar. This reconstructed image is provided from Step 0 of the second multi-step μCT experiment for the laminate with applied aerogel NPN (without desolventing). There exists voids within the intralaminar regions in this image.

The first of three experiments completed with the multi-step μCT system was with a $[0]_5$ woven IM7/8552 laminate with no applied NPN. Voids of entrapped gas existed near the interlaminar regions with larger voids appearing throughout the intralaminar regions of the laminate. As the first heating step is applied to the laminate, new voids formed and existing voids expanded in size. After the second heating step, a total of 30 minutes at 60 °C, voids continued to expand in size. At the final step of this experiment, nearby voids coalesced and isolated voids maintained expansion. The expansion of these voids occurred within the intralaminar, resin-rich regions of the composite indicating the thermally-affected

resin as the source of expansion. From Figure 4.6, acetone, ethanol, and water are the main sources of volatiles when testing HexPly 8552 prepreg. By heating the laminate to 60 °C for an extended period of time, the residual solvent gained a non-negligible partial pressure, where increased time allowed for further growth. Figure 5.10 demonstrates the described phenomenon.

In the second multi-step μCT experiment, a SCD PI aerogel film of 59 micron thickness was applied at the four interfaces in the 5-ply IM7/8552 laminate. The material properties for this film can be found in Table 4.2 under the name Aerogel PI 50 μm. The aerogel was manually applied via a cylindrical roller to the thawed prepreg at each interlaminar region. No other processing procedures were performed relative to the first experiment without applied NPN. At Step 0 of this trial, large interlaminar voids are shown in connection to the aerogel NPN. This entrapped air from the manual layup process is especially apparent in the top-left quadrant of the imaged reconstructed scan, Figure 5.11a. After the first heating step of 60 °C for 15 minutes, the aerogel NPN provided an evacuation pathway for interlaminar-located entrapped voids. Small, intralaminar voids were present at this step of the experiment that did not exist in Step 0. The aerogel film noticeably compressed within this step, as well. As the next heating step occurred, these intralaminar (although also extending to interlaminar region at times) voids expanded in size, which was a similar behavior to the study without NPN. Additionally, the NPN appeared to become saturated in the center of the scan due to indistinguishable pixel color between the CFRP laminate and NPN. In the final step, the intralaminar voids continued to grow, indicating that the NPN can provide migration pathways for interlaminar connected voids, but cannot mitigate against the growth of voids in resin-rich regions within the lamina.

In the third multi-step μCT experiment, the same aerogel film was applied in the four interlaminar regions of IM7/8552 woven composite. However, the prepreg was pre-processed in a procedure termed desolventing. Within this work, desolventing refers to a process of removing residual solvent of a prepreg lamina through the use of vacuum and applied

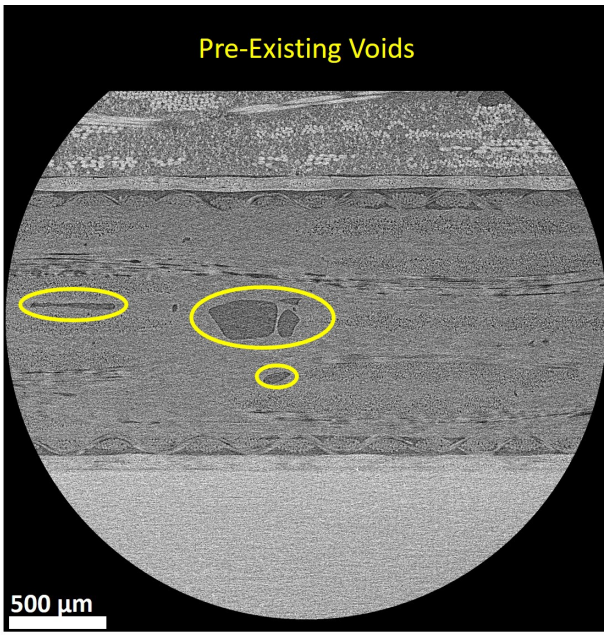
temperature. Before the μCT experiment, the IM7/8552 woven composite prepreg laminae was desolvented via a vacuum oven with the following conditions: $\sim$ 10 millibar and 60 °C for 60 minutes. There is no expectation of gelation for these temperature and time conditions [46]. One side of the lamina is exposed to the vacuum to ensure no blockage of volatiles extraction. Once the laminae are desolvented, the aerogel is applied in the same process as written above to create the laminate for the μCT experiment. In Step 0 of this experiment, there is evidence of large voids connected to the interlaminar region, confirmed by the top-center portion of the imaged scan, Figure 5.12a. The aerogel NPN provides the evacuation route to remove these connected voids, similar to OoA prepreg. The aerogel NPN also reduces in thickness, behavior seen in the previous aerogel NPN multi-step μCT experiment. In Step 2 and Step 3 of this third experiment, there is no longer void expansion present within the laminate, indicating that desolventing removes the intralaminar voids caused by prepreg manufacturing. Applying both NPN and the desolventing procedures allows for successful void removal of these woven laminates in this in situ μCT experiment. This is discussed further in Chapter 6.

While invaluable data was discovered from these experimental trials, each scan took 18-22 hours. Therefore, each of the three experiments, which represent the first 45 minutes of the IM7/8552 cure cycle, took a little under a week to complete. In order to gain observations for the entire cure cycle, this experiment should be performed using SCRT for maximum benefits.

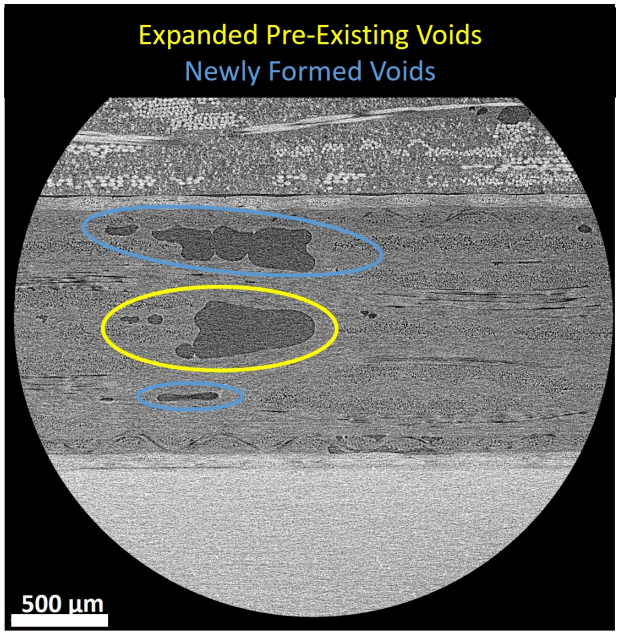
5.4 Summary

In this chapter, two in situ experiment types were developed to monitor the resin flow front through a NPN and to observe the void evolution throughout the cure cycle of CFRP woven composite laminates. The thermal-mechanical experimental set-ups were described and the limitations of these designs were expressed throughout this chapter. Employing SCRT with

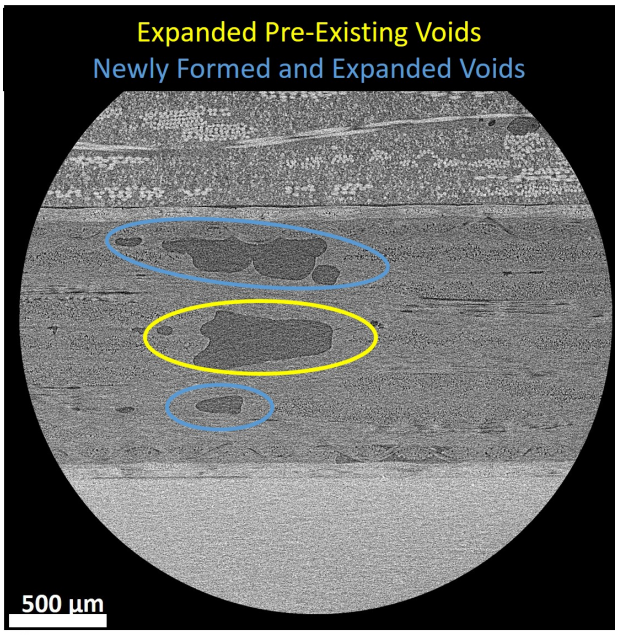
the 2D flow monitoring experiment would allow for the potential validation of the Newtonian flow front model. Additionally, real-time visual monitoring of laminates during their entire cure cycle could be achieved with the void observational experiment, leading to the collection of unprecedented data. From the results of the multi-step μCT void observation experiment, manufacturing procedures of IM7/8552 woven composites should be altered to reduce the expansion of voids during the cure cycle. After 15 minutes of 60 °C, voids emerged and expanded in resin-rich regions of untreated prepregs. NPNs could not remove these voids by the end of the 45-minute trial. However, when heat-treating the laminae under vacuum, void growth was stunted and NPNs removed existing interlaminar voids. Application of these techniques with various NPNs and laminate sizes is provided in Chapter 6.



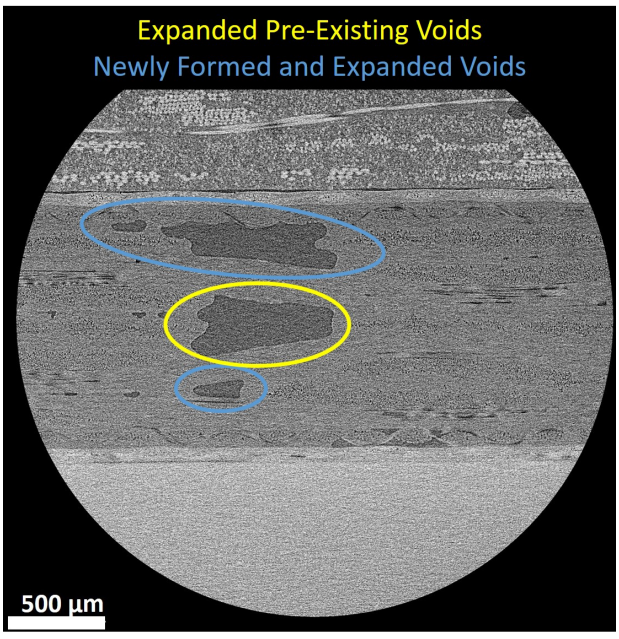
(a) Step 0 of the multi-step μCT experiment with $[0]_5$ woven IM7/8552 composite (no applied NPN). No heat (only vacuum) has been applied to this laminate. Intralaminar (oftentimes intersecting the interlaminar region) voids are present.



(b) Step 1 of the multi-step μCT experiment with $[0]_5$ woven IM7/8552 composite (no applied NPN). 15 minutes of 60 °C with vacuum has been applied. Expanded intralaminar voids are present.

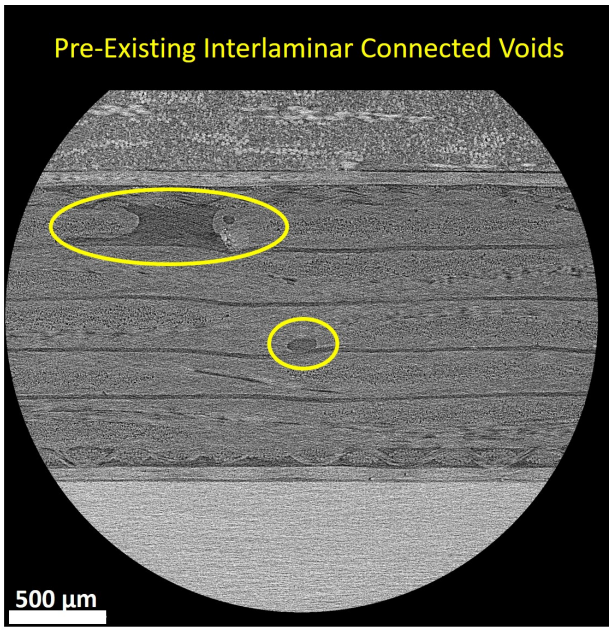


(c) Step 2 of the multi-step μCT experiment with $[0]_5$ woven IM7/8552 composite (no applied NPN). 30 minutes of 60 °C with vacuum has been applied. Further expanded intralaminar voids are present.

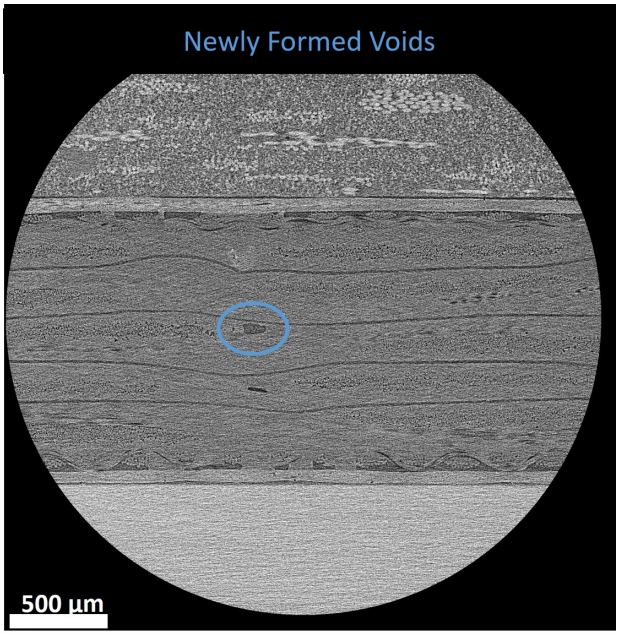


(d) Step 3 of the multi-step μCT experiment with $[0]_5$ woven IM7/8552 composite (no applied NPN). 45 minutes of 60 °C with vacuum has been applied. Expanded and coalesced intralaminar voids are present.

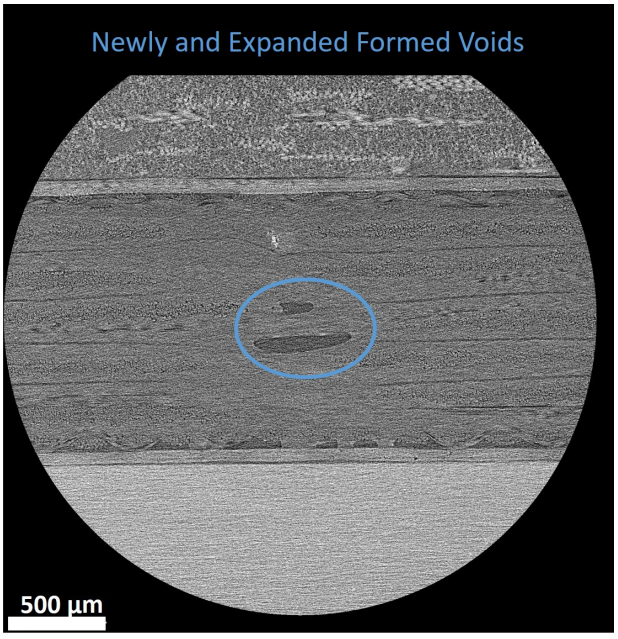
Figure 5.10: $[0]_5$ woven IM7/8552 laminate with no applied NPN and no desolventing for the first multi-step μCT experiment.



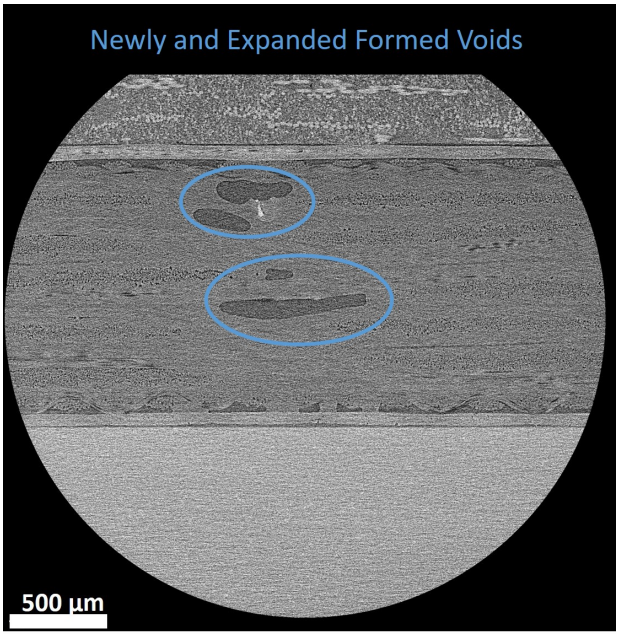
(a) Step 0 of the multi-step μCT experiment with $[0]_5$ woven IM7/8552 composite with applied SCD aerogel NPN. No heat (only vacuum) has been applied to this laminate. Interlaminar-connected and intralaminar voids are present.



(b) Step 1 of the multi-step μCT experiment with $[0]_5$ woven IM7/8552 composite with applied SCD aerogel NPN. 15 minutes of 60 °C with vacuum has been applied. Minimal intralaminar voids are present.

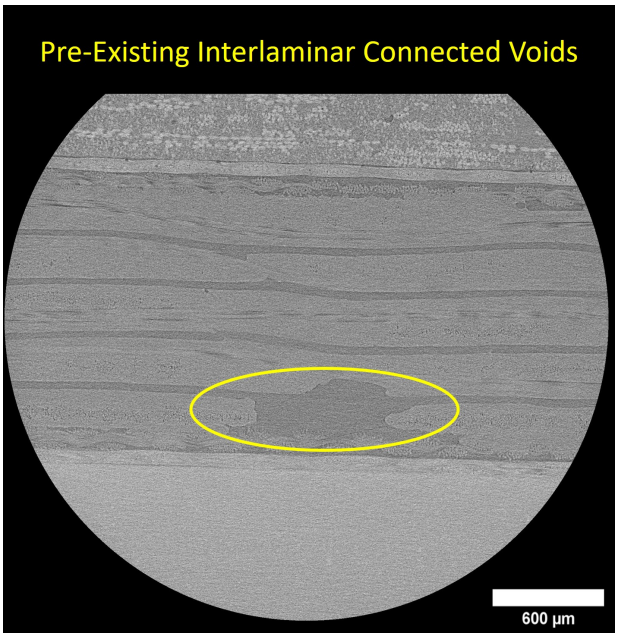


(c) Step 2 of the multi-step μCT experiment with $[0]_5$ woven IM7/8552 composite with applied SCD aerogel NPN. 30 minutes of 60 °C with vacuum has been applied. Expanded intralaminar voids are present.

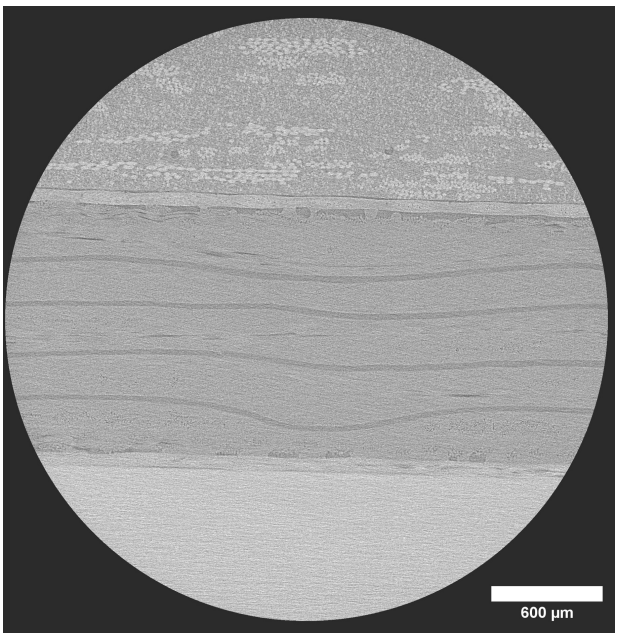


(d) Step 3 of the multi-step μCT experiment with $[0]_5$ woven IM7/8552 composite with applied SCD aerogel NPN. 45 minutes of 60 °C with vacuum has been applied. Further expanded and coalesced intralaminar voids are present.

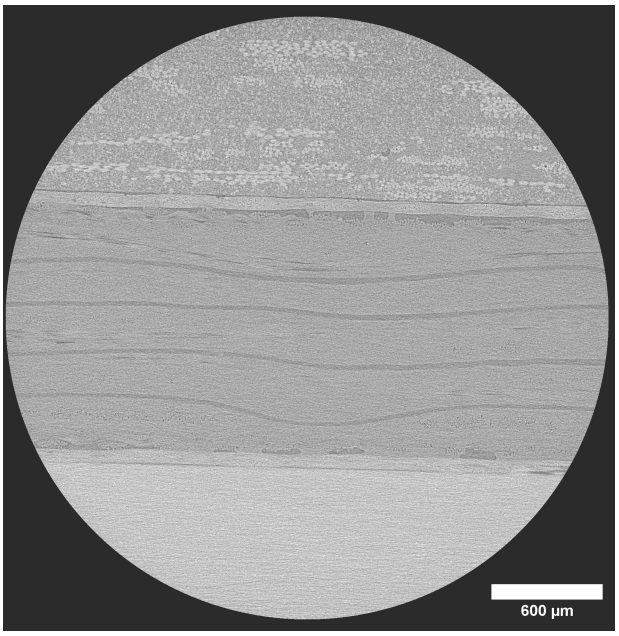
Figure 5.11: $[0]_5$ woven IM7/8552 laminate with aerogel NPN (named Aerogel PI 50 μm) and no desolventing processing for the second multi-step μCT experiment.



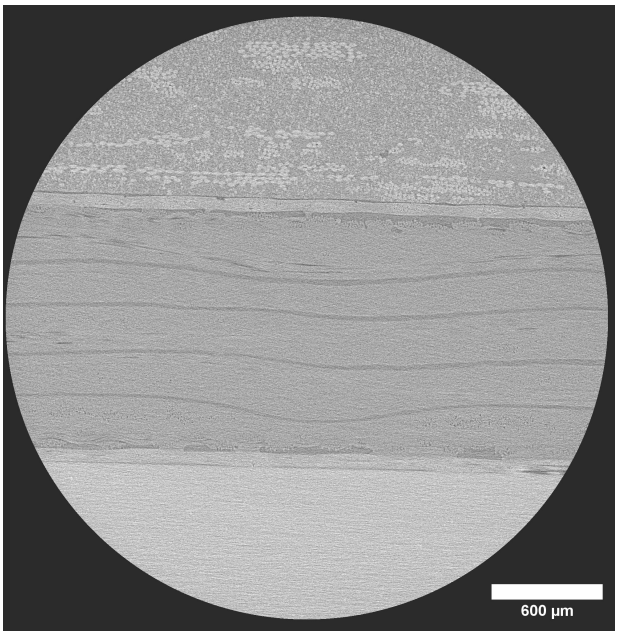
(a) Step 0 of the multi-step μCT experiment with $[0]_5$ woven IM7/8552 composite with applied SCD aerogel NPN. No heat (only vacuum) has been applied to this laminate. Interlaminar-connected voids are present.



(b) Step 1 of the multi-step μCT experiment with $[0]_5$ woven IM7/8552 composite with applied SCD aerogel NPN. 15 minutes of 60 °C with vacuum has been applied. No voids have grown from Step 0.



(c) Step 2 of the multi-step μCT experiment with $[0]_5$ woven IM7/8552 composite with applied SCD aerogel NPN. 30 minutes of 60 °C with vacuum has been applied. No voids have grown from Step 1.



(d) Step 3 of the multi-step μCT experiment with $[0]_5$ woven IM7/8552 composite with applied SCD aerogel NPN. 45 minutes of 60 °C with vacuum has been applied. No voids have grown from Step 2.

Figure 5.12: $[0]_5$ woven IM7/8552 laminate with aerogel SCD NPN (named Aerogel PI 50 μm) and desolventing processing for the third multi-step μCT experiment.

Chapter 6

Manufacturing and Void Analysis of IM7/8552 Woven Autoclave Prepreg with Nanoporous Networks

Within this chapter, the vacuum-bag-only (VBO) manufacturing process will be presented in detail to demonstrate the application of nanoporous networks (NPN) into IM7/8552 woven laminates. Two principal systems of NPN will be assessed: polyimide (PI) aerogel and electrospun polymer nanofibers (EPN). Experimental results of the NPN integration will be provided via void content analysis and representative microcomputed tomography (μCT) scans. The results of this chapter advance the feasibility of VBO-manufacturing aerospace, autoclave prepreg with the use of NPN, for efforts of energy-savings via removal of the autoclave from carbon fiber reinforced polymer (CFRP) composite processing.

6.1 Manufacturing Process for Transferring NPN into the Interlaminar Region of Autoclave Aerospace-grade CFRP Composites

Depending on the NPN and the tackiness of the autoclave prepreg, there are various techniques to integrate the NPN within composite interlaminar regions by increasing the contact between the surface of the NPN and the adjacent lamina surface. As mentioned in previous sections, EPN films and PI aerogel films are the primary NPNs investigated with here, partly due to their material continuity. The investigated EPN films, EPN 12 μm and EPN 21 μm (see Chapter 4), are applied to the lamina directly with pressure applied by hand rolling. Backing paper attached to the EPN film is then pulled off of the laminate and NPN assembly. For woven IM7/8552 composites, PI aerogel films follow a similar transfer procedure of the EPNs. However, as a note, PI aerogel films are less flexible than the EPNs possibly suggesting a need for techniques to maximize surface area contact for less tacky composite systems. In these particular scenarios, heat and additional pressure can be used to create the needed connection between the NPN and surrounding laminae. Past work with unidirectional CFRP IM7/8552 and unidirectional glass fiber reinforced polymers (GFRP) composites, specifically 913/30%/UD192/EC9 673517 prepreg, has indicated heat is needed in the application of PI aerogel film to the laminae surfaces to assist with transfer [30, 92]. The specifics of NPN application for woven IM7/8552 composite manufacturing are described in the following sections within this chapter.

6.2 IM7/8552 Autoclave Woven Composites

Hexply ® 8552 is a common epoxy system used in primary aircraft structures, engines, helicopters, space launchers, medical equipment, and more [121]. This polymer resin system is

a low flow system that has a service temperature of approximately 120 °C or 250 °F. In the following sections, the cure profile, VBO-procedure, and layup procedure with the insertion of NPN will be described in detail for this composite system. Information about the woven prepreg can be found in Table 6.1.

Table 6.1: Material characteristics for IM7/8552 prepreg composite system [46].

IM7/8552 Woven Carbon Prepreg	**Material Characteristics**
Fiber	IM7 Fiber, 6K Tow
Nominal Fiber Volume %	55.57 vol%
Fiber Density	1.77 g/cm^3
Resin	HexPly ® 8552
Nominal Resin Density	1.301 g/cc
Weave	Plain
Cured Ply Thickness	0.199 mm
Glass Transition Temperature, T_g Dry	200 °C

A baseline, autoclave-manufactured IM7/8552 $[0]_{12}$ laminate with no applied NPN is provided in Figure 6.1 to supply a point of comparison to the VBO-manufactured laminates within this chapter. This baseline laminate was processed with the cure cycle provided in Figure 2.2.

6.2.1 Cure Profile and Layup Process of IM7/8552 VBO-Manufactured Composites

For this thesis, woven laminates were positioned such that all laminates follow the layup orientation of $[0]_N$, where N represents the amount of plies within the assembled laminate. Using the following initial procedure, the laminate was manufactured before being inserted in the VBO-curing assembly shown in Figure 6.2:

1. Cut woven laminates to the desired dimensions. Typically square panels are produced.

2. Remove backing paper from one surface of all CFRP prepreg.

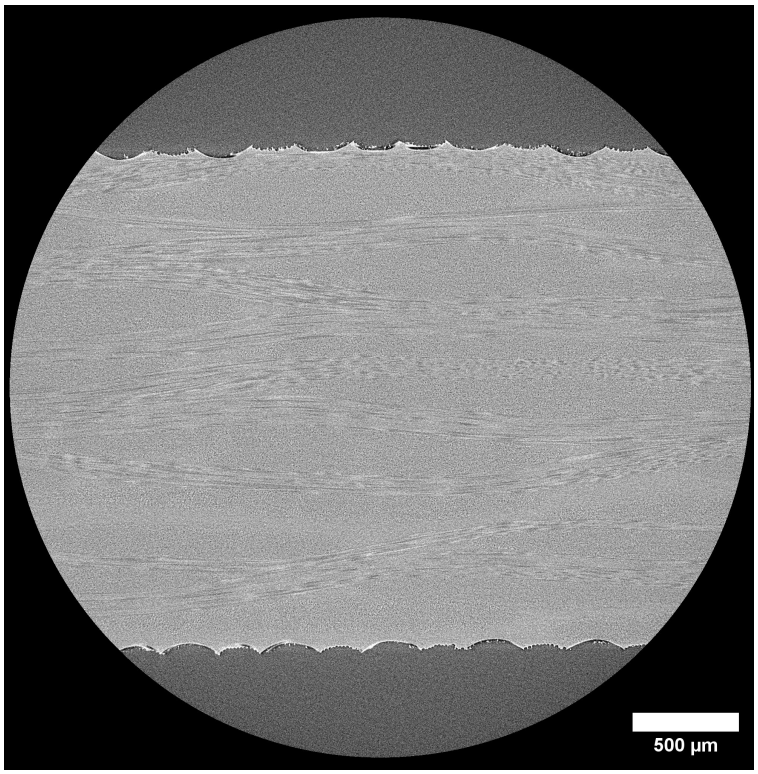


Figure 6.1: A reconstructed μCT scan of a baseline, autoclave-manufactured IM7/8552 woven $[0]_{12}$ laminate with no applied NPN. No voids are present throughout the laminate at the utilized pixel size. For this scan, the pixel size was 1.77 μm with an exposure time of 2.5s. The voltage of the scan was 100 kV with an applied filter of LE2 to increase overall transmittance.

3. Place one bare CFRP prepreg on a flat layup surface covered with guaranteed non-porous Teflon (GNPT) to initiate laminate stacking.

4. Apply NPN to one lamina surface.

   (a) PI Aerogel Application: Place the exposed CFRP prepreg lamina surface onto the aerogel film. Using a manual roller, apply light pressure on the prepreg backing paper to adhere the aerogel to the prepreg surface. Cut the aerogel to allow for an overhang of under a millimeter on each side of the CFRP prepreg. Using tweezers, pull the CFRP prepreg and attached aerogel from the surrounding aerogel film.

   (b) EPN Application: Pre-cut the EPN film in the dimensions of less than a millimeter larger than the desired CFRP dimensions around the perimeter. Place the cut

EPN membrane on top of the cut CFRP lamina. Using a manual roller, apply light pressure to adhere the EPN to the prepreg surface. Using tweezers, separate the backing paper from the EPN film.

5. Place the NPN covered CFRP lamina on top of the bare CFRP prepreg such that the NPN makes contact with a bare CFRP lamina surface. There should be backing paper on the top of this assembly.

6. Using a manual roller, apply light pressure over the entire assembly, on top of the backing paper, to assist in the conformability of the NPN to the surrounding laminae. Remove the backing paper after completing the manual rolling.

7. Complete this procedure N-1 times, where N is the total number of plies in the manufactured laminates, to fabricate the laminate with NPN.

Once the layup is completed, peel ply is applied to the top and bottom surface of the laminate for a consistent surface finish. Surrounding the laminate, breathable cork dams are layered to extend past the thickness of the laminate, but not extend past the height of the laminate and associated caul plate assembly to control the edge resin flow. The caul plate used to compress the laminate in the VBO assembly is wrapped in GNPT (Airtech Release Ease 234 TFNP) film to prevent resin from contacting the caul plate. The dimensions of the caul plate match that of the curing laminate, are at least 1 mm thick, and the composition is typically aluminum to withstand the cure cycle temperatures. Breather (Northern Composites BR-NB3010) is placed over the entire resin dam, laminate, and caul plate assembly. In addition, the breather is in contact with the cork dam to create a breathable pathway for gases or volatiles to evacuate from. To complete the VBO set-up, a vacuum bag (Airtech Wrightlon 8400) is sealed against the aluminum tool plate using sealant tape (TACKY TAPE® SM5126). A vacuum port is connected through the vacuum bag and placed on the breather to aid in the removal of gaseous voids throughout the laminate through use of a

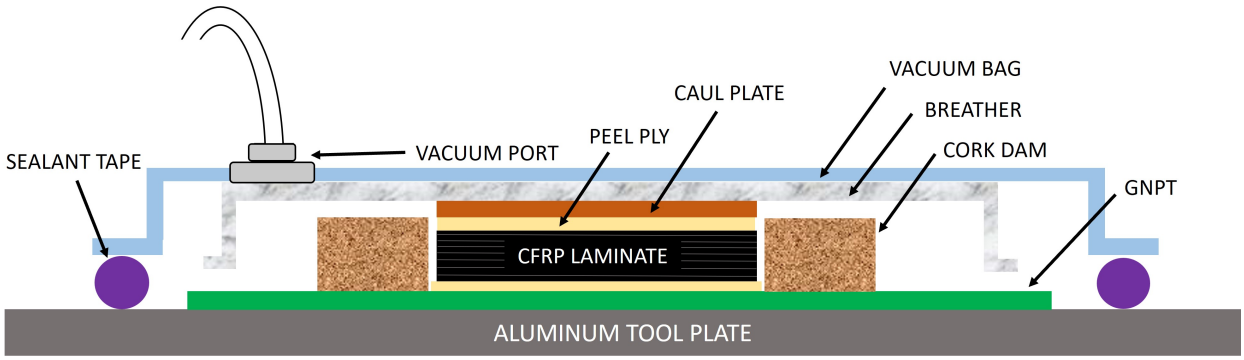


Figure 6.2: VBO assembly used for all CFRP laminates manufactured within this thesis. This system is placed within an oven to complete the cure cycle's temperature requirements.

rotary vane vacuum pump (Vacuubrand® RZ 2.5). An illustration of the VBO cure set-up is provided in Figure 6.2.

To cure all VBO-manufactured IM7/8552 composites, the manufacturer recommended cure cycle (MRCC) in Figure 2.2, sans applied pressure, was conducted following a 3 hour debulk at an elevated temperature of 60 °C. A heating ramp rate of 3°C/min and a cooling ramp rate 2°C/min were applied to the laminates, which is within the range of ramp rates provided by the MRCC. A debulk temperature of 60 °C was selected to aid in the consolidation of the laminate via a decrease in resin viscosity and promote the conformability of NPN to the surrounding laminae surfaces. A three hour debulk preceded the MRCC to allow trapped gas to evacuate the laminate before NPN saturation at higher temperatures, functioning similarly to out-of-autoclave (OoA) prepreg debulking procedures. For all cures, the vacuum achieved 96.51 kPa (28.5 in Hg) and is maintained for the entire cure cycle. These laminates were produced within an oven (Thermo Scientific™ Heratherm™ Advanced Protocol Oven 51028126). With the use of the Heratherm™ oven, a consistent convective heating method, multiple laminates could be cured simultaneously for faster processing.

However, when investigating the quality of the laminates through the use of Zeiss Versa 620, a μCT microscope, there were noticeable voids located throughout the laminate. Specifically, these voids were continuous in structure and both intralaminar and interlaminar in nature, creating CFRP composite specimens with large void content. An image of a cross-

sectional scan of a VBO and oven manufactured CFRP laminate with AD PI aerogel NPN is provided in Figure 6.3. The thickness of this aerogel NPN was approximately 41 microns. The voids in the interlaminar region were thin and oftentimes continuous, while the intralaminar voids had a more curved shape.

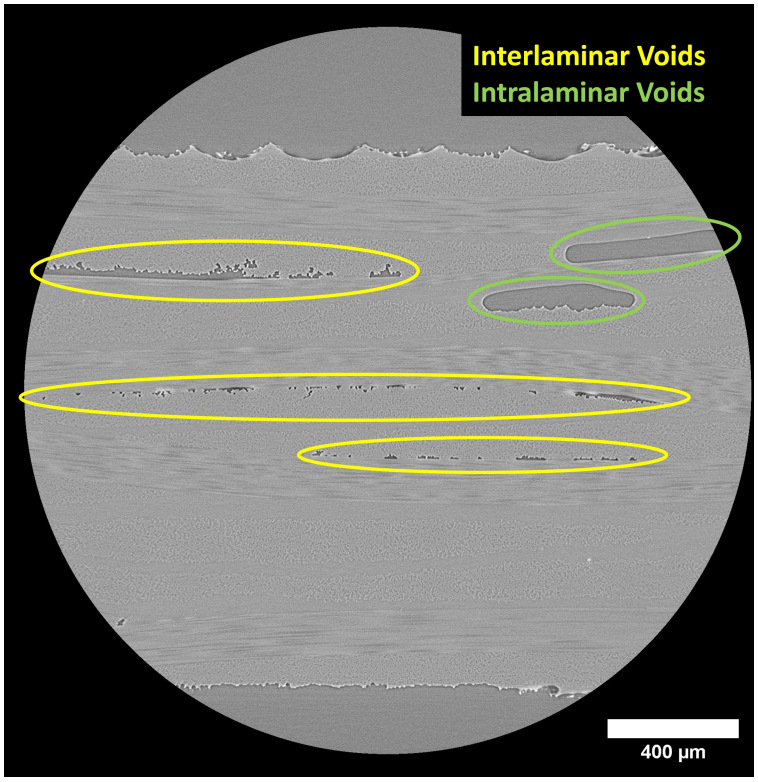


Figure 6.3: A reconstructed μCT scan of an IM7/8552 woven $[0]_8$ laminate with AD PI Aerogel NPN. The dark gray regions represent an absence of material indicating large void content, in both the intralaminar and interlaminar regions, of this manufactured CFRP composite. For this scan, the pixel size was 1.17 μm with an exposure time of 3s. The voltage of the scan was 120 kV with an applied filter of LE1 to increase overall transmittance. No special processing was performed on this laminate.

These results inspired the development of the 3D in situ μCT experiment explained in Chapter 5. Utilizing the results of the 3D in situ experiment and the volatile graph provided in section 4.2.1, a heat treatment step was added to the previous VB0-curing procedure to mitigate the creation of thermally expansive voids originating from prepreg volatiles. By placing exposed laminae in a vacuum oven at elevated temperatures, residual solvent can be extracted from the prepreg in a procedure termed desolventing. The new layup procedure

with desolventing follows the procedure written above, but with one additional step placed as 2.1 in the above procedure (following step 2):

2.1 Place the CFRP laminae, exposed side up, in a vacuum oven (vacuum achieved is typically 10 millibars or less) for 60 minutes at 60 °C. There should be noticeable bubbles on the top of the laminae during this process.

Steps 3 through 7 of the previous procedure are followed in the same manner after step 2.1 is completed. Using this updated procedure, low void content IM7/8552 laminates were fabricated with the results being shown in the next section.

6.2.2 Quality of Manufactured Laminates

To check for the existence of voids with micron-scale resolution, μCT was used to investigate the internal composition of the manufactured laminates. A pixel size of approximately 2 microns was used for each scan or less, resulting in an resolution of 6 microns or less with the usual rule that resolution is approximately 3 times the pixel size. Tape was used on multi-laminate μCT scans to assist in laminate identification. The tape is labelled on the images for further clarity. A test matrix, in Table 6.2, of VBO-manufactured square woven laminates was investigated for their void content with the results given in Table 6.3. In Table 6.2, laminate side dimensions refer to the side length of the manufactured IM7/8552 woven square laminates.

Figure 6.4 shows a μCT scan of a VBO-manufactured laminate without NPN, and the resulting voids. Figures 6.5, 6.6, 6.7, all 25.4 mm (1-inch) specimens VBO-manufactured with NPN, regardless of type, produced low void-content 5-ply CFRP laminates below the 1 vol% aerospace standard for voids. The necessity of NPN is illustrated by the high void content (over 3 vol%) of the 25.4 mm (1-inch) laminate VBO-manufactured without NPN, shown in Figure 6.4. However, when increasing the surface area and ply number of the laminates, only the AD PI aerogel film is able to reduce the void content below 1 vol%. The

AD PI aerogel film was selected as the primary aerogel film candidate after the 25.4 mm (1-inch) scale manufacturing. The void content raises to approximately 1.8 vol% when using the thin EPN 12 μm NPN at the 76.2 mm (3-inch) scale. The hypothesis for this behavior is directly correlated to surface area. As entrapped gases and gaseous volatiles are evacuating the laminate, the NPN is too thin to allow for proper migration. The pathways at the edges of the laminate become unavailable as the NPN becomes saturated, leaving gases towards the center of the laminate no path of evacuation. This results in pervasive voids in interlaminar and intertow regions. At the 152.4 mm (6-inch) scale, the AD PI aerogel film still performs as an effective evacuation medium.

Table 6.2: All VBO-manufactured woven IM7/8552 square, flat-panel composite laminates studied. In brackets is a reference to the representative μCT scan of that laminate. Each laminate name contains the side length of the manufactured laminate in inches. All laminates are produced with the desolventing procedure at 60°C and ~10 millibar for 60 min, including the laminate without NPN.

Laminate Name [Figure Number]	Number of Plies	NPN Used (Thickness)	Laminate Side Dimensions [mm (in.)]
Laminate IM7/8552 No-NPN 1" [6.4]	5	None	25.4 (1)
Laminate IM7/8552 SCD Aerogel I 1" [6.5]	5	SCD PI Aerogel (59 microns)	25.4 (1)
Laminate IM7/8552 SCD Aerogel II 1" [6.5]	5	SCD PI Aerogel (40-60 microns estimated)	25.4 (1)
Laminate IM7/8552 AD Aerogel 1" [6.6]	5	AD PI Aerogel (74.7 microns)	25.4 (1)
Laminate IM7/8552 EPN 12 μm 1" [6.7]	5	EPN 12 μm (12 microns)	25.4 (1)
Laminate IM7/8552 EPN 12 μm 3" [6.8]	8	EPN 12 μm (12 microns)	76.2 (3)
Laminate IM7/8552 AD Aerogel 3" [6.9]	8	AD PI Aerogel (74.7 microns)	76.2 (3)
Laminate IM7/8552 AD Aerogel 6"	12	AD PI Aerogel (74.7 microns)	152.4 (6)

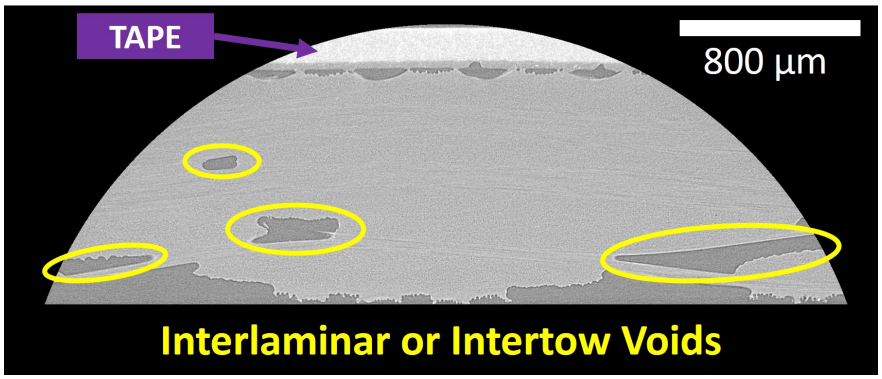


Figure 6.4: Representative cross-sectional view of the IM7/8552 woven laminate without applied NPN manufactured via VBO and oven at the 25.4 mm (1-inch) scale. Large voids are present throughout the laminate with the calculated void content being 3.176 vol%. This scan was produced 1.91 μm pixel size, 3 second exposure, voltage of 80 kV, and with a LE2 filter.

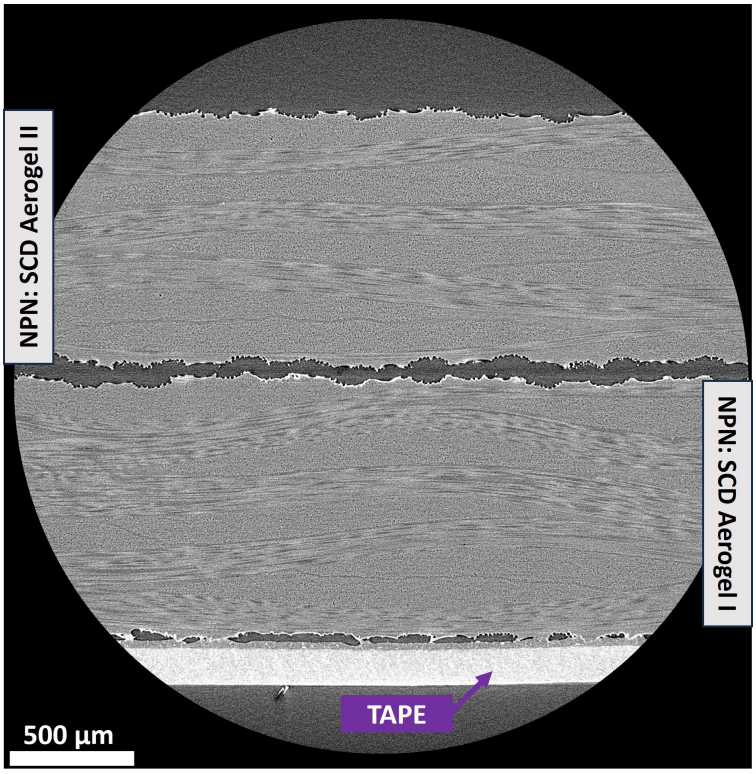


Figure 6.5: Representative cross-sectional view of the two IM7/8552 woven laminates with SCD PI aerogel NPN produced with VBO and oven at the 25.4 mm (1-inch) scale. The top laminate corresponds to Laminate IM7/8552 SCD Aerogel II 1" and the bottom laminate corresponds Laminate IM7/8552 SCD Aerogel I 1". The void content of the top laminate is 0.170 vol%, while the bottom laminate has a void content of 0.162 vol%. This scan was produced using 1.55 μm pixel size, 3 second exposure, voltage of 100 kV, and with a LE2 filter.

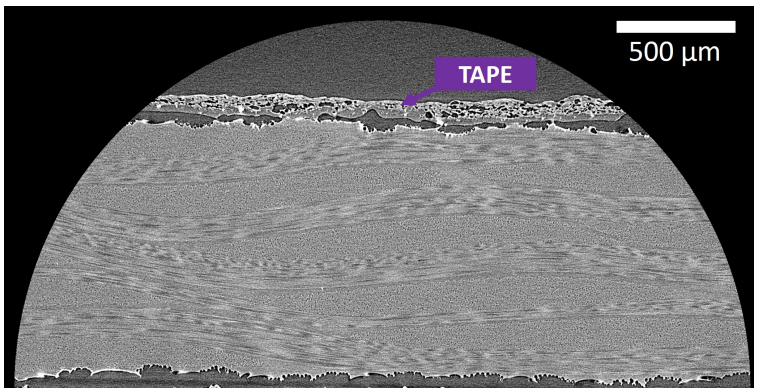


Figure 6.6: Representative cross-sectional view of the IM7/8552 woven laminates with AD PI aerogel NPN manufactured via VBO and oven at the 25.4 mm (1-inch) scale. The void content of this laminate is 0.035 vol%. This scan was produced using 1.59 μm pixel size, 3 second exposure, voltage of 80 kV, and with a LE1 filter.

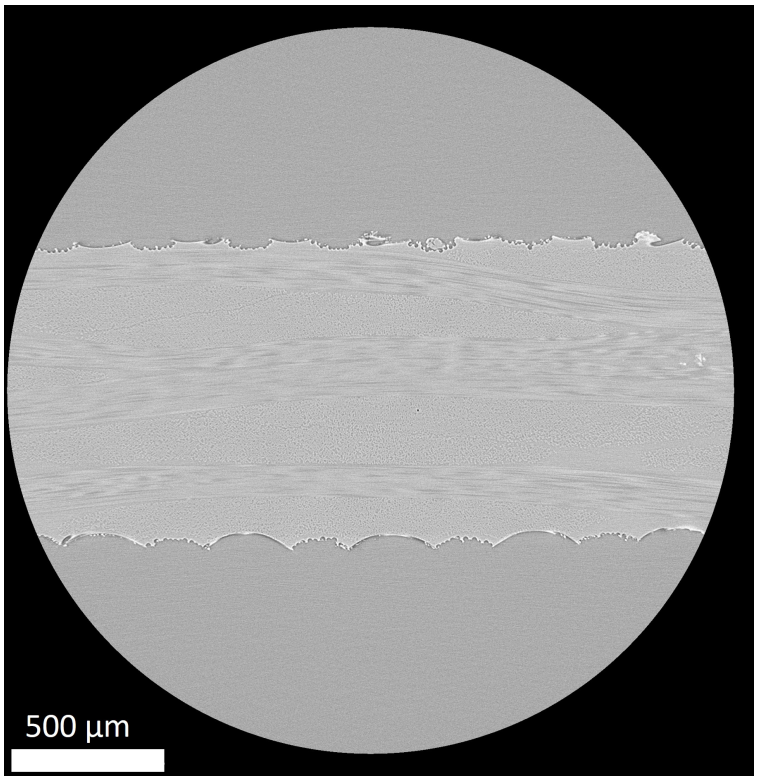


Figure 6.7: Representative cross-sectional view of the IM7/8552 woven laminate with EPN 12 μm NPN produced with VBO and oven at the 25.4 mm (1-inch) scale. The void content of this laminate is 0.003 vol%. This laminate has the lowest void content of the manufactured 25.4 mm (1-inch) laminates. This scan was produced using 1.24 μm pixel size, 4 second exposure, voltage of 80 kV, and with a LE2 filter.

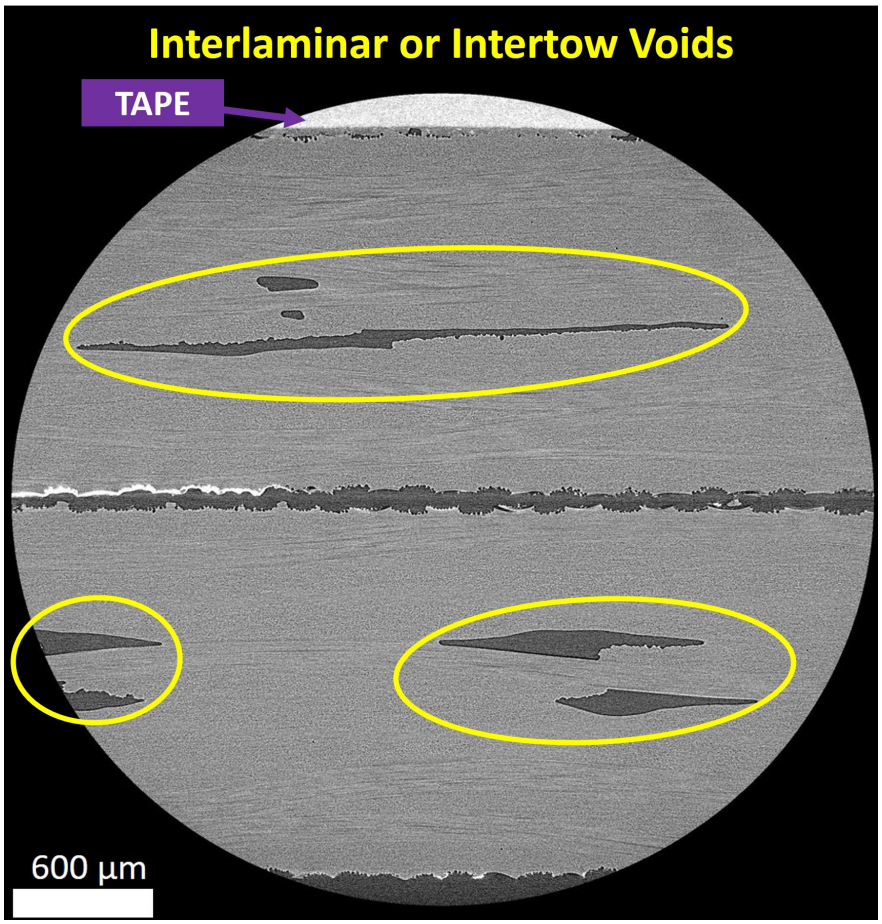


Figure 6.8: Representative cross-sectional view of the IM7/8552 woven laminate with EPN 12 μm NPN produced with VBO and oven at the 76.2 mm (3-inch) scale. The two scanned specimens are of the same laminate, but from different locations. This laminate has the highest void content of the manufactured 76.2 mm (3-inch) laminates. Noticeable voids are present throughout the laminate at the utilized pixel size with the laminate void content being 1.843 vol%. This scan was produced using 1.87 μm pixel size, 4 second exposure, voltage of 80 kV, and with a LE3 filter.

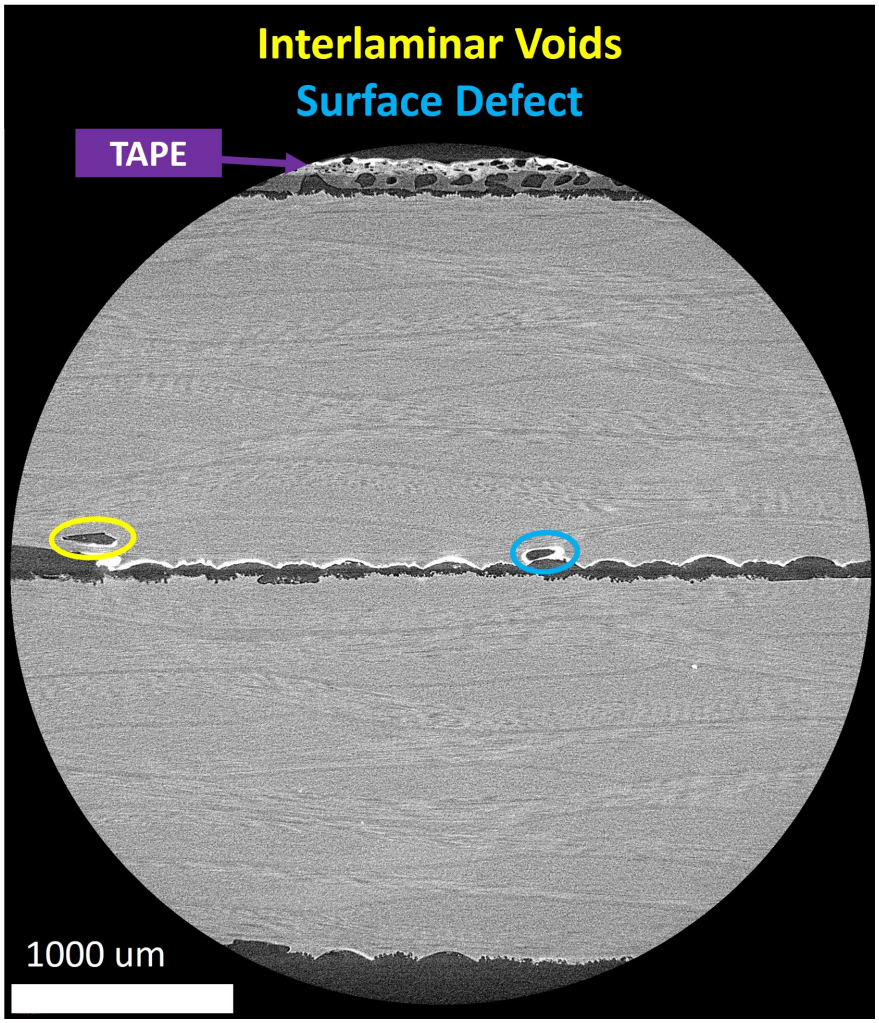


Figure 6.9: Representative cross-sectional view of the IM7/8552 woven laminate with AD PI aerogel NPN produced with VBO and oven at the 76.2 mm (3-inch) scale. The two scanned specimens are of the same laminate, but from different locations. The void content of this laminate is 0.16 vol%. This laminate has the lowest void content of the manufactured 76.2 mm (3-inch) laminates. This scan was produced using 2.01 μm pixel size, 4 second exposure, voltage of 80 kV, and with a LE3 filter.

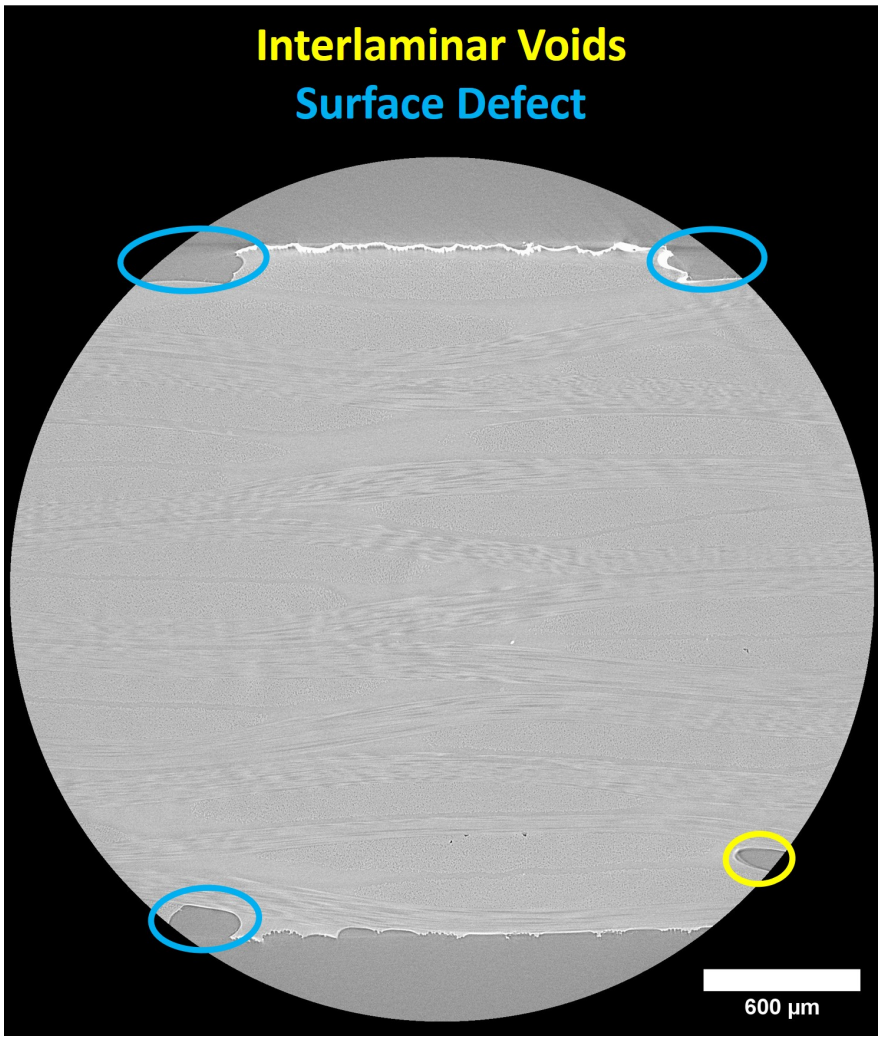


Figure 6.10: Representative cross-sectional view of the IM7/8552 woven laminate with AD PI aerogel NPN produced with VBO and oven at the 152.4 mm (6-inch) scale. The two scanned specimens are of the same laminate, but from different locations. The void content of this laminate is 0.112 vol%. This laminate is beneath the void content limit of 1 vol% often required for aerospace composite structures. This scan was produced using 1.68 μm pixel size, 4 second exposure, voltage of 80 kV, and with a LE1 filter.

To calculate the void content of each laminate, ImageJ, a popular image processing software, was applied to the TIFFs of the reconstructed scans. For μCT scans completed on CFRP laminates, 3201 projections are used for superior image reconstruction and accuracy of reconstructed dimensional information [122]. 3201 projections typically results in approximately 2000 cross-sectional reconstructed images of the scanned CFRP laminates in the file format of TIFFs for their high quality retention. For this composite system, 10 TIFFs are selected for void investigation, with the evenly spaced distribution of image selection being 50, 250, 450, 650, 850, 1050, 1250, 1450, 1650, 1850 in the approximate group of 2000. Within the images, only the laminate should be appear; the surrounding air and any non-laminate material should be cropped out of the image. Once the laminate-only images are imported in ImageJ, a plugin named Trainable Weka Segmentation is used to train a classifier to recognize voids within a laminate. There are two classes within the classifier; in this specific context, the 2 classes are (1) voids and (2) resin, carbon fiber, or NPN, within the VBO-manufactured laminate. Once the classifier is trained, after selecting "train classifier", a binary image of red and green pixels is created to display the two classes of materials, voids and non-voids respectively. Once the two-tone image is generated, the area percentage of both can be calculated via ImageJ. Completing this process for a minimum of ten times allows for a void vol% evaluation. Increasing the amount of evaluated reconstructed images, increases the accuracy of the void vol% calculation. A visual diagram displaying the procedure is provided in Figure 6.11.

In addition to the void vol% of the VBO-manufactured NPN-integrated laminates, the total thickness of these laminates were measured to compare against autoclave-manufactured laminates without NPN. The two sets of IM7/8552 woven $[0]_{12}$ laminates were: (1) manufactured via autoclave with no applied NPN and (2) VBO-manufactured with oven and AD PI aerogel NPN applied at every interlaminar region. The autoclave laminate was produced as a 304.8 mm by 304.8 mm panel, while the VBO-manufactured laminate with AD PI aerogel NPN was produced as a 152.4 mm by 152.4 mm panel. Using digital calipers,

the thicknesses of the two laminates can be found in Table 6.4. 5 sample specimens of each laminate set were measured. The average increase in each interlaminar region was estimated to be approximately 16 microns, using the difference in laminate thicknesses and the number of interlaminar interfaces (11). Future mechanical testing will be done on these two sets of laminates to determine the influence of integrated NPN within interlaminar regions.

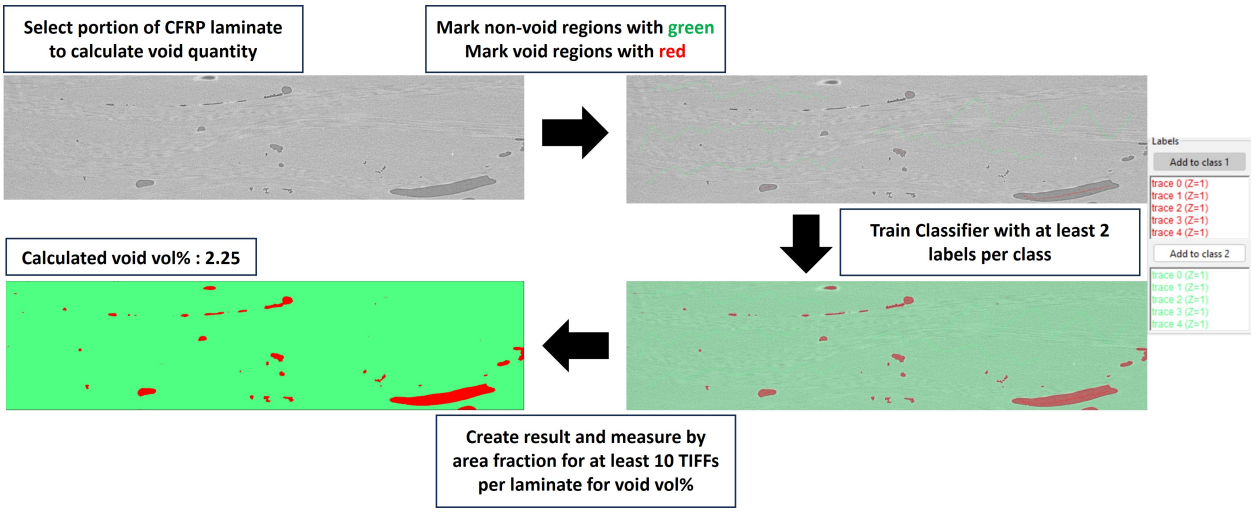


Figure 6.11: A visual demonstrating the calculation process for void vol% for all CFRP manufactured laminates. 10 TIFFs are completed for each analyzed laminate to obtain a void vol%. Voids are represented by red regions, while non-voids (resin, fiber, NPN) are represented by green regions. In the figure, 2.25 void vol% represents the calculated void area (colored red) of the example TIFF.

Table 6.3: Void content percentages of the IM7/8552 VBO-manufactured laminates. The desovlenting process of ∼10 millibar and 60 °C was applied to all laminates for 60 minutes. To calculate these results, 10 evenly spaced TIFFs were selected from the reconstructed 2D slices using ImageJ. The standard error listed for each laminate is the standard deviation of the void vol% for the 10 TIFFs divided by the square root of the TIFF set population (10).

Laminate Name	Void Vol% (± Standard Error)
Laminate IM7/8552 No-NPN 1"	3.176 ± 0.988
Laminate IM7/8552 SCD Aerogel I 1"	0.162 ± 0.032
Laminate IM7/8552 SCD Aerogel II 1"	0.170 ± 0.038
Laminate IM7/8552 AD Aerogel 1"	0.035 ± 0.016
Laminate IM7/8552 EPN 12 μm 1"	0.003 ± 0.0002
Laminate IM7/8552 EPN 12 μm 3"	1.843 ± 0.471
Laminate IM7/8552 AD Aerogel 3"	0.160 ± 0.033
Laminate IM7/8552 AD Aerogel 6"	0.112 ± 0.025

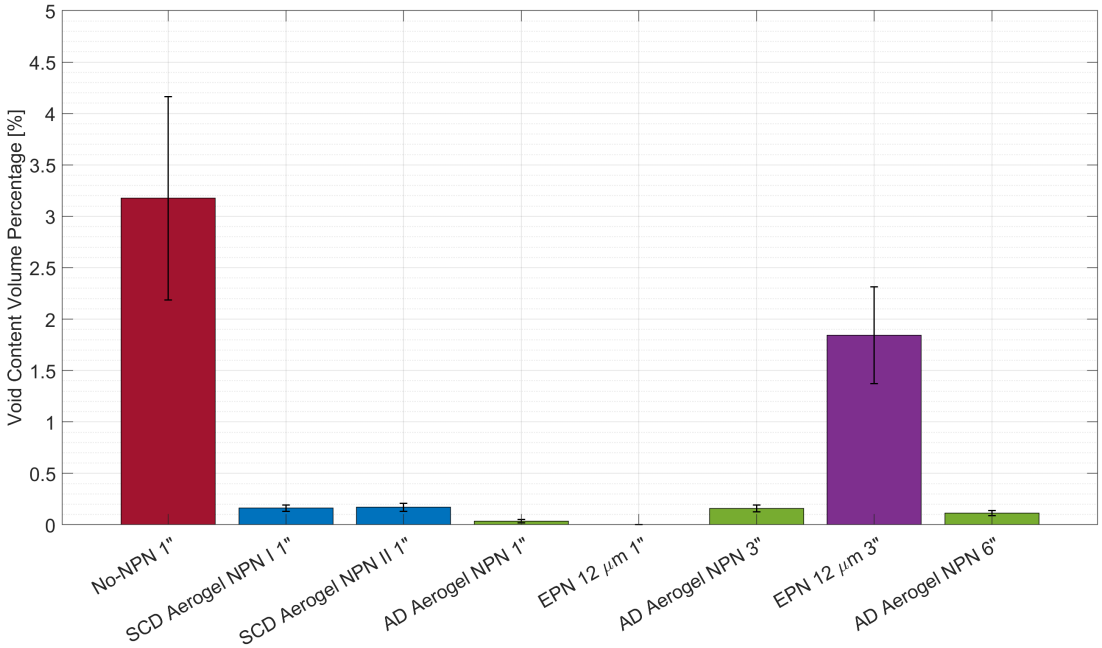


Figure 6.12: Void vol% of all VBO-manufactured IM7/8552 woven composites, including a standard error bar. The face colors of the bar chart, red, blue, green, and purple, indicate the applied NPN of no NPN, SCD PI aerogel, AD PI aerogel, and EPN 12 μm, respectively.

Table 6.4: Average laminate thicknesses of baseline autoclave manufactured and oven and VBO-manufactured IM7/8552 $[0]_{12}$ woven composites, along with calculated standard error. Standard error is defined as the standard deviation of the 5 thickness measurements per laminate set divided by the square root of the sample size (5).

Specimen Type	Thickness [mm] (± Standard Error)
Autoclave-Manufactured Baseline	2.47 ± 0.01
Oven & VBO-Manufactured with AD PI Aerogel NPN	2.65 ± 0.01

6.3 Summary

Within this chapter, it was demonstrated that low void content VBO-manufactured aerospace-grade autoclave woven composite laminates can be fabricated. By using discovered knowledge from the in situ experiments shown in Chapter 5, a new processing step, desolventing, could be applied to the laminae to remove residual solvent from prepreg manufacturing. Adding desolventing with the NPN integration process, laminates were VBO-manufactured using an elevated temperature debulk followed by the IM7/8552 MRCC. At small scales of 25.4 mm (1-inch) or less, all tested NPNs, SCD PI aerogel, AD PI aerogel, and EPN 12 μm produced specimens with 0.2 void vol% or less. At the 76.2 mm (3-inch) and 152.4 mm (6-inch) scale, only AD PI aerogel is able to produce specimens with a 0.2 void vol% or less. The thickness of the 12-ply laminate increased by 180 μm via VBO-manufacturing with AD PI aerogel NPN, resulting in an estimated average increase of 16 μm per interlaminar region. AD PI aerogel is proving to be a promising NPN candidate for IM7/8552 composite laminates. However, mechanical testing will be needed in future work to validate the integration of NPN and laminate thickness increase.

Chapter 7

Conclusions and Recommendations

Nanoporous networks (NPN) are materials recently introduced in fiber reinforced polymer (FRP) composites manufacturing with pore diameters ranging from tens of nanometers to several micrometers. By integrating the NPNs within the interlaminar region of FRP laminates, the induced capillary pressure within the pores of the NPN can replace autoclave pressure to produce void-free laminates. Aerospace-grade and autoclave formulated carbon fiber reinforced polymer (CFRP) laminates are fabricated with NPNs in a modified processing procedure via vacuum-bag-only (VBO) manufacturing. The modified manufacturing procedure introduced here is a pre-processing/manufacturing step to the prepreg laminae at low pressures and elevated temperatures, termed desolventing, enabled the creation of low void content composites. With the success of the NPN-enabled VBO-manufactured composites, there are further improvements in the overarching goal to replace the need for autoclaves in the manufacturing of aerospace-grade CFRP composites, including now woven composites. A summary of the thesis contributions, along with recommendations for future work, are presented.

7.1 Summary of Thesis Contributions

A list of thesis highlights is provided within this section to demonstrate the fundamentals of NPNs, along with their integration within CFRP woven composite laminates. The techniques used to achieve these contributions are delineated, as well.

Defining Nanoporous Networks and Their Function

NPNs were defined as materials integrated within the interlaminar region of FRP composites to reduce interlaminar void content. The fundamental behavior of NPNs was established through two primary characteristics: capillary pressure and through-thickness permeability. NPN surfaces come into contact with surrounding laminae and then capillary pressure is generated from the resin-air interface within the pores of the NPN. As these surfaces come into contact, entrapped gases can migrate throughout the NPN as a function of the NPN's permeability. Secondary characteristics— thickness, compressibility, and conformability— and their importance in NPN integration were discussed.

Microstructural characterization of Nanoporous Networks

The capillary pressure and permeability of the various NPNs, along with other nanoporous materials, were characterized via capillary flow porometry (CFP). Using CFP, mean flow pore (MFP) pore sizes range from $\sim$ 20 nm to $\sim$ 2 μm in this work, MFP capillary pressures range from 0.025 MPa (0.25 bar) to $\sim$ 1.3 MPa (13 bar), and through-thickness permeabilities range from $\sim 1*10^{-5}$ μm^2 to $\sim 2*10^{-2}$ μm^2 for NPNs are observed. The thickness of NPNs were measured using microcomputed tomography (μCT) or scanning electron microscopy (SEM).

Development of Preliminary Ashby Guidelines

Ashby Plots were established to display the properties of capillary pressure and permeability for the measured materials. Through these plots, the range of different materials, especially PI aerogel films, are demonstrated. Two main material categories are established with the use of these plots: (1) high capillary pressure and low permeability and (2) low capillary pressure and high permeability.

Design of 2D and 3D In Situ Experiments for NPN Application Understanding

A 2D in situ experiment was designed to monitor the resin flow front through an NPN-integrated laminate. From this experiment, the compressibility of a SCD PI aerogel was demonstrated as a function of temperature. A SCD PI aerogel of 151 μm thickness was reduced to 30 % of its original size with no applied vacuum. A 3D in situ experiment was also conceived to investigate the void evolution of IM7/8552 CFRP woven laminates during the first 45 minutes of their cure cycle. Using aerospace-grade woven IM7/8552 pre-impregnated fibers (prepreg), void growth and creation was exhibited after the application of temperature, regardless of NPN use. Heat treating the laminae, in a process termed desolventing, reduced the residual solvent left in the prepreg. Void expansion and growth was terminated after an added desolventing step and included into the IM7/8552 woven laminate manufacturing process.

Process Modification of VBO-Manufacturing to Produce Low-Void Content Laminates via Desolventing

Discovered via the multi-step 3D in situ experiment, void growth and expansion occurred significantly throughout woven CFRP laminates after subjecting the layered architecture to elevated temperatures. To mitigate this effect from the residual solvent leftover from the prepreg manufacturer process, laminae were subjected to heat treatment and vacuum before completing the laminate layup. By using a vacuum oven and exposing the laminae to an

environment of $\sim$ 10 millibar and 60 °C for 60 minutes, the growth of intralaminar voids during the cure cycle is prevented, leading to low void content VBO-manufactured IM7/8552 woven laminates.

Demonstration of Successful NPN-Integration with CFRP Laminates to Create Low-Void Content Layered Architectures

Through the use of desolventing at $\sim$ 10 millibar and 60 °C for 60 minutes, along with NPN-integration techniques of manual rolling, low-void content IM7/8552 woven laminates were able to be VBO-manufactured via oven-curing. For square panels with side lengths of 25.4 mm (1 inch), all tested NPNs, SCD PI aerogel, AD PI aerogel, and polymer NPN, produced specimens with 0.2 vol% voids or less. For square panels with side lengths of 76.2 mm (3 inch) or 152.4 mm (6 inch), only AD PI aerogel was able to produce specimens with 0.2 vol% voids or less. At the 152.4 mm (6 inch) scale, the void vol% of the woven laminate with AD PI aerogel NPN was measured at 0.11 vol%, which is almost one order of magnitude lower than the aerospace industry standard.

7.2 Recommendations for Future Work

Within this section, recommendations for future work will be suggested to further the development of this VBO-manufacturing technique. Long-term, future goals include large-scale industrial integration of these NPNs for a variety of composite systems.

Expansion to Other Relevant Composite Systems

To demonstrate the versatility of NPN usage within FRP laminates, other autoclave formulated and aerospace-grade FRP prepreg should be tested with the selection of NPNs provided in this thesis. This can include low-viscosity prepreg systems or GFRP woven autoclave prepreg. By expanding the catalog of composite systems investigated, a better

understanding of NPN characteristics can be achieved to aid in the NPN selection process.

Mechanical Performance Evaluation

While 152.4 mm (6 inch) square panels were manufactured with a low void content of 0.11 vol%, the mechanical performance of this laminate needs to be investigated in comparison to baseline autoclave manufactured IM7/8552 woven laminates. Short beam shear testing can be completed to investigate the interlaminar shear strength, while flexural beam testing can be performed to explore in-plane mechanical properties. Differential scanning calorimetry should be completed to analyze the degree of cure between the two sets of manufactured laminates: (1) VBO-manufactured and NPN-enabled and (2) autoclave-manufactured baseline (no NPN) laminates.

Manufacture Sample with OoO Techniques to Further Increase Energy Savings and Remove Part Geometrical Constraints

To quantify the energy used to VBO-manufacture these NPN-enabled laminates, out-of-oven (OoO) heaters can be employed. Maximum manufacturer recommended cure cycle (MRCC) heating ramp rates can be utilized using carbon nanotube (CNT) resistive heaters. This energy measurement could be compared to autoclave and oven energy requirements to highlight the advantages of these coupled manufacturing techniques.

Adapt Current Experiments for SCRT to Validate Current Flow Front Model and Observe Void Evolution Throughout Entire MRCCs

While the designed in situ μCT experiments provided insights into NPN-enabled laminate performance, more comprehensive information could be collected through the use of synchrontron radiation computed tomography (SRCT). For the 2D flow front monitoring in situ experiment, sub-second projections could be captured at improved resolutions, allowing real-time collection of the resin flow front through a NPN. For the 3D void evolution in situ

experiment, using SCRT would enable visualization of the laminate throughout the entire MRCC versus the previous 45 minutes. Multiple composite systems or NPNs could easily be tested through alterations of the laminate lay up.

Quantify the Secondary Characteristics of NPNs

While the thickness was measured using μCT, conformability and compressibility should also be quantified to add another measured characteristic to classify the NPN. By measuring the properties of these secondary characteristics, a range of values for conformability and compressibility could be used to better understand the function of NPNs at the lamina-NPN interface and help update current NPN models.

References

[1]R. R. Nagavally, "Composite materials-history, types, fabrication techniques, advantages, and applications", in 29th IRF International Conference (2016).

[2]A. Kelly, "Composite materials after seventy years", Journal of Materials Science **41**, 905–912 (2006).

[3]S. Hegde, B. Satish Shenoy, and K. Chethan, "Review on carbon fiber reinforced polymer (CFRP) and their mechanical performance", Materials Today: Proceedings **19**, 658–662 (2019).

[4]D. R. Tenney, J. G. Davis Jr, R. B. Pipes, and N. Johnston, "Nasa composite materials development: lessons learned and future challenges", in NATO RTO AVT-164 Workshop on Support of Composite Systems, LF99-9370 (2009).

[5]*Carbon Fiber Study*, Technical Memorandum NASA-TM-79449 (National Aeronuatics and Space Administration, Jan. 1977).

[6]F. Campbell, *Structural Composite Materials* (ASM International, Nov. 2010).

[7]C. González, J. J. Vilatela, J. M. Molina-Aldareguía, C. S. Lopes, and J. LLorca, "Structural composites for multifunctional applications: Current challenges and future trends", Progress in Materials Science **89**, 194–251 (2017).

[8]M. Altin Karataş and H. Gökkaya, "A review on machinability of carbon fiber reinforced polymer (CFRP) and glass fiber reinforced polymer (GFRP) composite materials", Defence Technology, Composite Materials in Defence Technology **14**, 318–326 (2018).

[9]H. Zheng, W. Zhang, B. Li, J. Zhu, C. Wang, G. Song, G. Wu, X. Yang, Y. Huang, and L. Ma, "Recent advances of interphases in carbon fiber-reinforced polymer composites: A review", Composites Part B: Engineering **233**, 109639 (2022).

[10]D. Chung, "Carbon Fiber Composites", in (Butterworth-Heinemann, 1994), pp. 85–123.

[11]M. F. Ashby, *Materials selection in mechanical design*, 2. ed., reprinted (Elsevier Butterworth-Heinemann, Amsterdam, 2004).

[12]A. Quilter, "Composites in aerospace applications", IHS White Paper **444**, 264 (2001).

[13]S. Kesarwani et al., "Polymer composites in aviation sector", International Journal of Engineering Research and Technology (IJERT) **6** (2017).

[14]M. Norkhairunnisa, T. Chai Hua, S. Sapuan, and R. Ilyas, "Evolution of aerospace composite materials", in *Advanced composites in aerospace engineering applications* (Springer, 2022), pp. 367–385.

[15]Firefly Aerospace, *Alpha Launch Vehicle*, https://fireflyspace.com/alpha/ (visited on 06/28/2024).

[16]B. L. Wardle, J. H. Koo, G. M. Odegard, and G. D. Seidel, "Advanced Nanoengineered Materials", in *Aerospace Materials and Applications* (2017), pp. 275–304.

[17]L. Gorbatikh, B. L. Wardle, and S. V. Lomov, "Hierarchical lightweight composite materials for structural applications", MRS Bulletin **41**, 672–677 (2016).

[18]L. Nele, A. Caggiano, and R. Teti, "Autoclave Cycle Optimization for High Performance Composite Parts Manufacturing", Procedia CIRP, Factories of the Future in the digital environment - Proceedings of the 49th CIRP Conference on Manufacturing Systems **57**, 241–246 (2016).

[19]S. Y. Park, C. H. Choi, W. J. Choi, and S. S. Hwang, "A Comparison of the Properties of Carbon Fiber Epoxy Composites Produced by Non-autoclave with Vacuum Bag Only Prepreg and Autoclave Process", Applied Composite Materials **26**, 187–204 (2019).

[20]Y. S. Song, J. R. Youn, and T. G. Gutowski, "Life cycle energy analysis of fiber-reinforced composites", Composites Part A: Applied Science and Manufacturing, Special Issue: 15th French National Conference on Composites - JNC15 **40**, 1257–1265 (2009).

[21]T. Centea, L. K. Grunenfelder, and S. R. Nutt, "A review of out-of-autoclave prepregs – Material properties, process phenomena, and manufacturing considerations", Composites Part A: Applied Science and Manufacturing **70**, 132–154 (2015).

[22]J. Lee, X. Ni, F. Daso, X. Xiao, D. King, J. S. Gómez, T. B. Varela, S. S. Kessler, and B. L. Wardle, "Advanced carbon fiber composite out-of-autoclave laminate manufacture via nanostructured out-of-oven conductive curing", Composites Science and Technology, Carbon nanotube composites for structural applications **166**, 150–159 (2018).

[23]J. Lee, I. Y. Stein, E. F. Antunes, S. S. Kessler, and B. L. Wardle, "Out-of-oven curing of polymeric composites via resistive microheaters comprised of aligned carbon nanotube networks", in Twentieth International Committee on Composite Materials (ICCM20) (2015).

[24]X. Li, F. Daso, J. Lee, J. Spangler, J.-P. Canart, M. Kinsella, and B. L. Wardle, "Consolidation of aerospace-grade high-temperature thermoplastic carbon fiber composites via nano-engineered electrothermal heating", Composites Part B: Engineering **262**, 110814 (2023).

[25]J. Lee, S. S. Kessler, and B. L. Wardle, "Void-free layered polymeric architectures via capillary-action of nanoporous films", Advanced Materials Interfaces **7**, 1901427 (2020).

[26]A. N. Webb, J. Dai, K. Asamoah-Addo, J. Griffin, S. A. S. III, and B. L. Wardle, "Fundamental Study of Nanoporous Network (NPN) Characteristics Enabling Out of Autoclave Manufacturing of Aerospace-Grade Composite Laminates", in Twenty-third International Conference On Composite Materials (ICCM23) (2023).

[27]J. Dai, A. Webb, J. Lee, K. Asamoah-Addo, J. Griffin, S. Steiner, and B. L. Wardle, "Investigation of Void Removal Behavior during Nanoporous Network Enabled Out of

Autoclave Manufacturing of Void-free Aerospace-grade Carbon Fiber Reinforced Plastic Composites", in AIAA SCITECH 2024 Forum (2024), p. 1219.

[28]C. X. Li, T. J. Hank, E. Kalfon-Cohen, C. Furtado, J. Lee, S. Cassady, J. Tucker, S. S. Kessler, and B. L. Wardle, "Manufacturing Autoclave-Grade Thermoset Carbon Fiber-Reinforced Polymer Aerospace Composites without an Autoclave Using Nanoporous Materials", ACS Applied Materials & Interfaces **16**, Publisher: American Chemical Society, 25280–25293 (2024).

[29]T. J. Hank, J. Lee, S. Cassady, S. Kessler, S. Steiner, and B. L. Wardle, "Void-Free Vacuum-Bag-Only Composite Manufacturing with Autoclave-Grade Prepreg Using Capillary Effects of Polymer Electrospun Nanofibers and Aerogel Nanoporous Networks", in AIAA SCITECH 2022 Forum (2022), p. 1094.

[30]S. Serrano, "Nanomaterial-Enabled Out-of-Autoclave and Out-of-Oven Manufacturing of Fiber Reinforced Polymer Composites", Master's thesis (Massachusetts Institute of Technology, Sept. 2023).

[31]D. K. Rajak, D. D. Pagar, P. L. Menezes, and E. Linul, "Fiber-Reinforced Polymer Composites: Manufacturing, Properties, and Applications", Polymers **11**, 1667 (2019).

[32]J. D. Buckley and D. D. Edie, *Carbon-Carbon Materials and Composites* (William Andrew, Dec. 1993), pp. 78–79.

[33]L. Mohammed, M. N. Ansari, G. Pua, M. Jawaid, and M. S. Islam, "A Review on Natural Fiber Reinforced Polymer Composite and Its Applications", International Journal of Polymer Science **2015**, 243947 (2015).

[34]Y.-W. Lim, J. Jin, and B.-S. Bae, "Optically Transparent Multiscale Composite Films for Flexible and Wearable Electronics", Advanced Materials **32**, 1907143 (2020).

[35]S. Prashanth, K. Subbaya, K. Nithin, and S. Sachhidananda, "Fiber Reinforced Composites - A Review", Journal of Material Science & Engineering **6**, 2–6 (2017).

[36]S. Arbab and J. D. Menczel, "18 - Thermal analysis of acrylic and carbon fibers", in *Thermal Analysis of Textiles and Fibers*, edited by M. Jaffe and J. D. Menczel, The Textile Institute Book Series (Woodhead Publishing, Jan. 2020), pp. 297–323.

[37]S.-J. Park, *Carbon fibers*, Vol. 210 (Springer, 2015).

[38]V. M. Drakonakis, J. C. Seferis, and C. C. Doumanidis, "Curing Pressure Influence of Out-of-Autoclave Processing on Structural Composites for Commercial Aviation", Advances in Materials Science and Engineering **2013**, 356824 (2013).

[39]B. S. Hayes, J. C. Seferis, and J. S. Chen, "Development and hot-melt impregnation of a model controlled flow prepreg system", Polymer Composites **17**, 730–742 (1996).

[40]Y. Golfman, *Hybrid Anisotropic Materials for Structural Aviation Parts* (CRC Press, Apr. 2016).

[41]J. C. Seferis, *Cryogenic Cycling Behavior of Polymeric Composite Materials:* tech. rep. (Defense Technical Information Center, Fort Belvoir, VA, Dec. 2002).

[42]C. Harris, Starnes, J. H, and M. Shuart, *An Assessment of the State-of-the-Art in the Design and Manufacturing of Large Composite Structures for Aerospace Vehicles*, Technical Memorandum NASA/TM-2001-210844 (NASA, Langley Research Center, Hampton VA, Apr. 2001).

[43]I. Fernández, F. Blas, and M. Frövel, "Autoclave forming of thermoplastic composite parts", Journal of Materials Processing Technology, Proceedings of the International Conference on the Advanced Materials Processing Technology, 2001. **143-144**, 266–269 (2003).

[44]M. Ramezankhani, B. Crawford, A. Narayan, H. Voggenreiter, R. Seethaler, and A. S. Milani, "Making costly manufacturing smart with transfer learning under limited data: A case study on composites autoclave processing", Journal of Manufacturing Systems **59**, 345–354 (2021).

[45]A. R. Upadhya, G. N. Dayananda, G. M. Kamalakannan, J. Ramaswamy Setty, and J. Christopher Daniel, "Autoclaves for Aerospace Applications: Issues and Challenges", International Journal of Aerospace Engineering **2011**, 985871 (2011).

[46]HexPly®, *HexPly® 8552 Epoxy matrix (180˚C/356˚F curing matrix) Product Data*, https://energy.ornl.gov/CFCrush/materials/uou/8552_eu.pdf (visited on 08/01/2024).

[47]P. K. Mallick, "6 - Thermoset–matrix composites for lightweight automotive structures", in *Materials, Design and Manufacturing for Lightweight Vehicles*, edited by P. K. Mallick, Woodhead Publishing Series in Composites Science and Engineering (Woodhead Publishing, Jan. 2010), pp. 208–231.

[48]O. A. Ekuase, N. Anjum, V. O. Eze, and O. I. Okoli, "A Review on the Out-of-Autoclave Process for Composite Manufacturing", Journal of Composites Science **6**, Number: 6 Publisher: Multidisciplinary Digital Publishing Institute, 172 (2022).

[49]Hoffman Construction Company, *Hoffman Construction — Boeing 777X Composite Wing Center (Building 40-58)*, https://www.hoffmancorp.com/project/777x-composite-wing-center-building-40-58/ (visited on 07/07/2024).

[50]Q. Wang, L. Wang, W. Zhu, Q. Xu, and Y. Ke, "Design optimization of molds for autoclave process of composite manufacturing", Journal of Reinforced Plastics and Composites **36**, 1564–1576 (2017).

[51]P. G. Ifju, B. C. Kilday, X. Niu, and S.-C. Liu, "A Novel Method to Measure Residual Stresses in Laminated Composites", Journal of Composite Materials **33**, 1511–1524 (1999).

[52]J. Dai, A. Webb, J. Lee, L. Randaccio, J. Griffin, S. A. Steiner III, and B. L. Wardle, "Out of Autoclave Manufacturing of Void-free Woven Aerospace-grade Carbon Fiber Reinforced Plastic Composite Laminates Using Capillary Effects of Aerogel Nanoporous Networks", in AIAA SCITECH 2023 Forum (2023), p. 0516.

[53]F. Y. C. Boey and S. W. Lye, "Void reduction in autoclave processing of thermoset composites: Part 1: High pressure effects on void reduction", Composites **23**, 261–265 (1992).

[54]T.-H. Hou, S. G. Miller, T. S. Williams, and J. K. Sutter, "Out-of-autoclave processing and properties of bismaleimide composites", Journal of Reinforced Plastics and Composites **33**, 137–149 (2014).

[55]P. Hubert, "9 - Autoclave and out-of-autoclave processing of prepregs", in *Design and Manufacture of Structural Composites*, edited by L. Harper and M. Clifford, Woodhead Publishing Series in Composites Science and Engineering (Woodhead Publishing, Jan. 2023), pp. 209–236.

[56]C. Soutis, "1 - Aerospace engineering requirements in building with composites", in *Polymer Composites in the Aerospace Industry (Second Edition)*, edited by P. Irving and C. Soutis, Woodhead Publishing Series in Composites Science and Engineering (Woodhead Publishing, Jan. 2020), pp. 3–22.

[57]S. Laurenzi, M. Marchetti, et al., "Advanced composite materials by resin transfer molding for aerospace applications", in *Composites and their properties* (InTech, 2012), pp. 197–226.

[58]M. K. Kang, W. I. Lee, and H. T. Hahn, "Formation of microvoids during resin-transfer molding process", Composites Science and Technology **60**, 2427–2434 (2000).

[59]V. R. Tamakuwala, "Manufacturing of fiber reinforced polymer by using VARTM process: a review", Materials Today: Proceedings **44**, 987–993 (2021).

[60]K. Hsiao and D. Heider, "10 - Vacuum assisted resin transfer molding (VARTM) in polymer matrix composites", in *Manufacturing Techniques for Polymer Matrix Composites (PMCs)*, edited by S. G. Advani and K.-T. Hsiao, Woodhead Publishing Series in Composites Science and Engineering (Woodhead Publishing, Jan. 2012), pp. 310–347.

[61]C. Garschke, C. Weimer, P. P. Parlevliet, and B. L. Fox, "Out-of-autoclave cure cycle study of a resin film infusion process using in situ process monitoring", Composites Part A: Applied Science and Manufacturing **43**, 935–944 (2012).

[62]A. P. Mouritz, "14 - Manufacturing of fibre–polymer composite materials", in *Introduction to Aerospace Materials*, edited by A. P. Mouritz (Woodhead Publishing, Jan. 2012), pp. 303–337.

[63]Y. Chen, J. Zhang, Z. Li, H. Zhang, J. Chen, W. Yang, T. Yu, W. Liu, and Y. Li, "Manufacturing Technology of Lightweight Fiber-Reinforced Composite Structures in Aerospace: Current Situation and toward Intellectualization", Aerospace **10**, 206 (2023).

[64]C. X. Li, C. Catalano, C. Furtado, E. Kalfon-Cohen, S. Cassady, J. Lee, S. Kessler, and B. L. Wardle, "Enhanced Manufacturing of Complex Shape Composites with Nano-Porous Networks", in AIAA SCITECH 2023 Forum (2023), p. 0199.

[65]J. Lee, I. Y. Stein, S. S. Kessler, and B. L. Wardle, "Aligned Carbon Nanotube Film Enables Thermally Induced State Transformations in Layered Polymeric Materials", ACS Applied Materials & Interfaces **7**, 8900–8905 (2015).

[66]R. Dawson, A. I. Cooper, and D. J. Adams, "Nanoporous organic polymer networks", Progress in Polymer Science, Topical Issue on Polymer Physics **37**, 530–563 (2012).

[67]B. Zdravkov, J. Čermák, M. Šefara, and J. Janků, "Pore classification in the characterization of porous materials: A perspective", Open Chemistry **5**, 385–395 (2007).

[68]S. P. Adiga, C. Jin, L. A. Curtiss, N. A. Monteiro-Riviere, and R. J. Narayan, "Nanoporous membranes for medical and biological applications", WIREs Nanomedicine and Nanobiotechnology **1**, 568–581 (2009).

[69]R. Ron, E. Haleva, and A. Salomon, "Nanoporous Metallic Networks: Fabrication, Optical Properties, and Applications", Advanced Materials **30**, 1706755 (2018).

[70]B. C. Tappan, S. A. Steiner III, and E. P. Luther, "Nanoporous Metal Foams", Angewandte Chemie International Edition **49**, 4544–4565 (2010).

[71]T. Juarez, J. Biener, J. Weissmüller, and A. M. Hodge, "Nanoporous Metals with Structural Hierarchy: A Review", Advanced Engineering Materials **19**, 1700389 (2017).

[72]G. Q. M. Lu and X. S. Zhao, *Nanoporous Materials: Science And Engineering* (World Scientific, Nov. 2004).

[73]M. T. Q. S. da Silva, M. do Rocio Cardoso, C. M. P. Veronese, and W. Mazer, "Tortuosity: A brief review", Materials Today: Proceedings, 3rd International Congress on Materials & Structural Stability **58**, 1344–1349 (2022).

[74]B. Ghanbarian, A. G. Hunt, R. P. Ewing, and M. Sahimi, "Tortuosity in Porous Media: A Critical Review", Soil Science Society of America Journal **77**, 1461–1477 (2013).

[75]R. Ouimet, J. Young, T. Schuler, G. Bender, G. Roberts, and K. Ayers, "Measurement of Resistance, Porosity, and Water Contact Angle of Porous Transport Layers for Low-Temperature Electrolysis Technologies", Frontiers in Energy Research **10**, 911077 (2022).

[76]D. Li, M. W. Frey, and Y. L. Joo, "Characterization of nanofibrous membranes with capillary flow porometry", Journal of Membrane Science **286**, 104–114 (2006).

[77]M. Halisch, E. Vogt, C. Müller, A. Cano-Odena, D. Pattyn, P. Hellebaut, and K. van der Kamp, "Capillary flow porometry-assessment of an alternative method for the determination of flow relevant parameters of porous rocks", in Proceedings of International Symposium of the Society of Core Analysts, Napa Valley, California, USA (2013), pp. 16–19.

[78]A. Paar, *Basics of capillary flow porometry | Anton Paar Wiki*, https://wiki.anton-paar.com/en/basics-of-capillary-flow-porometry/ (visited on 08/19/2024).

[79]A. Jena and K. Gupta, "Advances in Pore Structure Evaluation by Porometry", Chemical Engineering & Technology **33**, 1241–1250 (2010).

[80]K. Bromberger, J. Ghinaiya, T. Lickert, A. Fallisch, and T. Smolinka, "Hydraulic ex situ through-plane characterization of porous transport layers in PEM water electrolysis cells", International Journal of Hydrogen Energy **43**, 2556–2569 (2018).

[81]E. Maire, "X-Ray Tomography Applied to the Characterization of Highly Porous Materials", Annual Review of Materials Research **42**, 163–178 (2012).

[82]J. Kratz, P. Galvez-Hernandez, L. R. Pickard, J. Belnoue, and K. Potter, "Lab-based *in-situ* micro-CT observation of gaps in prepreg laminates during consolidation and cure", Composites Part A: Applied Science and Manufacturing **140**, 106180 (2021).

[83]S. C. Garcea, Y. Wang, and P. J. Withers, "X-ray computed tomography of polymer composites", Composites Science and Technology **156**, 305–319 (2018).

[84]R. Kopp, J. Joseph, and B. L. Wardle, "Automated Segmentation of In Situ X-ray Microtomography of Progressive Damage in Advanced Composites via Deep Learning", in AIAA Scitech 2021 Forum (2021), p. 2024.

[85]X. Ni, N. K. Fritz, and B. L. Wardle, "In Situ Testing Using Synchrotron Radiation Computed Tomography in Materials Research", MRS Advances **4**, 2831–2841 (2019).

[86]K. Naresh, K. A. Khan, R. Umer, and W. J. Cantwell, "The use of X-ray computed tomography for design and process modeling of aerospace composites: A review", Materials & Design **190**, 108553 (2020).

[87]P. J. Withers, C. Bouman, S. Carmignato, V. Cnudde, D. Grimaldi, C. K. Hagen, E. Maire, M. Manley, A. Du Plessis, and S. R. Stock, "X-Ray Computed Tomography", Nature Reviews Methods Primers **1**, 1–21 (2021).

[88]S. Stock, "X-ray microtomography of materials", International Materials Reviews **44**, 141–164 (1999).

[89]D. H. Bilderback, P. Elleaume, and E. Weckert, "Review of third and next generation synchrotron light sources", Journal of Physics B: Atomic, Molecular and Optical Physics **38**, S773 (2005).

[90]The European Synchrotron Radiation Facility, *How does a synchrotron work?*, https://www.esrf.fr/cms/live/live/en/sites/www/home/education/what-is-the-esrf/how-does-the-esrf-work.html (visited on 06/04/2024).

[91]T. J. Hank, J. Lee, S. Cassady, S. Kessler, S. Steiner, and B. L. Wardle, "Void-free Vacuum-bag-only Composite Manufacturing with Autoclave-grade Prepreg using Capillary Effects of Polymer Electrospun Nanofibers and Aerogel Nanoporous Networks", in AIAA SCITECH 2022 Forum (2022), p. 1094.

[92]T. J. Hank, "Capillary Effects of Nanoporous Networks on Aerospace Autoclave-grade Prepreg Composites Enabling Vacuum-bag-only Manufacturing", Master's thesis (Massachusetts Institute of Technology, June 2021).

[93]J. Lee, "Nanomaterial-enabled manufacturing for next-generation multifunctional advanced composite prepreg laminate architectures", PhD thesis (Massachusetts Institute of Technology, 2018).

[94]A. L. Kaiser, "Interfacial and physical confinement effects on the structure and properties of aligned carbon nanotube architectures", PhD thesis (Massachusetts Institute of Technology, 2021).

[95]B. L. Wardle, D. S. Saito, E. J. García, A. J. Hart, R. G. de Villoria, and E. A. Verploegen, "Fabrication and Characterization of Ultrahigh-Volume- Fraction Aligned Carbon Nanotube–Polymer Composites", Advanced Materials **20**, 2707–2714 (2008).

[96]A. L. Kaiser and B. L. Wardle, "Fabrication of hierarchical polymer nanocomposites with capillary-densified aligned carbon nanotube reinforcement", in Twenty-second International Conference On Composite Materials (ICCM22) (2019), pp. 396–407.

[97]J. Lee, I. Y. Stein, M. E. Devoe, D. J. Lewis, N. Lachman, S. S. Kessler, S. T. Buschhorn, and B. L. Wardle, "Impact of carbon nanotube length on electron transport in aligned carbon nanotube networks", Applied Physics Letters **106**, 053110 (2015).

[98]K. E. Parmenter and F. Milstein, "Mechanical properties of silica aerogels", Journal of Non-Crystalline Solids **223**, 179–189 (1998).

[99]A. Soleimani Dorcheh and M. H. Abbasi, "Silica aerogel; synthesis, properties and characterization", Journal of Materials Processing Technology **199**, 10–26 (2008).

[100]S. Ghaffari-Mosanenzadeh, O. Aghababaei Tafreshi, S. Karamikamkar, Z. Saadatnia, E. Rad, M. Meysami, and H. E. Naguib, "Recent advances in tailoring and improving the properties of polyimide aerogels and their application", Advances in Colloid and Interface Science **304**, 102646 (2022).

[101]H. Guo, M. A. B. Meador, L. McCorkle, D. J. Quade, J. Guo, B. Hamilton, M. Cakmak, and G. Sprowl, "Polyimide Aerogels Cross-Linked through Amine Functionalized Polyoligomeric Silsesquioxane", ACS Applied Materials & Interfaces **3**, 546–552 (2011).

[102]NanoLayr, *XantuLayr - NanoLayr*, (Mar. 2021) https://www.nanolayr.com/product/xantulayr/ (visited on 07/23/2024).

[103]Celgard, *Battery Separator Products & Literature | Celgard World Leader in Battery Separator Technology*, https://www.celgard.com/product-data (visited on 07/14/2024).

[104]Y. Subasi and B. Cicek, "Recent advances in hydrophilic modification of PVDF ultrafiltration membranes – a review: part I", Membrane Technology **2017**, 7–12 (2017).

[105]W. Lee and S.-J. Park, "Porous Anodic Aluminum Oxide: Anodization and Templated Synthesis of Functional Nanostructures", Chemical Reviews **114**, 7487–7556 (2014).

[106]A. Santos, T. Kumeria, and D. Losic, "Nanoporous anodic aluminum oxide for chemical sensing and biosensors", TrAC Trends in Analytical Chemistry **44**, 25–38 (2013).

[107]S. L. Agius, K. J. C. Magniez, and B. L. Fox, "Cure behaviour and void development within rapidly cured out-of-autoclave composites", Composites Part B: Engineering **47**, 230–237 (2013).

[108]C. Song and G. C. Rutledge, "Electrospun Liquid-Infused Membranes for Emulsified Oil/Water Separation", Langmuir **38**, 2301–2313 (2022).

[109]F. A. AlMarzooqi, M. R. Bilad, B. Mansoor, and H. A. Arafat, "A comparative study of image analysis and porometry techniques for characterization of porous membranes", Journal of Materials Science **51**, 2017–2032 (2016).

[110]K. J. Ahn, J. C. Seferis, and J. C. Berg, "Simultaneous measurements of permeability and capillary pressure of thermosetting matrices in woven fabric reinforcements", Polymer Composites **12**, 146–152 (1991).

[111]R. A. Greenkorn, "Steady flow through porous media", AIChE Journal **27**, 529–545 (1981).

[112]S. Hernández, F. Sket, J. M. Molina-Aldareguı´a, C. González, and J. LLorca, "Effect of curing cycle on void distribution and interlaminar shear strength in polymer-matrix composites", Composites Science and Technology **71**, 1331–1341 (2011).

[113]B. A. Morris, "8 - Barrier", in *The Science and Technology of Flexible Packaging*, edited by B. A. Morris, Plastics Design Library (William Andrew Publishing, Oxford, Jan. 2017), pp. 259–308.

[114]L. Skartsis, J. L. Kardos, and B. Khomami, "Resin flow through fiber beds during composite manufacturing processes. Part I: Review of newtonian flow through fiber beds", Polymer Engineering & Science **32**, 221–230 (1992).

[115]S. C. Amico and C. Lekakou, "Axial impregnation of a fiber bundle. Part 2: Theoretical analysis", Polymer Composites **23**, 264–273 (2002).

[116]R. Brault, A. Germaneau, J. C. Dupré, P. Doumalin, S. Mistou, and M. Fazzini, "In-situ Analysis of Laminated Composite Materials by X-ray Micro-Computed Tomography and Digital Volume Correlation", Experimental Mechanics **53**, 1143–1151 (2013).

[117]T. Centea and P. Hubert, "Measuring the impregnation of an out-of-autoclave prepreg by micro-CT", Composites Science and Technology **71**, 593–599 (2011).

[118]D. Van Ee and A. Poursartip, *HexPly 8552 MATERIAL PROPERTIES DATABASE for use with COMPRO CCA and Raven*, Nov. 2009.

[119]N. Zobeiry and C. Duffner, "Measuring the negative pressure during processing of advanced composites", Composite Structures **203**, 11–17 (2018).

[120]S. S. Rahatekar, K. K. K. Koziol, S. A. Butler, J. A. Elliott, M. S. P. Shaffer, M. R. Mackley, and A. H. Windle, "Optical microstructure and viscosity enhancement for an epoxy resin matrix containing multiwall carbon nanotubes", Journal of Rheology **50**, 599–610 (2006).

[121]HEXCEL, *HexPly® 8552 mid-toughened, high strength, damage-resistant, structural epoxy matrix Product Data*, https://www.hexcel.com/user_area/content_media/raw/HexPly_8552_us_DataSheet.pdf (visited on 08/01/2024).

[122]H. Villarraga-Gómez and S. T. Smith, "Effect of the number of projections on dimensional measurements with X-ray computed tomography", Precision Engineering **66**, 445–456 (2020).